ABSTRACT

LE, QUANG VAN. Relationship between Microstructure and Mechanical Properties in $Bi_2Sr_2CaCu_2O_x$ Round Wires Using Peridynamic Simulation. (Under the direction of Justin Schwartz).

$Bi_2Sr_2CaCu_2O_x$ (Bi2212) superconducting round wires are a well-known high temperature superconductor due to their isotropic properties, high fill factor, and ease of winding. There have been extensive experiments to improve the wires' performance, yet there is little understanding of how the internal microstructure of the wires influences the mechanical behavior. This is due to the multiple phases and their complex arrangements inside the wires, making it challenging for traditional approaches to investigate and simulate the wires' behavior. The peridynamic theory, using non-local interactions and integral constitutive equations, can provide a solution to these challenges from the Bi2212 wires microstructure. To reduce computation cost, in this study the peridynamic formulas are developed for 2D simulations. Dynamic relaxation and energy minimization methods to find the steady-state solution are used and compared. The model shows m-convergence and δ-convergence behaviors when m increases and δ decreases. Model verification shows close quantitative matching to finite element analysis results. The 2D peridynamic model is then used to simulate mechanical behavior of Bi2212 wires. Various types of natural and artificial defects are simulated and compared quantitatively. Both defect geometry and physical characteristics are investigated to study their influence on the stress concentration in the material. The results show significant stress concentration around defects and protruding growths of the Bi2212 phase.

Relationship between Microstructure and Mechanical Properties in $Bi_2Sr_2CaCu_2O_x$ Round Wires Using Peridynamic Simulation

by
Quang Van Le

A dissertation submitted to the Graduate Faculty of the
North Carolina State University
in partial fulfillment of the
requirements for the degree of
Doctor of Philosophy

Materials Science & Engineering

Raleigh, North Carolina

2014

APPROVED BY:

Justin Schwarz Committee Chair	Douglas Irving
Mohammed Zikry	Ronald Scattergood

ProQuest LLC.
789 East Eisenhower Parkway
P.O. Box 1346
Ann Arbor, MI 48106 - 1346

BIOGRAPHY

Quang Le is drawn to science because to him, it is just another way of saying “magic”. Quang received his M.S. from Florida State University in 2009 and is currently a Ph.D. student at North Carolina State University. He is experienced in both experimental and theoretical studies of electro-mechanical properties. He is set to graduate in 2014 and hopes to continue conducting research after graduation.

When not involved with school and research, Quang plays tennis and ballroom dances. He loves the outdoors and nature, especially aquatic life. He says he could stay in an aquarium all day, and his ideas have been inspired by nature from time to time.

ACKNOWLEDGEMENTS

I would like to express my gratitude to these persons for all their helps. Without them, I would not be able to be where I am today

- My advisor Justin Schwartz for his support and guidance throughout my long study.
- Former mentor Abdallah Mbaruku for his teaching and helping on my very first steps of being a graduate student.
- Ronald Scattergood, Douglas Irving, and Mohammed Zikry for serving on my committee.
- Wan Kan Chan for helpful discussions and guidance.
- My colleagues for collaboration and being great friends.
- And last but not least, my family for their eternal support and encouragement.

TABLE OF CONTENTS

LIST OF FIGURES vi

1. INTRODUCTION 1

   1.1. Superconductors 1

   1.2. High Temperature Superconductors 2

   1.3. Bi2212 Round Wires 4

   1.4. Peridynamic Theory 22

      1.4.1. Peridynamics as a Non-local Theory 22

      1.4.2. Relations between Classical Mechanics and Peridynamics 35

      1.4.3. Peridynamic Applications 40

2. 2D STATE BASED PERIDYNAMICS 50

   2.1. Introduction 50

   2.2. Peridynamic Model for 2D Plane Stress 51

   2.3. Peridynamic Model for 2D Plane Strain 57

   2.4. Simulation Approach 59

      2.4.1. Finding the Peridynamic Steady-State Solution 59

      2.4.2. Modifying the Node Interaction Volume 64

   2.5. Verification with FEM Analysis 65

      2.5.1. Convergence to Continuum Peridynamics 67

      2.5.2. Convergence to Classical Mechanics 70

   2.6. Peridynamics Stress at the Sharp Corners 74

3. Bi2212 STUDY RESULTS 78

3.1. Scanning Electron Microscopy Image Analysis 78
3.2. Peridynamics System Construction 81
3.3. Peridynamic Simulation Method 85
3.4. Simulation Results 86
  3.4.1. Samples with no defect 87
  3.4.2. Samples with a single natural defect from a SEM image 91
  3.4.3. Samples with a multiple natural defects from a SEM image 93
  3.4.4. Samples with rectangle artificial defects of different vertical lengths 95
  3.4.5. Samples with rectangle artificial defects of different horizontal widths 99
  3.4.6. Samples with 45 degree slanted artificial defects of different widths 102
  3.4.7. Samples with circular defects of different diameters 105
  3.4.8. Samples with artificial rectangle voids inside a Bi2212 filament 109
  3.4.9. Sample with artificial voids around a Bi2212 filament 111
  3.4.10. Simulation of stress concentration due to thermal cooling 112
4. CONCLUSION AND SUGGESTED FUTURE WORK 115
REFERENCES 120

LIST OF FIGURES

Figure 1.1. Superconductivity surface: superconductivity exists only when temperature, magnetic field, and current density all smaller than critical values. 2

Figure 1.2. Engineering critical current density versus magnetic field for low temperature superconductor wires, high temperature superconductor wires and tapes and MgB2 wires [1]. 4

Figure 1.3. Reliability vs. critical current in Bi2212 round wires [2]. 5

Figure 1.4. Cross-sectional scanning electron microscopy images of Bi2112 round wires: (a) Before heat treatment, and (b) After heat treatment. 7

Figure 1.5. Temperature–time schematics (not to scale) of the heat treatment profiles for (a) partial-melt processing, (b) split-melt processing, and (c) saw-tooth processing [3] 8

Figure 1.6. (a) Tomographic image of a heat treated wire, dark gray areas are bubbles. (b) Scanning electron microscopy image of a cut-out Bi2212 filament, showing the hollow core inside it [5]. 10

Figure 1.7. Cross-sectional SEM images of (a) filament with significant amount of Bi22012 phase and (b) filament consisting mostly Bi2212 phase [3]. 12

Figure 1.8. (a) Original cross-sectional SEM image analysis of Bi2212 wire showing intergrowths between the filaments. (b) Image analysis: bridges with different widths are marked with different colors from red to blue. 13

Figure 1.9. (a) Relationship between split temperature and bridge size and bridge area percentage. (b) Relationship between return temperature and bridge size and bridge area percentage [4]. 14

Figure 1.10. Relationship between 4.2 K, self-field Je, bridge size and bridge area percentage (of the non-Ag area) with bridges size, (a) 0–1 μm; (b) 1–2 μm; (c) 2–3 μm and (d) 3–4 μm [4]. 15

Figure 1.11. Dependence of critical current on compressive and tensile strains in Bi2212 in modified descriptive strain model [10]. 17

Figure 1.12. Original and simulated microstructures using fractal analysis [15]. 21

Figure 1.13. Steady-state von-Mises stress distribution with fixed load of 60 N/m to simulated microstructure [15]. 22

Figure 1.14. Interaction forces between 2 points in an ordinary peridynamic system. 24

Figure 1.15. Undeformed and deformed peridynamic bonds. 26

Figure 1.16. Dependence of different influence functions on bond vector. 28

Figure 1.17. Crack propagation speed with three different horizon sizes [38]. 33

Figure 1.18. Dispersion relations for various values of p. (a) with influence function in equation (1.18). (b) with influence function in equation (1.19) [23]. 34

Figure 1.19. Impact of a hard sphere on a disc of brittle material at $5\text{x}10^{-5}$s after impact. (a) p = 0. (b) p = 5. (c) p = 10 [23]. 35

Figure 1.20. Force acting on a surface in classical mechanics. 36

Figure 1.21. Interpretation of the force flux at x across a plane with unit normal n [41]. 39

Figure 1.22. Damaged maps for tests of crack path instability and branching, with sudden loads on top and bottom. (a) 12 MPa load, t = 46 μs. (b) 27 MPa load, t = 38 μs [42]. 41

Figure 1.23. Experimental results of cracking from sharp and blunt pre-notches [42, 45]. ... 41

Figure 1.24. (a) Crack growth in a glass plate under thermal cooling. (b) Peridynamic simulation result when ΔT = 2500 K [46]. 42

Figure 1.25. Peridynamic application in fracture of membrane (a); and a fiber network in initial and deformed configuration (b) [48]. 44

Figure 1.26. (a) Peridynamic discretization scheme of matrix and fibers in a laminate composite. (b) Local damage at interface between two lamina [28]. 45

Figure 1.27. Schematic for coupling of finite element method and peridynamics [29]. 48

Figure 2.1. Viscous interaction forces between two peridynamic nodes. 60

Figure 2.2. von Mises stress vs. simulation step in a system of 33144 nodes with (a) dynamic relaxation and (b) energy minimization. 63

Figure 2.3. (a) Two-dimensional diagram showing discrete nodes with boundaries (dotted lines), node 2 has about half of its volume inside the horizon region of node 1. (b) Volume fraction as a function of distance. 65

Figure 2.4. Rectangular plate with a hole in the middle. The left side is fixed and a tensile load is applied to the right. 66

Figure 2.5. Distribution along the horizontal line with different m values and a fixed δ. (a) Displacement vs. position (b) von Mises stress vs. position. 68

Figure 2.6. Distribution along the vertical line with different m values and a fixed δ. (a) Displacement vs. position. (b) von Mises stress vs. position. 69

Figure 2.7. Distribution along the horizontal line with different horizon sizes and a fixed m. (a) Displacement vs. position. (b) von Mises stress vs. position. 72

Figure 2.8. Distribution along the vertical line with different horizon sizes and a fixed m. (a) Displacement vs. position. (b) von Mises stress vs. position.. 72

Figure 2.9. von Mises stress distribution of (a) finite element simulation and (b) peridynamics simulation. Colors denote stress levels. Displacements are magnified 15,000 times in both cases. 73

Figure 2.10. Rectangular plate with a square hole in the middle. The left side is fixed and a tensile load is applied to the right. 75

Figure 2.11. Tensile test with different values of horizon size δ. (a) δ = 5 mm. (b) δ = 4 mm. (c) δ = 3 mm. (d) δ = 2mm... 76

Figure 2.12. Dependence of von Mises stress at the sharp corner on horizon size. 77

Figure 3.1. (a) Longitudinal SEM image of a Bi2212 filament. (b) Longitudinal SEM image of multiple Bi2212 filaments. (c) Processed microstructure from (a). (d) Processed microstructure from (b)... 79

Figure 3.2. Different defect shapes studied. (a) Single real defect. (b) Multiple real defects. (c) Artificial rectangle defect. (d) Artificial 45 degree slanted defect. (e) Artificial circular defect. (f) Artificial irregular defect... 80

Figure 3.3. (a) Discretization scheme from SEM image to peridynamic system. (b) Additional peridynamic nodes are added at the free boundary... 82

Figure 3.4. Effects of discretization grid size on phase boundary. (a) When grid size is equal to pixel size. (b) When grid size is half of pixel size.. 84

Figure 3.5. von Mises stress distribution in single-filament sample (a) 2D representation of the stress. (b) 3D representation of the stress, showing the concentrations at the phase boundary. 89

Figure 3.6. von Mises stress distribution in a cross-sectional microstructure with multiple filaments. (a) Longitudinal image. (b) Cross-sectional image. 91

Figure 3.7. von Mises stress distribution in the multiple-filament SEM image. (a) When there is a single void defect. (b) When the defect is a soft phase. (c) When the defect is a hard phase. 93

Figure 3.8. von Mises stress distribution. (a) When there are multiple void defects. (b) When there are multiple soft phase defects. (c) When there are multiple hard phase defects. 95

Figure 3.9. von Mises stress distribution when there is a rectangle defect. (a) When defect is a void. (b) When defect is a soft phase. (c) When defect is a hard phase. 98

Figure 3.10. Dependence of maximum von Mises stress on rectangle defect's vertical length. (a) When defect is a void. (b) When defect is a soft phase. (c) When defect is a hard phase. 99

Figure 3.11. von Mises stress distribution when there is a vertical defect cutting through the whole filament. (a) When defect is a void. (b) When defect is a soft phase. (c) When defect is a hard phase. 101

Figure 3.12. Dependence of maximum von Mises stress on vertical defect's horizontal width. (a) When defect is a void. (b) When defect is a soft phase. (c) When defect is a hard phase. 102

Figure 3.13. von Mises stress distribution when there is a 45 degree defect crossing the whole filament. (a) When defect is a void. (b) When defect is a soft phase. (c) When defect is a hard phase. 104

Figure 3.14. Dependence of maximum von Mises stress on 45 degree defect's width. (a) When defect is a void. (b) When defect is a soft phase. (c) When defect is a hard phase.... 105

Figure 3.15. von Mises stress distribution when there is a round defect. (a) When defect is a void. (b) When defect is a soft phase. (c) When defect is a hard phase. 108

Figure 3.16. Dependence of maximum von Mises stress on round defect's diameter. (a) When defect is a void. (b) When defect is a soft phase. (c) When defect is a hard phase.... 109

Figure 3.17. von Mises stress distribution when there is a rectangle void. (a) When defect's h:w aspect ratio is 4. (b) When the ratio is 1. (c) When the ratio is 0.25........ 111

Figure 3.18. von Mises stress distribution when a fraction of a Bi2212 is detached from the silver matrix. 112

Figure 3.19. Stress distribution when temperature change is -300 K. (a) Pressure. (b) von Mises stress. 114

Figure 4.1. (a) A crude, uniform mesh. (b) A mesh that roughly follows the image's interface and smoothens out the pixel artifacts [61]. 118

1. INTRODUCTION

1.1. Superconductors

Superconductors are materials that can carry an electrical current without generating heat. This is a desired property for applications where reducing energy waste or high current density is critical; since a resistive conductor with a high current will generate much heat and may damage the system. Superconductors show promises in applications using high field magnets such as maglev trains, magnetic resonance imaging, nuclear magnetic resonance, or in power transfer and storage applications. Other applications include digital circuits and sensitive magnetic sensors.

Superconductivity was first discovered by Heike Kamerlingh Onnes in 1911 in some pure metals such as mercury, tin, and lead. These metals have very low critical temperature above which superconductivity disappears: mercury at 4.2K, tin at 3.7K and lead at 7.2K. Other than temperature, superconductivity will also disappear if applied magnetic field is higher than a critical value. Also, below critical temperature and critical magnetic field, there is a maximum limit of electric current density a superconductor can carry, which is called critical current density. As Figure 1.1 shows, this critical current density decreases with increase of either temperature or magnetic field. Another feature of these superconductors is when they are in superconducting state, all outside magnetic field is expelled from the material. This effect is called Meissner effect and should not be confused with the Faraday shield effect of perfect conductors.

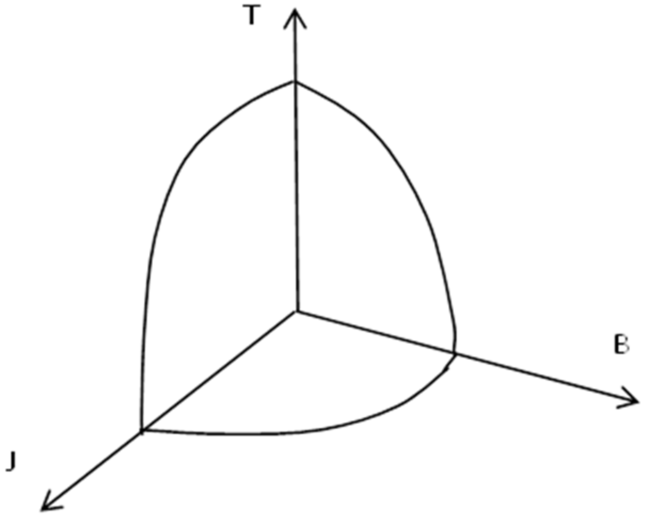

Figure 1.1. Superconductivity surface: superconductivity exists only when temperature, magnetic field, and current density all smaller than critical values.

After the discovery in mercury, tin, and lead, superconductivity was discovered in most other elements as well. Most pure elements (except vanadium, technetium and niobium) have type 1 superconductivity, in these superconductors the Meissner effect is an all or nothing phenomenon. If the magnetic field is less than critical value, no magnetic flux penetrates the material. But if the magnetic field is higher than that critical value, superconductivity is lost totally and the magnetic field penetrates the material completely.

1.2. High Temperature Superconductors

In 1930, another type of superconductivity was discovered by DeHaas and Voogd in PbBi alloy. Unlike type 1 superconductor, in PbBi there are two critical magnetic fields H_{c1} and H_{c2}. Below the magnetic field H_{c1}, all magnetic field is totally expelled from the conductor, similar to type 1 superconductors. But when magnetic field is increasing from H_{c1} to H_{c2}, the magnetic field does not penetrate the whole material immediately. It instead penetrates the material in quantized fluxes called vortices. These vortices comprise some but not all of the conductor's volume, thus superconductivity still remains. The superconductivity is only lost when magnetic field reaches the value H_{c2}. This behavior is called type 2 superconductivity. Most of type 2 superconductors that have been found are metallic compounds and alloys.

High temperature superconductors have advantages of lower cooling cost and higher critical current density. Among them, Bi2212 and YBCO are 2 most well-known high temperature superconductors. Figure 1.2 shows Bi2212 and YBCO have significantly higher critical current densities than others at high magnetic field. YBCO material has higher critical current density but it requires to be biaxially textured to be able to conduct the current. Consequently, YBCO must be made in tape form, while Bi2212 can be made in wire form which has higher fill factor than YBCO. In fact, Bi2212 is currently the only superconducting material that can be made in wires. A high fill factor is essential in applications that require high effective critical current density such as high field magnets.

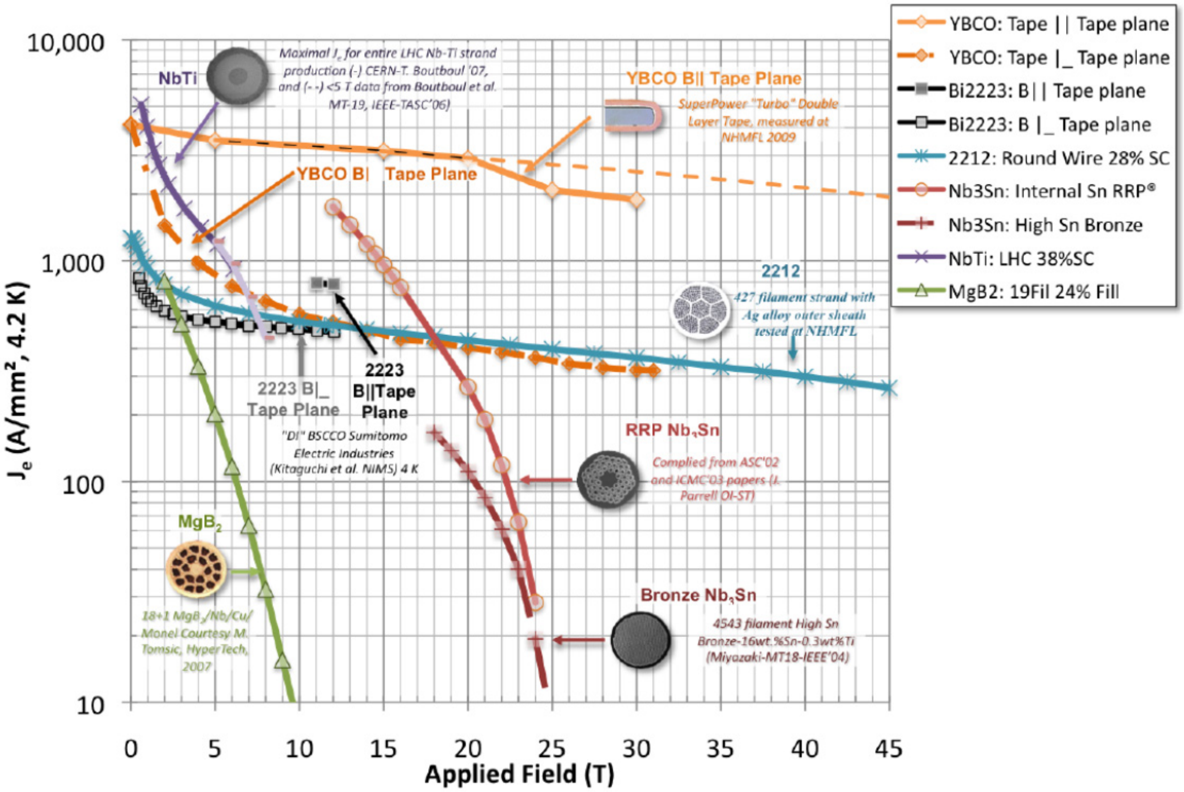

Figure 1.2. Engineering critical current density versus magnetic field for low temperature superconductor wires, high temperature superconductor wires and tapes and MgB2 wires [1].

1.3. Bi2212 Round Wires

As mentioned previously, the Bi2212 superconductor is a promising material due to high critical current density and the ability to conduct current when made in wire form. However, the superconductor is brittle and has to be reinforced with silver and silver magnesium. The conductor's performance is sensitive to the heat treatment parameters, and there is a wide variation of the outcome. Figure 1.3 shows the statistical analysis of the Bi2212 round wire conductor reliability as a function of critical current. The statistical approach is needed is because even individual samples of the same heat treatment batch, under the same mechanical loading condition, usually have different critical currents. On Figure 1.3 the reliability at a certain value of I_c on the graph is the probability a sample will have the current of at least that I_c value or higher. By definition, this probability is equal to 1 at zero critical current because every sample has a critical current of at least zero.

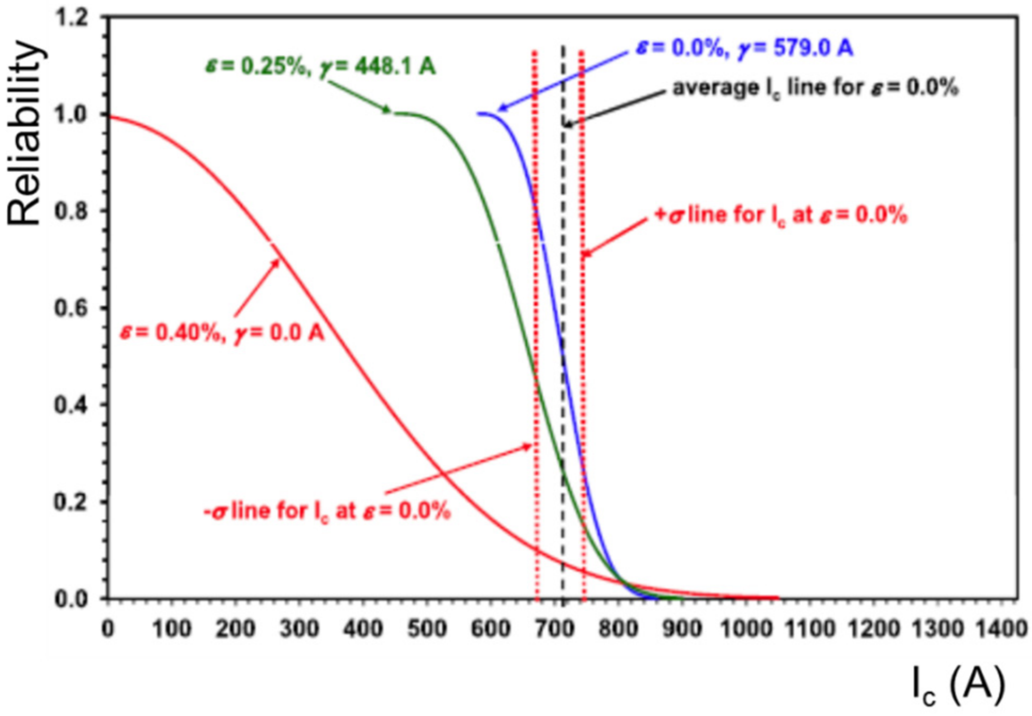

Figure 1.3. Reliability vs. critical current in Bi2212 round wires [2].

The reliability does not necessarily decrease immediately as I_c increases, in fact for samples under no mechanical loading (strain equal to zero), reliability stay constantly equal to one until I_c reaches the critical value $\gamma = 579A$. This means at no load condition, it is certain that every sample has critical current of at least 579A or higher. Value of γ however decreases markedly with loading strain: when strain increases from 0% to 0.25%, γ decreases from 579A to 448.1A. When strain increases to 0.40%, γ approaches 0A. This means at strain of 0.40%, there is no certainty that a sample will carry a non-zero superconducting current. From this statistical analysis, one can see that the current carrying performance depends not only on the loading condition but also on individual samples. One question remains: how do samples have such large variation in performance even when they undergo the same manufacturing processes?

One possible explanation is the variation in the electrical performance is caused by the variation in the micro-structure of the superconducting wire, which in turn is highly sensitive to heat treatment parameters. Powder-in-tube method is used in the manufacturing of the Bi2212 wires, in which Bi2212 powder is filled in silver tubes, and then the tubes are drawn to create the untreated or "green" wires. The green wires become superconducting after they have gone through a heat treatment process to create connected, solid Bi2212 filaments from the initial powder. As Figure 1.4(a) shows, there are hundreds of untreated Bi2212 filaments inside a green wire and initially, they are all separated from each other. However, Figure 1.4(b) shows after a heat treatment, there are voids, multiple phases and intergrowth between the filaments.

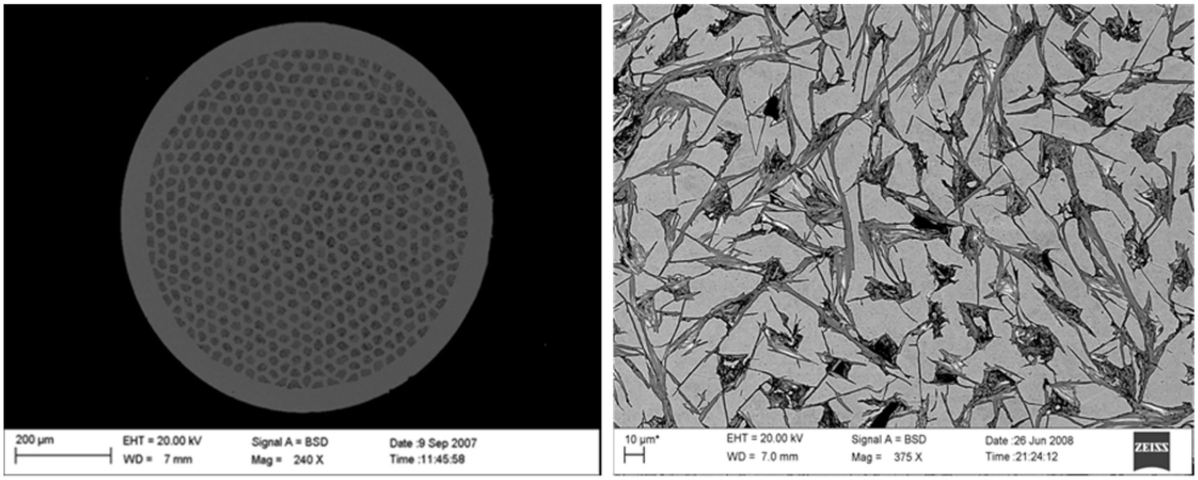

(a) (b)

Figure 1.4. Cross-sectional scanning electron microscopy images of Bi2112 round wires: (a) Before heat treatment, and (b) After heat treatment.

Various heat treatment processes have been implemented and optimized to achieve higher critical current density via improving the microstructure of the conductor. The most well-known processes in treating the wires are partial-melt, split-melt, and saw-tooth process [3, 4]. Figure 1.5 shows the heat treatment schematics of these processes. In a partial-melt heat treatment process, the Bi2212 powder is heated above its peritectic temperature. This melts the Bi2212 powder to liquid and also creates other phases such as alkaline earth cuprate (AEC) and copper-free phases [5]. After that, a slow cooling to room temperature process will allow the Bi2212 phase to re-crystalize from the melt to create connected, superconducting filaments. A split-melt heat treatment process is basically a partial melt heat treatment process that is split into two heat treatment steps.

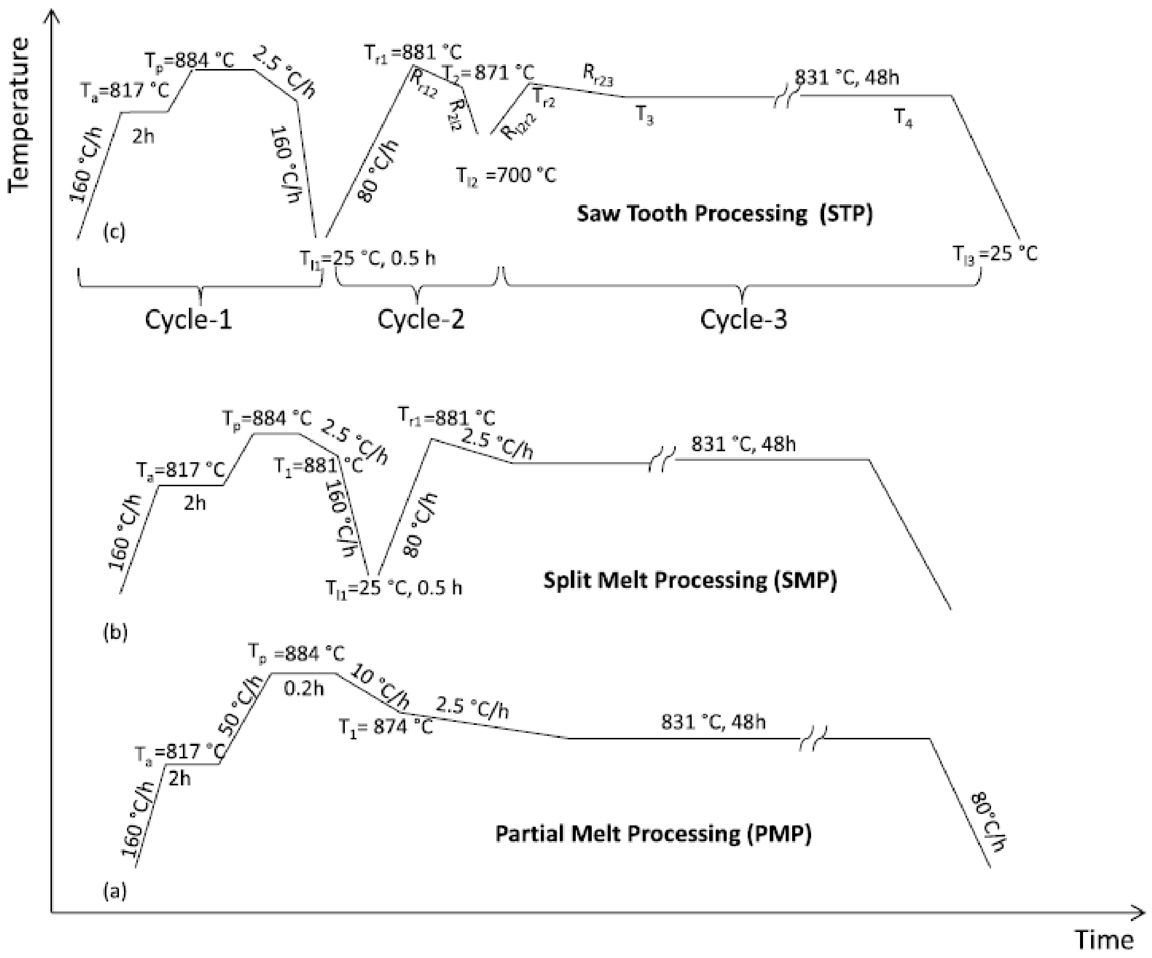

Figure 1.5. Temperature–time schematics (not to scale) of the heat treatment profiles for (a) partial-melt processing, (b) split-melt processing, and (c) saw-tooth processing [3] .

It has been found the split melt process results in 40% increase in critical current in Bi2212 round wires, compared the to the partial melt process [6]. While study [3] shows that a saw-tooth heat treatment process can increase the critical current density 120% at 5 Tesla magnetic field and 70% at self-field, compared to the partial melt heat treatment process.

However, all heat treatment processes are often not 100% effective. As mentioned above, other than the Bi2212 superconducting phase and silver, there are also remaining non-superconducting phases and bubbles/voids. Limiting the amount of these phases is often the underlying mechanism for improving the material's performance.

Bubbles first come from the porosity in the Bi2212 powder, comprising typically about 30% to 40% of the total volume of the powder [5]. In the heat treatment process, impurities and even oxygen from the Bi2212 phase could evaporate thus introduce more gas into the wires. The result is after a heat treatment, there can still be large volume percentage of the wires that is made of bubbles. Figure 1.6(a) shows a tomographic image where there is still significant amount of porosity still inside a wire after a heat treatment. Figure 1.6(b) shows the scanning electron microscopy image of a single filament inside the wire. The filament is cut out to show a hollow core inside the filament.

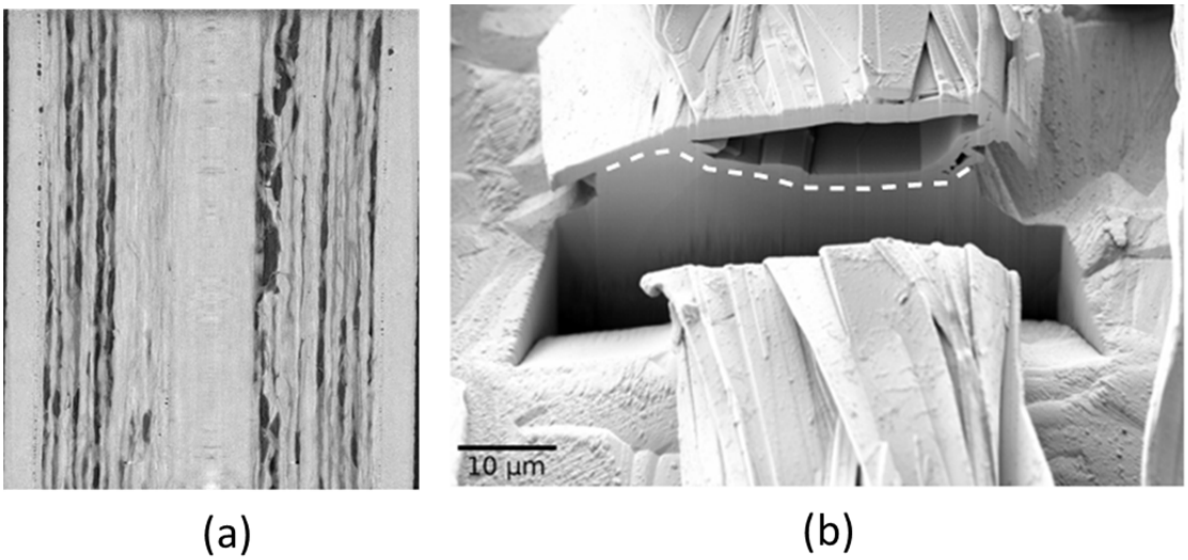

(a) (b)

Figure 1.6. (a) Tomographic image of a heat treated wire, dark gray areas are bubbles. (b) Scanning electron microscopy image of a cut-out Bi2212 filament, showing the hollow core inside it [5].

Bubbles play an important role in the wires' electrical performance. Especially when they become comparable in size to the filaments' diameters as shown in Figure 1.6(b), they can significantly impact or completely block the current flow in the filaments. Thus reducing either the bubbles' size or volume fraction could result in performance improvement. The study [7] shows by cold iso-static pressing at the pressure of 2 GPa on the green wires before heat treatment, critical current density can be more than doubled compared to the regular heat treatment without the pressing. The study shows that, after going through the same heat treatment profile with maximum temperature of 885^{o}C then tested 4.2K and 5T magnetic field, the wire without iso-static pressing achieves a critical current density of 1332 A/mm^2

while the wire with iso-static pressing achieves 3661 A/mm^2. The reason why the cold pressing results in such improvement is it densifies the (untreated) wires, resulting in lower porosity or the volume fraction of the bubbles in the wires. Also, in the study, SEM image analysis of the quenched samples shows a change in shape and size of the bubbles. The wires without cold pressing have elongated bubbles with length about 2-3 times their diameters, while the wires undergoing the cold pressing have smaller and more rounded bubbles.

Similar to bubbles, non-superconducting phases also limit or block the current flow inside the Bi2212 filaments. Thus by reducing their volume fractions, one could also improve the performance of the wires. One of the methods of doing so is the saw-tooth heat treatment process [3]. In the process, by the multiple heating and cooling cycles, more nucleation sites for growing the superconducting phase Bi2212 are formed compared to just one cycle as in the split-melt process. This results in a higher percentage of the superconducting phase Bi2212, and conversely, lower percentages of other non-superconducting phases. Figure 1.7(a) shows an example of a filament where a significant fraction is the non-superconducting phase Bi2201 (light gray) instead of the desired superconducting phase Bi2212 (dark gray). Such filament would not conduct current well. While Figure 1.7(b) shows a dense filament comprised of mostly the Bi2212 phase. It is found in [3] that more filaments of the type in Figure 1.7(b) result in higher overall performance of the wires.

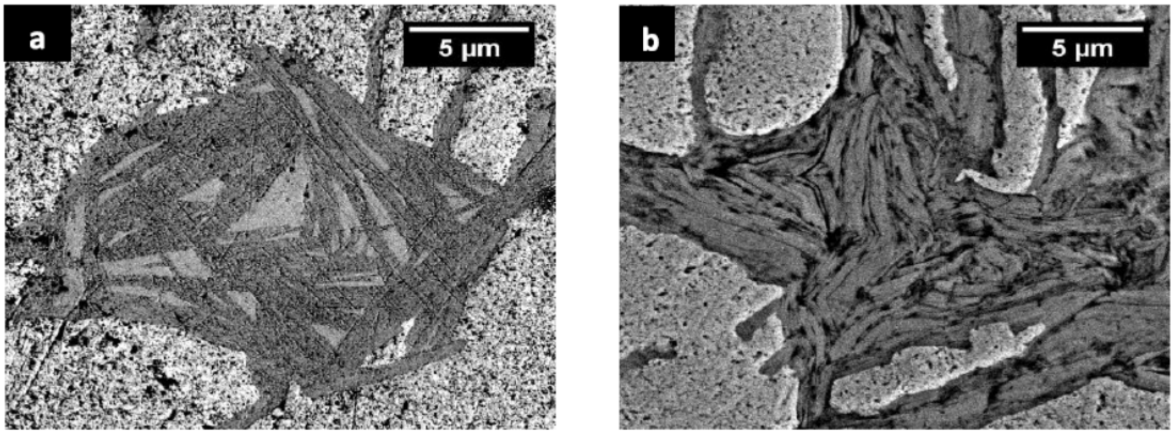

Figure 1.7. Cross-sectional SEM images of (a) filament with significant amount of Bi22012 phase and (b) filament consisting mostly Bi2212 phase [3].

Another important microstructure feature in Bi2212 round wires is the intergrowths between the Bi2212 filaments. In the study [4], it is found that by varying the split and the return temperatures of the split-melt process, there's a significant change in microstructure of the wires and consequently, the electrical performance. Specifically, the amount of intergrowths between the superconducting filaments is highly dependent on both the split and the return temperatures. Figure 1.8 (a) shows an example cross-sectional SEM image of the wire, while Figure 1.8(b) shows the transformed image of Figure 1.8(a) by analyzing and marking the superconducting areas different colors by different thicknesses. The red color corresponds to areas with half-width from 0 to 1 micron, yellow: 1 to 2 microns, green: 2 to 3 microns, blue: 3 to 4 microns, black: larger than 4 microns.

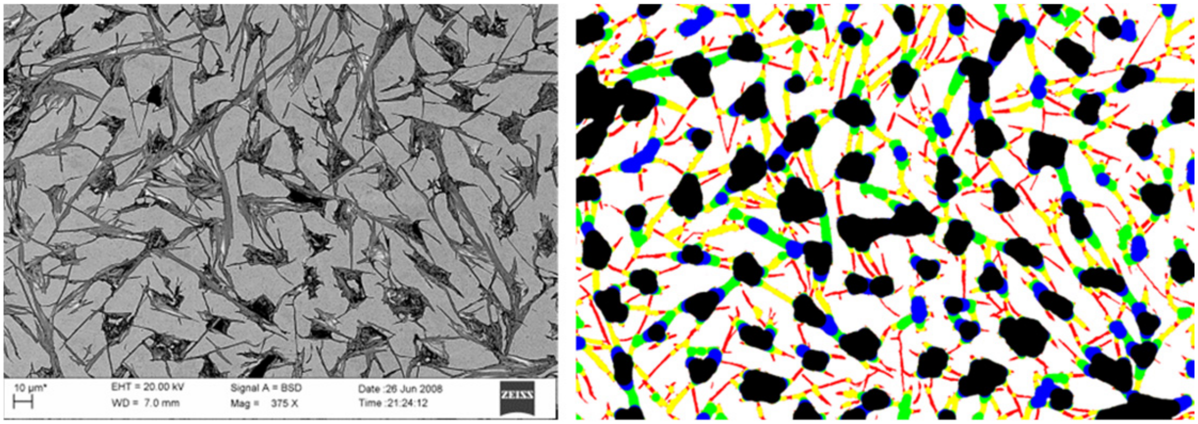

(a) (b)

Figure 1.8. (a) Original cross-sectional SEM image analysis of Bi2212 wire showing intergrowths between the filaments. (b) Image analysis: bridges with different widths are marked with different colors from red to blue.

By analysis of SEM images of multiple wires then matching the results with heat treatment profiles, relationships between bridges growth and heat treatment temperatures are established [4]. Figure 1.9(a) shows the correlation between the split temperature and the volume percentage of bridges/intergrowths. Similarly, Figure 1.9(b) shows the correlation between return temperature and the bridges volume percentage. In the range of the temperatures investigated, there is a positive relation between the temperatures and the bridges volume fraction.

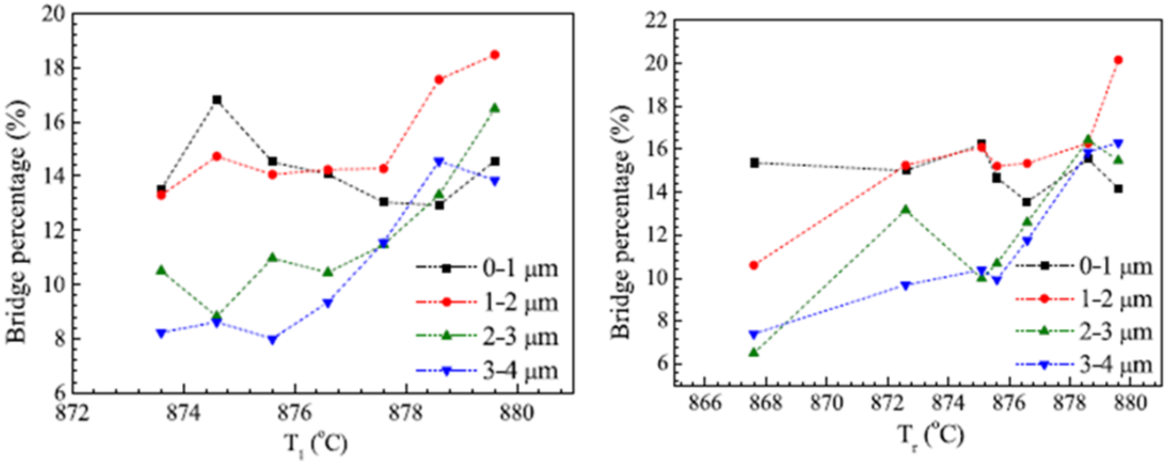

(a)

(b)

Figure 1.9. (a) Relationship between split temperature and bridge size and bridge area percentage. (b) Relationship between return temperature and bridge size and bridge area percentage [4].

Also, matching the image analysis results with data on critical current densities of the wires shows the strong correlation between bridge percentage and electrical performance. More specifically, Figure 1.10 shows that when the bridges are categorized by sizes, the larger bridges (Figures 1.10(c) and 1.10(d)) have a strong positive correlation with effective critical current density.

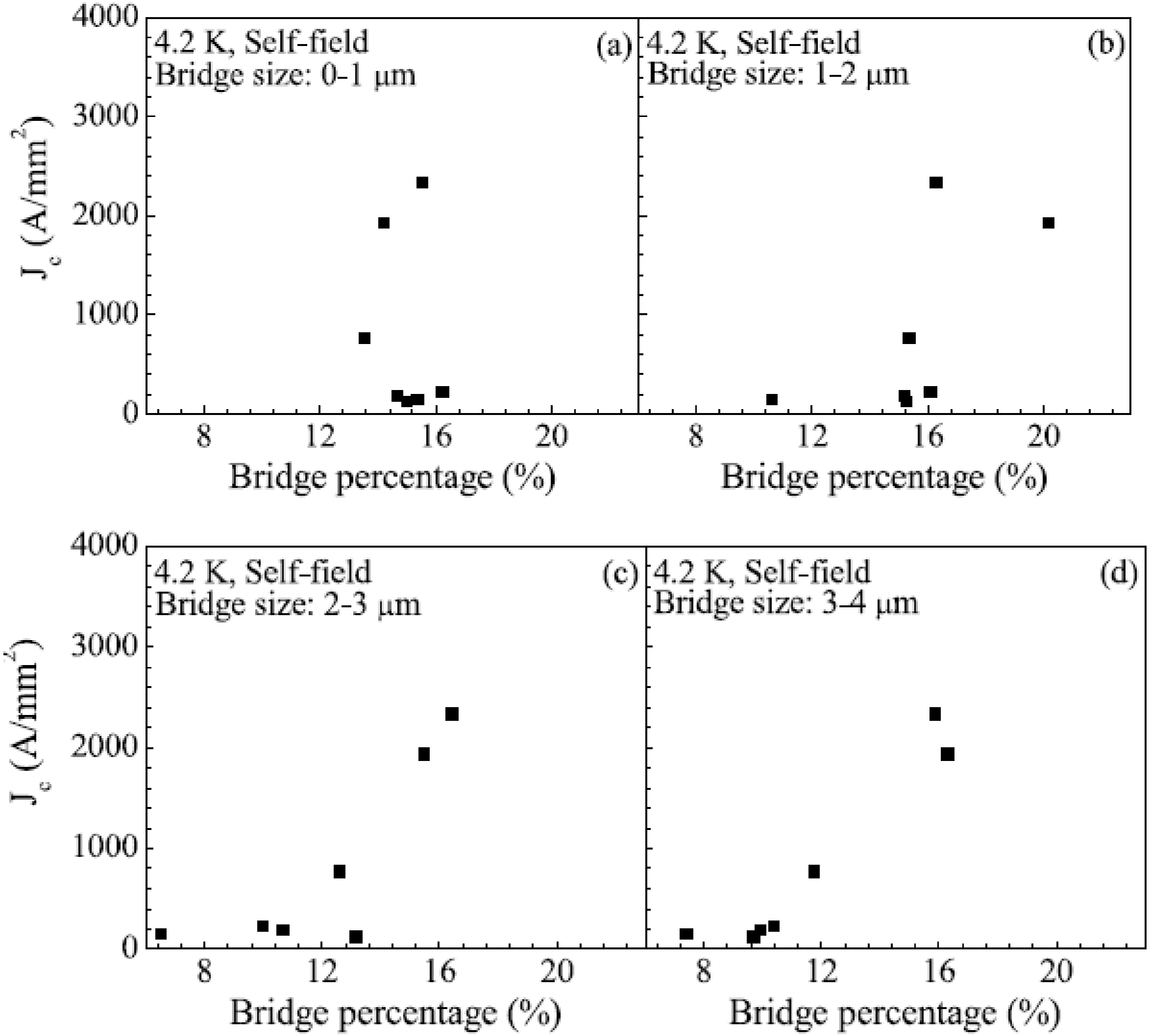

Figure 1.10. Relationship between 4.2 K, self-field Je, bridge size and bridge area percentage (of the non-Ag area) with bridges size, (a) 0–1 μm; (b) 1–2 μm; (c) 2–3 μm and (d) 3–4 μm [4].

One possible explanation for this behavior is the intergrowths enhance the connectivity of the Bi2212 filaments by connecting them together to form a single network. As shown previously, there are bubbles and non-superconducting phases inside Bii2212 filaments. They can severely limit the current running through them or even block the current completely. When this happens in a filament, the intergrowths allow other pathways for the current to flow from the blocked filament to other ones. In other words, the relationship between the filaments and the intergrowths is similar to a system of highways and detours. When one highway gets congested, traffic can redirect to detours to get into other highways. This enhanced connectivity results in higher electrical performance. The reason why thicker bridges have more influence than thinner bridges on performance could be simply because the thicker bridges can bypass a higher electric current from filament to filament because of their bigger sizes. Also, another possible explanation is thicker bridges tend to be made of single grain, while thinner bridges can be formed from joined grains with different orientations [8]. Grain boundaries (especially high angle ones) are barriers to superconducting currents. Thus qualitatively the single grain bridges can carry currents better than the multi-grain bridges.

While microstructure certainly has great influence on the electrical performance of Bi2212 wires under zero mechanical load, microstructure also plays an important role on how the wires deform under applied strain and ultimately, critical current under non-zero strains. As shown previously in [2], statistical analysis shows strong dependence of critical current on the applied strain in the sample. There have been studies aim to explain the role of microstructure in electrical performance under strain [9, 10]. Figure 1.11 shows a descriptive model on critical current – strain relationship. In tensile strain region, the strain-critical current relationship in Bi2212 wires exhibits reversible behavior when the strain is smaller than a critical value and irreversible/degrading behavior when the strain is higher than the critical value.

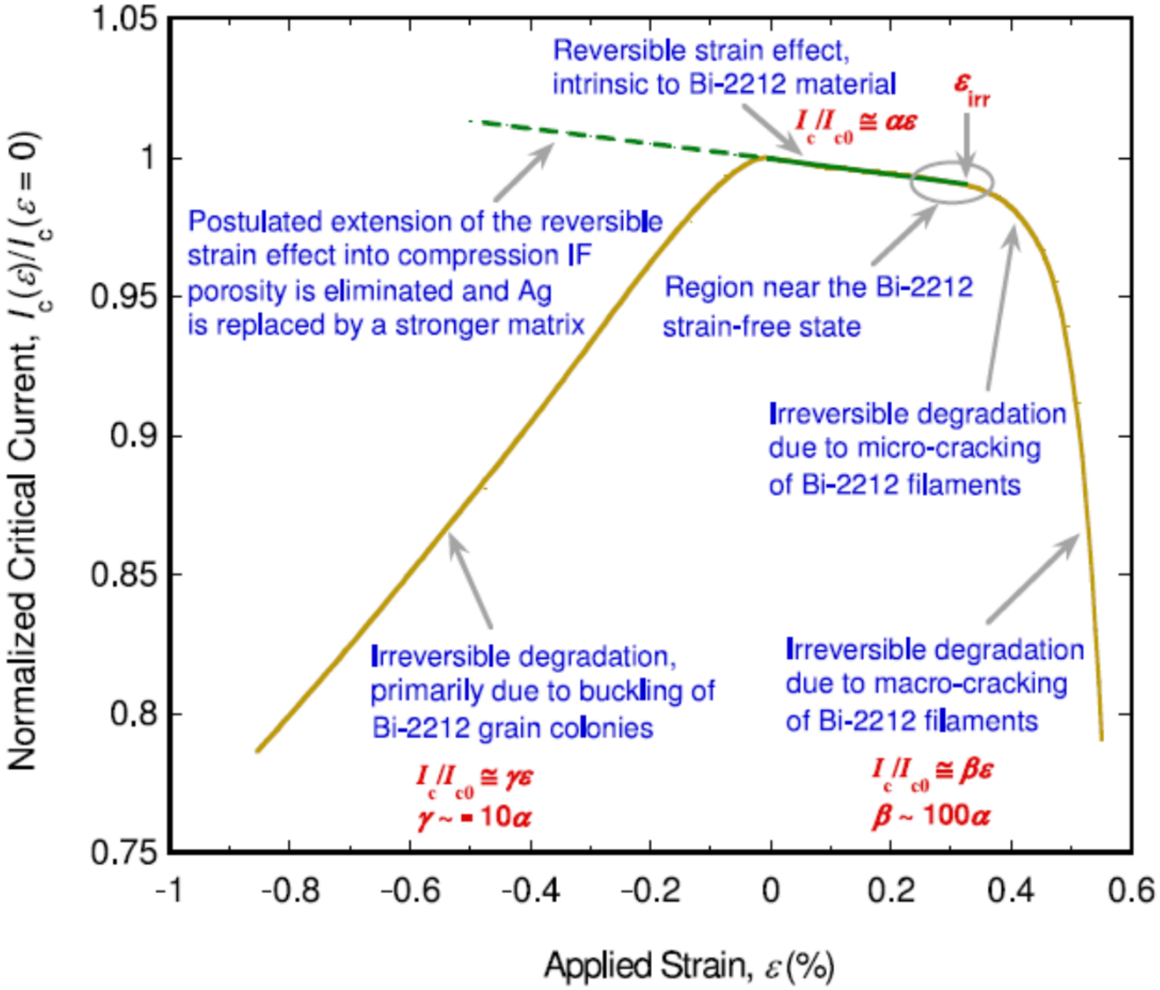

Figure 1.11. Dependence of critical current on compressive and tensile strains in Bi2212 in modified descriptive strain model [10].

Experimentally, it has been found that this threshold strain value varies from wire to wire, with the average value about 0.31% in tension. From zero to 0.31% applied tensile strain, the critical current slightly decreases when the applied strain increases. In the study, it is considered that in this region, the Bi2212 phase is actually in the compressive state. The reason is due to differences in thermal expansion coefficients, when the Bi2212 wire is cooled from room temperature to cryogenic temperature where experiments are taken, the B-i2212 phase will be in compression stress/strain state, while silver is in expansion state. So the externally applied strain in this region only alleviates the internal compression already present in the B-i2212 phase, and around the critical applied strain 0.31% is where the externally applied strain neutralizes the internal strain in Bi2212. The irreversible degradation of critical current at strains larger than 0.31% is stipulated as the result of the cracking in Bi2212 filaments in tension.

Intrinsically, Bi2212 material itself has higher critical current in compression [10]. This explains why in Figure 1.11 the critical current decreases when the externally applied tensile strain goes up from zero to 0.31%, this is because the compression is neutralized in the process. But conversely, when the applied strain goes in the compression direction, the studies [9, 10] show there is no increasing in critical current density as expected from the intrinsic property of Bi2212 material. Instead, the critical current shows immediate irreversible degradation. The studies postulate that in this region, the intrinsic property of Bi2212 is overshadowed by another phenomenon in Bi2212 wire under compression: buckling of thin Bi2212 columns under compression. SEM images from [10] show regions inside the wire where the Bi2212 grains grow into columnar shapes and without much support from the silver matrix. Although the descriptive models are reasonable, there need more understandings as well as quantitative experiments to confirm the suggestions of the models. However, due to the micro-scale of the features in Bi2212 wires, experimental approaches would face significant difficulties to be conducted at such as small scale.

So far, it has been found that that bubbles, non-superconducting phases, and filament shapes and inter-filamentary bridges all play important roles in the electrical performance for the Bi2212 round wires. But how do they influence the mechanical behavior? For example, do wires with bubbles have lower strength than wires without them, and how much lower? Or how do the spatial arrangements of different phases affect the relationship between local strain and the macroscopic strain? The micrometer scale of these features in Bi2212 round wires make it difficult for experimental approaches to correlate a specific microstructure feature to the material's mechanical behavior, since each wire can contain multiple features. Since mechanical experiments on these wires are usually implemented on macroscopic scale, it is challenging to correlate some specific microstructure features and the macroscopic properties.

There have been few computer simulation approaches to investigate behavior of Bi-2212 round wires. The simulations are mainly on magnetic and electrical properties of the wires [11-14]. The main reason it is difficult to simulate mechanical behavior of the wires is as shown in previous picture, the wires have very complex microstructure with multiple phases and defects. Especially, the interfaces between phases often have irregular, jagged edges with sharp corners. Also, there are discontinuities such as cracks present in the wires. All these pose significant challenges for traditional approaches using classical mechanics equations to investigate the system’s behavior. The reason is classical mechanics rely on partial differential equations to establish the constitutive stress-strain relationship in the material. Classical approaches using finite element method usually requires rounding off the geometry at those sharp corners.

In order to eliminate those rough edges/sharp corners, in [15] a fractal analysis is used to re-generate the microstructure of the Bi2212 wires. In the study, a longitudinal SEM image of Bi2212 filament is used to analyze the irregular shape of the boundary between the Bi2212 filament and the silver matrix. A fractal dimension number is assigned to this boundary line. Then using computer simulation, fractal curves of the same fractal dimension number (as the original line) are generated. Figure 1.12(b) shows a simulated microstructure in which, two fractal curves are used for generating the Bi2212/silver interface. The computer generated fractal curves in Figure 1.12(b) have the same fractal dimension of the real silver/Bi2212 boundary curves obtained from the Figure 1.12(a). The computer generated fractal curves have the advantage of being mathematically smooth, thus eliminate the sharp corner problem. However, though the simulated microstructure is equivalent to the microstructure from the original image in terms of fractal dimension, their shapes are not the same. Thus the simulations are not performed on the real microstructure.

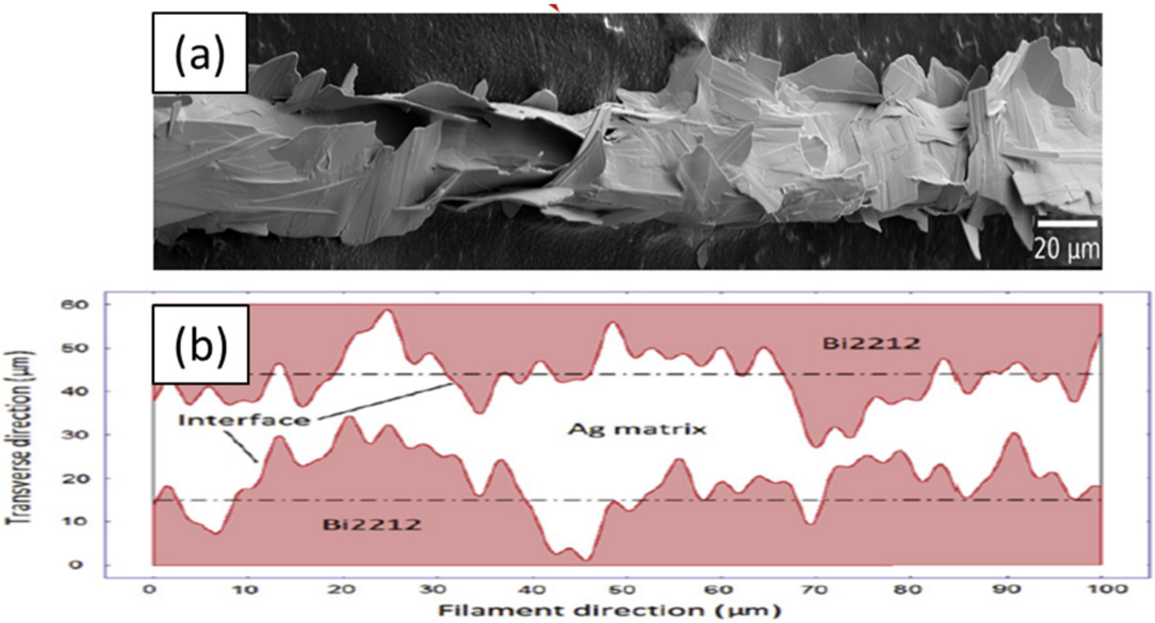

Figure 1.12. Original and simulated microstructures using fractal analysis [15].

Figure 1.13 shows the von-Mises stress distribution in the simulated microstructure. Stress concentration factor ranging from 1.5 to 2.5 is found in the system. However, since the simulated microstructure does not have the same shape as the original SEM image, it's still a remaining question whether the real microstructure would have the same behavior as that of the simulated microstructure.

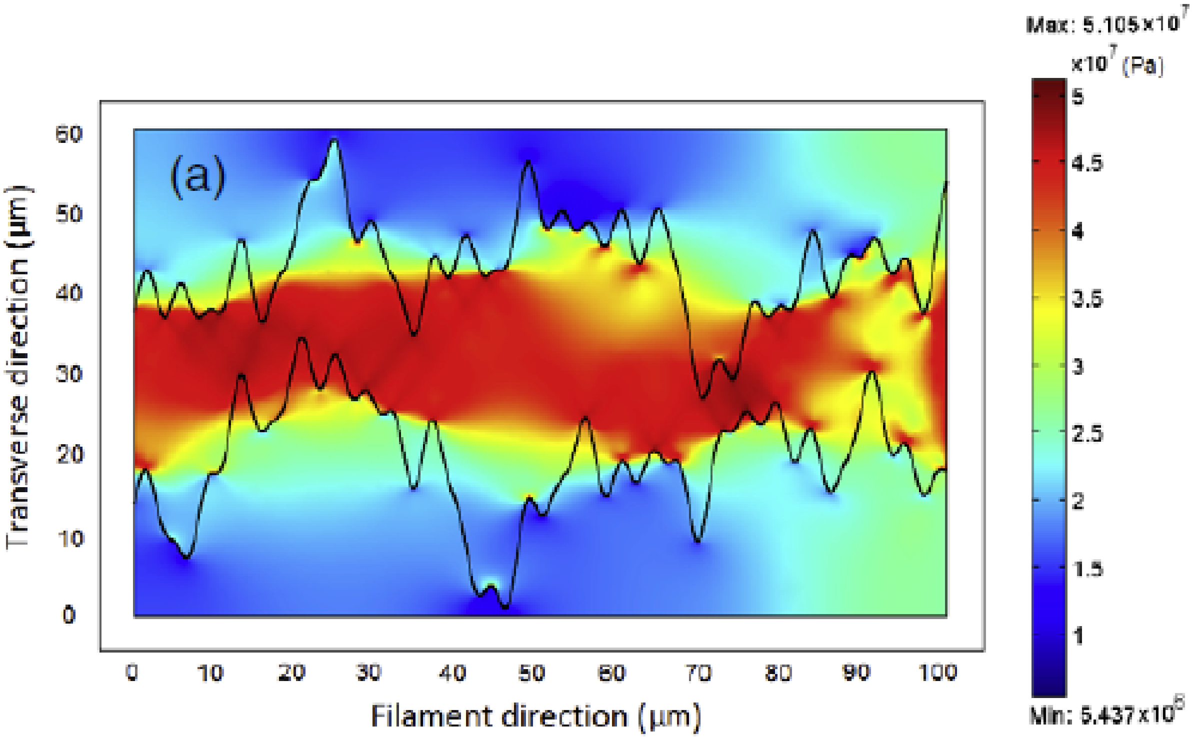

Figure 1.13. Steady-state von-Mises stress distribution with fixed load of 60 N/m to simulated microstructure [15].

1.4. Peridynamic Theory

1.4.1. Peridynamics as a Non-local Theory

As shown previously, there are significant challenges simulating the mechanical behavior of Bi2212 round wires using traditional approaches because of sharp corners and discontinuities. This is because in classical mechanics, interactions only happen over infinitesimal distances, and the theory is based on spatial derivatives for its formula. This leads to difficulties at discontinuities such as cracks, since the spatial coordinates are undefined there. Thus one needs to redefine the body and its boundary so the cracks are on the boundary [16]. Also, at phase boundary where coordinates are defined and continuous, their spatial derivatives are not continuous - there is a jump at the interface. This also requires classical mechanics to define the phase boundary and its corresponding boundary conditions. For a composite material with complex phase structure, this could lead to complex boundary problems. So far, finite element method (FEM) is the most commonly used to simulate mechanical behaviors of a material or system. Since FEM is based on partial differential equations, stress and strain singularities at sharp corners create undefined derivatives at these regions, resulting in convergence problems. Especially in materials with complex phase arrangements where there are many “sharp corners” at the phase boundaries or voids, FEM faces significant difficulties. Partial differential equations are also limited with respect to systems with discontinuities such as cracks. Additional modeling techniques, such as adaptive meshing, are required to model the growth of an existing crack.

In order to solve these difficulties with classical mechanics, another approach was developed by Stewart Silling [16] with the peridynamics theory. The theory name comes from the words “peri” which means “near” and the root “dyna” which means “force”, which reflects the basis of the theory: a non-local mechanics theory. In peridynamics, interactions between peridynamics volumes happen over finite distances, similar to molecular dynamics. So from the application point of view, the peridynamics can be viewed as an upscaled molecular dynamics theory [17, 18]. In fact, some peridynamic models have been implemented as a part of the molecular dynamics software LAMMPS, developed by Sandia National Laboratories [19]. The main difference with molecular dynamics is while molecular dynamics involves interactions between discrete points, in peridynamic theory material points are continuous, like in classical mechanics. It is just that in practice of computer modeling and simulation, the continuum peridynamic body is approximated by a discrete set of peridynamic nodes. Finally, the difference between peridynamics and classical mechanics is peridynamics uses integral equations instead of partial derivative equations for its formulas, and the force interactions happen over a finite distance instead of contact/ local forces.

Figure 1.14 shows the schematic of interaction between 2 points in peridynamic theory. In the figure, each peridynamic point interacts with all other points around it within a cut off distance δ called the horizon.

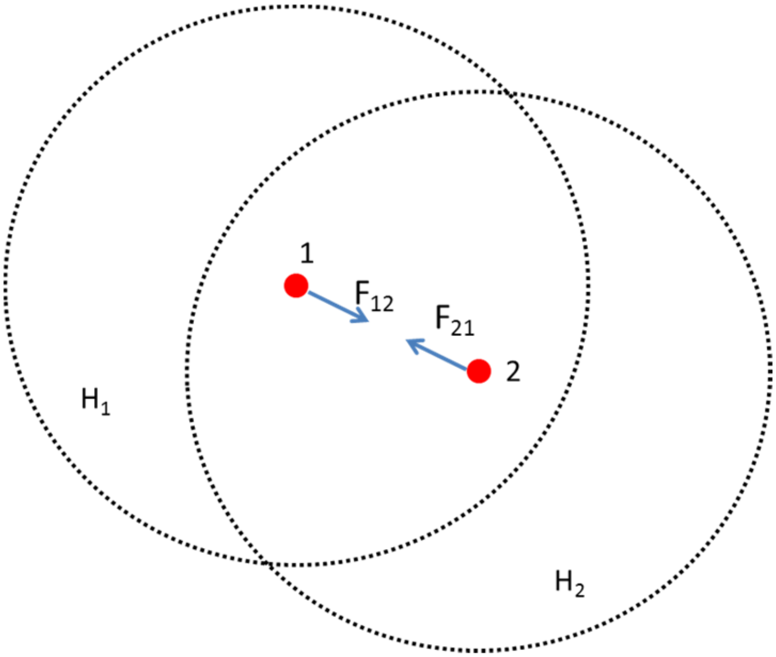

Figure 1.14. Interaction forces between 2 points in an ordinary peridynamic system.

In peridynamics, the motion of a point depends on forces other points acting on it:

$$\rho(\mathbf{x})\ddot{\mathbf{u}}(\mathbf{x},t) = \int_{\mathrm{H}} \mathbf{f}(\mathbf{x}',\mathbf{x},t)\, \mathrm{d}V_{\mathbf{x}'} + \mathbf{b}(\mathbf{x},t) \tag{1.1}$$

where $\rho(\mathbf{x})$ is the mass density at reference point **x** (kg/m^3). **u** is the displacement of point **x** at time *t*. H is the neighborhood region of point **x** containing all points that interact with it. The region of H depends on the specific peridynamic model, usually it is defined as a region around the point x within the cut off distance δ as illustrated in Figure 1.14. $\mathbf{f}(\mathbf{x}',\mathbf{x},t)$ is the force density the reference point **x** act on reference point **x** at time *t*: **f** has the unit of Newton/m^6. $\mathrm{d}V_{\mathbf{x}'}$ is the differential volume at point **x'** (m^3). And $\mathbf{b}(\mathbf{x},t)$ is the externally applied body force at point **x** and time *t* (Newton/m^3). To satisfy Newton's third law, the function **f** is anti-symmetric:

$$\mathbf{f}(\mathbf{x}',\mathbf{x},t) = -\mathbf{f}(\mathbf{x},\mathbf{x}',t) \tag{1.2}$$

Also, when **f** is anti-symmetric, the linear momentum conservation of a peridynamic system is satisfied, as shown in [20]. The specific dependence of force $\mathbf{f}(\mathbf{x}',\mathbf{x},t)$ on bond deformations determines how a peridynamic system behaves and is called the constitutive equation.

There are two types of peridynamic models: bond based and state based models. In the bond based model, force interaction between two peridynamic points depends only on their relative position/displacement. While in state based models, the interaction force between two points depends on the relative deformations of all other points inside the neighborhoods of both points. The vast majority of peridynamic applications use the bond based model since it is the first model introduced in peridynamics. In a 3D, bond based model for linearly elastic solid by Silling and Askari [21], peridynamic constitutive equation is:

$$\mathbf{f}(\boldsymbol{\eta},\boldsymbol{\xi}) = \frac{\boldsymbol{\eta}+\boldsymbol{\xi}}{|\boldsymbol{\eta}+\boldsymbol{\xi}|}cs \tag{1.3}$$

where $\boldsymbol{\xi}$ is the original relative position of the point exerting force on the point of interest, $\boldsymbol{\xi}$ is also called the bond vector, $\boldsymbol{\eta}$ is the relative displacement and $\boldsymbol{\xi}+\boldsymbol{\eta}$ is the deformed bond vector. Figure 1.15 shows the physical presentation of those vectors when a peridynamic body is in deformation. In the figure, point 1 moves a distance $\mathbf{u}_1$, while point 2 moves a distance $\mathbf{u}_2$. Thus the relative displacement of point 2 to point 1 is:

$$\boldsymbol{\eta} = \mathbf{u}_2 - \mathbf{u}_1 \tag{1.4}$$

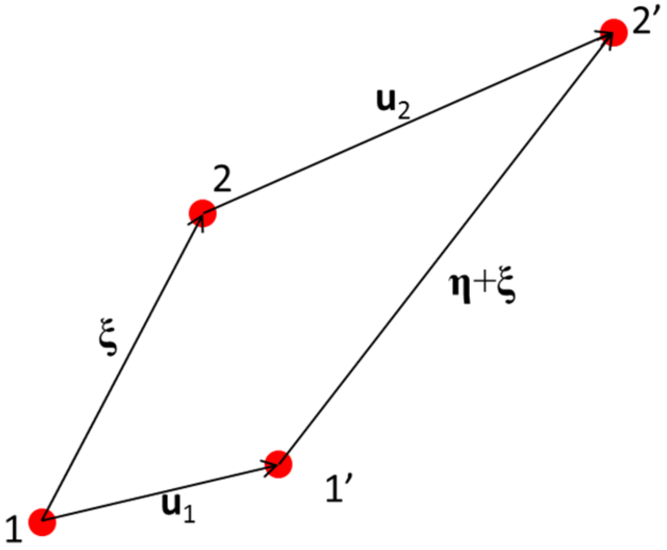

Figure 1.15. Undeformed and deformed peridynamic bonds.

s is the bond stretch which is defined as:

$$s = \frac{|\boldsymbol{\eta}+\boldsymbol{\xi}|-|\boldsymbol{\xi}|}{|\boldsymbol{\xi}|} \tag{1.5}$$

c is a constant named micromodulus, and this bond based model is called the prototype microelastic brittle (PMB) model . The interaction between two points in this peridynamic model is like that of a spring: the direction of the force is parallel to the deformed bond vector, while the magnitude is proportional to the relative displacement from the original/equilibrium position. By comparing the strain energy density of this model and that of classical mechanics, the authors find that this PMB model is equivalent to a classical mechanic elastic model with a Poisson's ratio of 1/4, and the micromodulus *c* is related to the bulk modulus *k* by the equation:

$$c = \frac{18k}{\pi\delta^4} \tag{1.6}$$

Where δ is horizon size mentioned previously. Although this model is a linearly elastic model, mathematically the model is not linear. The reason is although the interaction force is linear to the bond elongation, it is not linear to the material coordinates. A linearized bond based model based on this model has been proposed in [22]. Also, a generalized PMB model is proposed by Seleson and Parks in [23] by adding a function named influence function to the constitutive equation:

$$\mathbf{f}(\boldsymbol{\eta}, \boldsymbol{\xi}) = \frac{\boldsymbol{\eta}+\boldsymbol{\xi}}{|\boldsymbol{\eta}+\boldsymbol{\xi}|}\underline{\omega} c s \tag{1.7}$$

The micromodulus c of this generalized PMB model takes the form:

$$c = \frac{18k}{\int_H |\boldsymbol{\xi}|^2 \underline{\omega_s}\langle|\boldsymbol{\xi}|\rangle dV_{\boldsymbol{\xi}}} \tag{1.8}$$

s is the bond stretch defined above. The influence function $\underline{\omega}$ is a scalar function of the undeformed bond vector $\boldsymbol{\xi}$. In most researches, the influence function is chosen to be dependent on the bond length only but not the bond direction, $\underline{\omega}\langle|\boldsymbol{\xi}|\rangle = \underline{\omega}_s\langle|\boldsymbol{\xi}|\rangle$. Influence function is used to give different weight contributions to different point, usually to give closer points greater weights of force than points further away. Constant, inverse polynomial, triangle/conical, and Gaussian functions have been used for influence function in various studies [23-30]. Figure 1.16 gives a graphical presentation of these functions. Note that all the functions are cut off at the bond length $|\boldsymbol{\xi}| = \delta$.

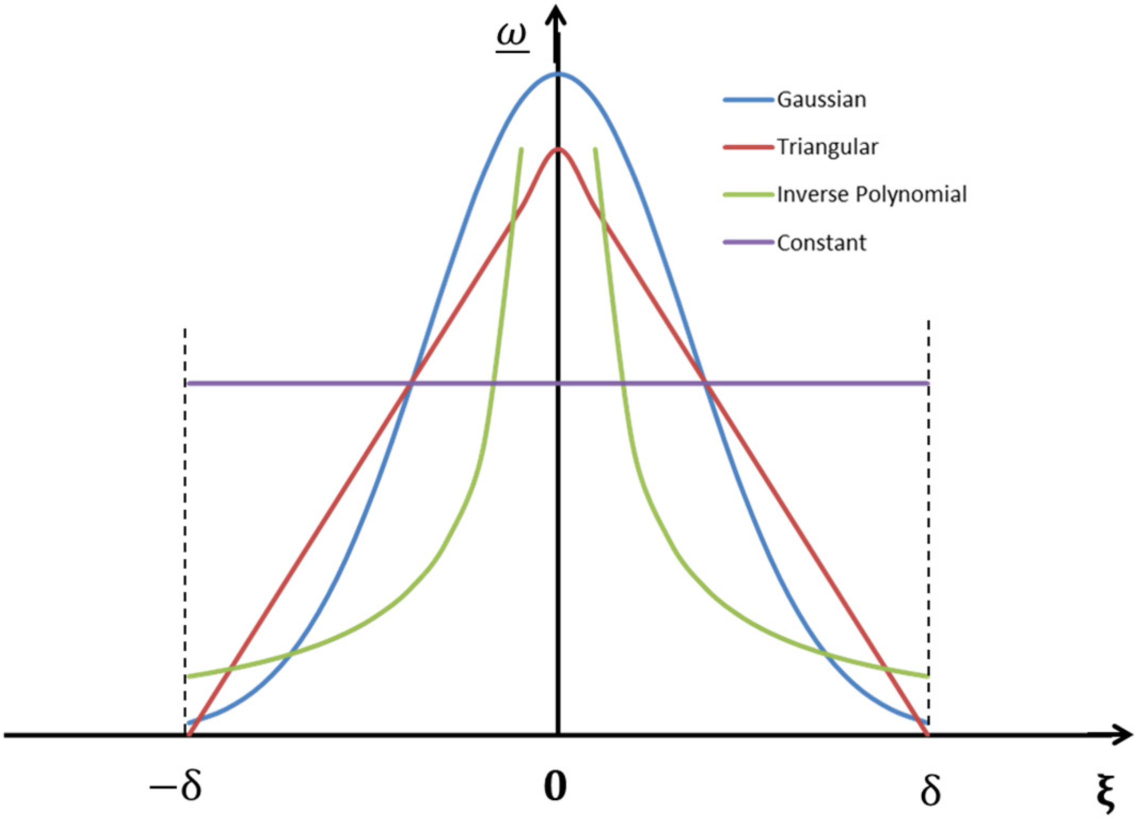

Figure 1.16. Dependence of different influence functions on bond vector.

The PMB and generalized PMB models above are 3D models, meaning each peridynamic point has a spherical neighborhood. Development of constitutive equations for 1D and 2D bond based models has been proposed in [26, 31-33]. The bond-based models can only have a fixed Poisson's ratio =1/4 in 3D and 1/3 in 2D plane stress [32, 34]. This is the main limitation of the bond-based model, because in reality materials have a wide range of Poisson's ratio. Especially in composite materials, where the difference in Poison's ratio in different phases has important influences on mechanical stress, the bond-based models would not be able to account for such influences. State-based peridynamics was developed to solve this limitation.

In a state-based peridynamic system, the force density **f** is decomposed into two parts [34]:

$$\mathbf{f}(\mathbf{x}',\mathbf{x},t) = \underline{\mathbf{T}}[\mathbf{x},t]\langle\mathbf{x}'-\mathbf{x}\rangle - \underline{\mathbf{T}}[\mathbf{x}',t]\langle\mathbf{x}-\mathbf{x}'\rangle \tag{1.9}$$

$\underline{\mathbf{T}}[\mathbf{x},t]\langle\mathbf{x}'-\mathbf{x}\rangle$ is called the force vector state. In peridynamic theory, a state is a function that takes the bond vector $\boldsymbol{\xi} = \mathbf{x}' - \mathbf{x}$ as input and produces an output which could be a scalar or a vector. The variable or input of a peridynamic state is written in angle brackets. In this case, **T** takes a vector input and produces another vector output. Note that output of **T** has the same unit as that of the force density **f**: force/volume^2, or N/m^6. $\underline{\mathbf{T}}[\mathbf{x},t]$ is similar to the concept of second order tensors in classical mechanics: it uses the bond vector $(\mathbf{x}'-\mathbf{x})$ as input and produces another vector as output. The main difference with tensors is: **T** does not always have to be linear or even continuous. In state-based peridynamics, the formula of $\underline{\mathbf{T}}[\mathbf{x},t]\langle\mathbf{x}'-\mathbf{x}\rangle$ depends on deformations of all bond vectors in the neighborhood of **x,** not just the bond vector $\boldsymbol{\xi} = \mathbf{x}' - \mathbf{x}$. The state based peridynamic model can be formulated for both solids and fluids. The peridynamic fluid model can be set up simply by setting the shear modulus in the model to zero. In [34], a 3D ordinary model for linear peridynamic solids is proposed. In the model, the force state is set as: $\underline{\mathbf{T}} = \underline{t}\mathbf{M}$, where **M** is the unit vector along the deformed bond direction and t is a scalar named force scalar state (see [34], equation (43)). For linearly elastic solids, the peridynamic formula of t in the 3D model is:

$$t = \frac{-3k\theta}{q}\underline{\omega x} + \alpha\underline{\omega e}^{d} \tag{1.10}$$

where

$$\theta = 3\frac{\underline{\omega x}\bullet\underline{e}}{q} \tag{1.11}$$

$$\underline{e}^{\mathrm{d}} = \underline{e} - \frac{\theta\underline{x}}{3} \tag{1.12}$$

θ is the called the volumetric strain, which is equal to the volume dilatation one would obtain by taking the trace of the strain tensor in classical mechanics when horizon size is small enough so that the strain field could be considered uniform within the neighborhood of the point of interest. $\underline{\omega}\langle\boldsymbol{\xi}\rangle$ is the influence function mentioned previously. $\underline{x}$ is the position scalar state whose value at a bond vector $\boldsymbol{\xi}$ is the scalar bond length $|\boldsymbol{\xi}|$; and $\underline{e}$ is the extension scalar state whose value at a bond vector $\boldsymbol{\xi}$ is the bond elongation, which is the difference between the deformed and undeformed bond lengths. $\underline{e}^{\mathrm{d}}$ is the deviatoric part of the extension state $\underline{e}$: $\underline{e}^{\mathrm{d}} = \underline{e} - \frac{\theta\underline{x}}{3}$. q is the weighted volume, defined as the dot product of the influence function and the position scalar state, $q = \underline{\omega x}\bullet\underline{x}$. The dot product (●) of two peridynamic states is defined in [34], equation (11). In the case where two peridynamic states are scalars as in this case, then the dot product is simply the integration of their regular product over the neighborhood region [34]:

$$\mathbf{A}\bullet\mathbf{B} = \int_{H} \mathbf{A}\langle\boldsymbol{\xi}\rangle\mathbf{B}\langle\boldsymbol{\xi}\rangle dV_{\boldsymbol{\xi}} \tag{1.13}$$

The scalar constants k and α can be chosen so the peridynamic solid corresponds to a classical elastic solid. By equalizing the peridynamic and classical strain energy density for the same deformation, it is found that k is equal to the bulk modulus, while α is related to the shear modulus μ by the formula:

$$\alpha = \frac{15\mu}{q} \tag{1.14}$$

This 3D state based model is also linear to the bond elongation but not to the material coordinates. Linearized theory of state based peridynamics has been proposed in [35]. Recently, there has been development frame work for modeling plasticity with peridynamics [36, 37].

One advantage of the peridynamic models is that they can incorporate cracking behavior natively without any additional equations. In both bond based and state based models, this is simply done by setting a peridynamic bond to break irreversibly when it gets longer than some critical value. Once a bond breaks, there will be no interaction between the two peridynamic points. In the study by Silling and Askari [21], a bond is broken if its bond stretch is larger than a critical value s_0. They also show that for the 3D PMB model, the critical stretch is related to the energy release rate G_0 by:

$$s_0 = \sqrt{\frac{5G_0}{9k\delta}} \tag{1.15}$$

To calculate the degree of damage, a history-dependent function that takes the values of either 1 or 0 is introduced [21]:

$$\mu(\mathbf{x}, t, \boldsymbol{\xi}) = \begin{cases} 1 \text{ if } s(\mathbf{x}, t', \xi) < s_0 \text{ for all } 0 \leq t' \leq t \\ 0 \text{ other wise} \end{cases} \tag{1.16}$$

The damage index, representing the portion of bonds connected to a peridynamic point, thus can be calculated by:

$$\varphi(\mathbf{x}, t) = 1 - \frac{\int_{H_{\mathbf{x}}} \mu(\mathbf{x}, t, \boldsymbol{\xi}) dV_{\boldsymbol{\xi}}}{\int_{H_{\mathbf{x}}} dV_{\boldsymbol{\xi}}} \tag{1.17}$$

By making maps of damage index, cracking patterns in peridynamics can be visualized and studied. Most of dynamic simulation studies in peridynamics focus on the cracking behavior and pattern. The dynamic behavior of a peridynamic system depends strongly on the choice of horizon size. Peridynamic simulations of crack propagation when dynamic load is applied on the sample boundaries show that the propagation speed is dependent on the horizon size [26, 38]; but when the mechanical load is applied directly on the crack surface, study by Bobaru and Hu [38] shows crack propagation speed is largely unaffected by the choice of horizon size, as illustrated by Figure 1.17. It is explained that in the previous case, there is interaction between the propagating crack and the reflected stress waves from the sample boundaries. The magnitude and frequency of these waves depend strongly on horizon size [16, 38], that is why in that case the crack propagation speed also depends on horizon size.

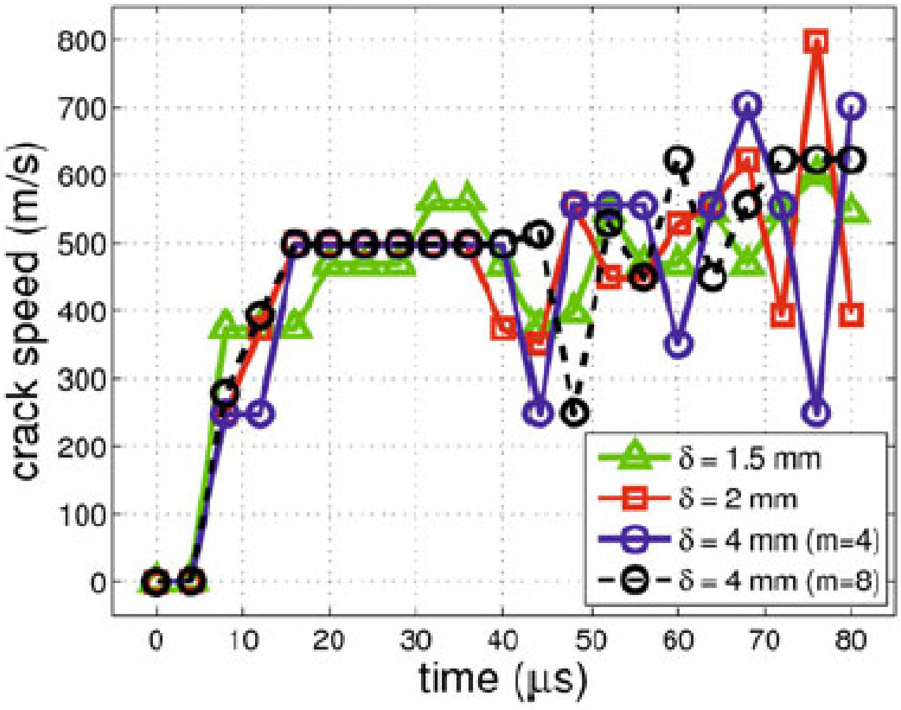

Figure 1.17. Crack propagation speed with three different horizon sizes [38].

The shape of the influence function also has influences on the dynamic behavior of a peridynamic system. In the study [23], the authors use the influence function of the forms:

$$\underline{\omega}\langle\boldsymbol{\xi}\rangle = \left(\frac{1}{|\boldsymbol{\xi}|+\epsilon}\right)^p \tag{1.18}$$

and $\underline{\omega}\langle\boldsymbol{\xi}\rangle = \left(\frac{1}{|\boldsymbol{\xi}|}\right)^p$ (1.19)

Where ϵ and p are constants. In both formulas above, the higher the value of p, the more weight the shorter bonds have compared to the longer bonds in the interactions of peridynamic points. By using a 1D, bond-based peridynamic model for plane wave, the researchers find that p has significant influence on the dispersion relation between the angular frequency Ω and wave number k. When values of *p* are small, peridynamic dispersion curve shows significant difference from the linear relationship (which is typical of classical mechanics), as shown in Figure 1.18. In fact, when *p* is negative, Figure 1.18(b) even shows a range where Ω even decreases when k increases. When *p* is positive and large, the peridynamic dispersion curve becomes linear just like in classical mechanics. This is understandable because the higher than value of *p*, the more local the peridynamic system becomes.

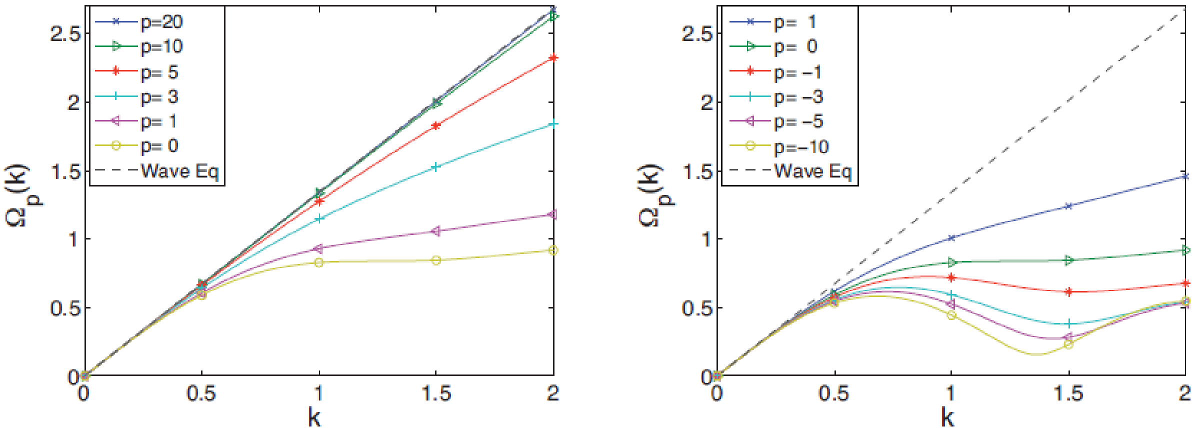

(a) First Example (b) Second Example

Figure 1.18. Dispersion relations for various values of p. (a) with influence function in equation (1.18). (b) with influence function in equation (1.19) [23].

The choice of *p* also influences results in a dynamic fracture simulation using peridynamics [23]. Figure 1.19 shows 3D, bond-based peridynamic simulation results of an impact between a hard sphere and a brittle disc at 5×10^{-5} s after impact. Only the brittle disc is shown on the figure from the top down view, the colors denote the damage index. From the figure it can be clearly seen the crack or damage pattern is strongly dependent on the choice of p.

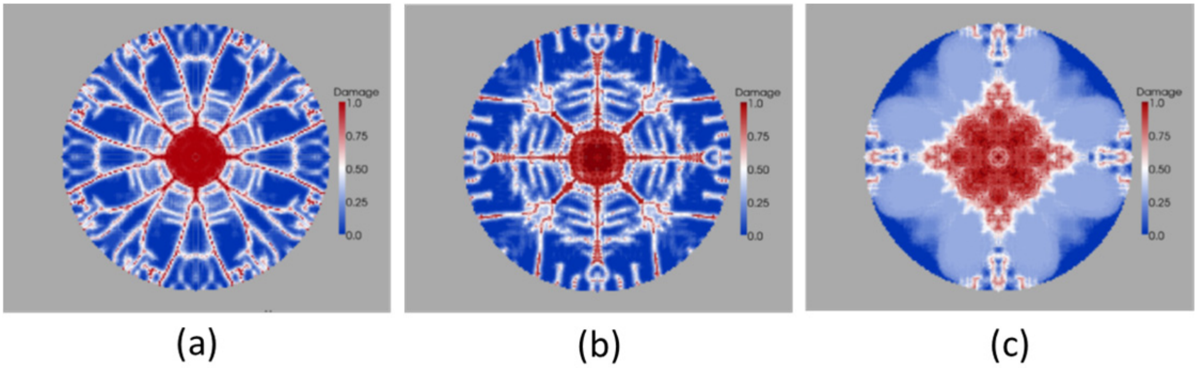

Figure 1.19. Impact of a hard sphere on a disc of brittle material at 5x10^{-5}s after impact. (a) p = 0. (b) p = 5. (c) p = 10 [23].

1.4.2. Relations between Classical Mechanics and Peridynamics

In classical mechanics, there are two basic concepts: stress and strain. The infinitesimal strain tensor is defined as the spatial derivative of displacement [39]:

$$\boldsymbol{\varepsilon} = \frac{1}{2}(\nabla \mathbf{u}^T + \nabla \mathbf{u}) \tag{1.20}$$

where $\nabla \mathbf{u}$ is the displacement gradient of the displacement field $\mathbf{u}$ with respect to the reference coordinates. The strain tensor at a point depends on the displacement at that point only, in other words it is a local quantity. One important physical interpretation of the strain tensor $\boldsymbol{\varepsilon}$ is the formula of unit elongation:

$$\frac{ds-dS}{dS} = \mathbf{n}.\boldsymbol{\varepsilon}\mathbf{n} \tag{1.21}$$

where dS and ds are the length of a small element vector before and after deformation. **n** is unit vector at the direction of the element before deformation.

Similar to the strain tensor, in classical mechanics stress is also a local quantity. In classical mechanics, the forces are contact forces, meaning the interactions happen over an infinitesimal distance between two touching surfaces. The force acting on a small surface area is proportional to that area by the formula:

$$\mathbf{df} = \mathrm{dA}\boldsymbol{\sigma}\mathbf{n} \tag{1.22}$$

where **df** is the force acting on the surface area dA at the point of interest, **n** is the surface normal vector (**n** is a unit vector). **σ** is the stress tensor. Though the force **df** depends on the direction of the surface normal, the stress tensor **σ** does not**,** at a point **σ** only depends on the state of deformation at that point.

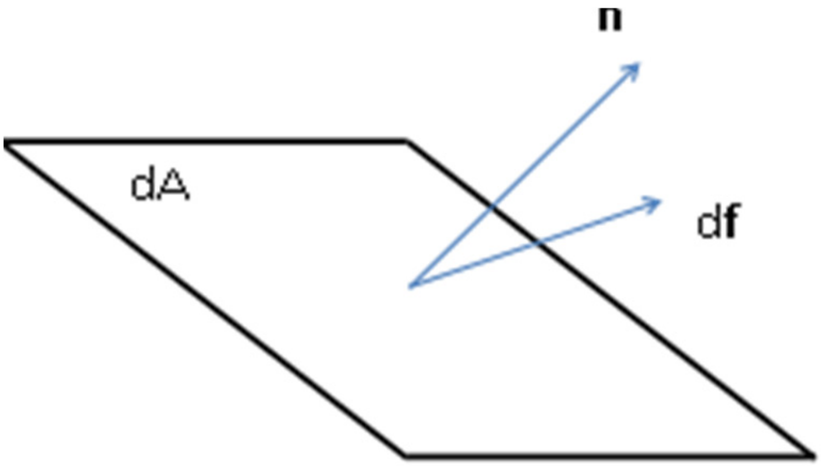

Figure 1.20. Force acting on a surface in classical mechanics.

When there is mechanical loading on a solid, the system will deform and reach equilibrium where there is a balance between external and internal forces. How the system deforms depends on the external load distribution, the system's intrinsic material properties, and its geometry. Constitutive equation in classical mechanics is the equation describing the relationship between the intrinsic stress and strain tensors, which depends only on the material's characteristics but not its macroscopic shape. Typically, in solids there are elastic and plastic deformations, which have different stress-strain relationships. The elastic region is where a material deforms reversibly under mechanical load, the material comes back to its original shape after the load is removed. There is a maximum limit of stress or strain under which the material will deform elastically, over that limit is the plastic region or fracture. Many materials, especially metals and alloys, display a linear relationship between stress and strain when it is in elastic region. In such relationship is described by Hooke's law [39]:

$$\boldsymbol{\sigma} = \mathbf{C}\boldsymbol{\varepsilon} \tag{1.23}$$

Or conversely:

$$\boldsymbol{\varepsilon} = \mathbf{S}\boldsymbol{\sigma} \tag{1.24}$$

where $\mathbf{C}$ is the stiffness tensor and $\mathbf{S}$ is the compliance tensor. Note that since stress and strain tensors are second order tensors, $\mathbf{C}$ and $\mathbf{S}$ are fourth order tensors. Not all materials show this linear behavior in elastic region. For example, rubber is a known material having non-linear elasticity. But the scope of this study is focused on linearly elastic solids only.

As shown above, in classical mechanics both stress and strain tensors in classical mechanics are local quantities, based on the concept of infinitesimal deformations and surface contact forces. But in peridynamics, interactions happen over finite distances. So how would one relate and compare the results in peridynamics and classical mechanics? And what would be an equivalent classical mechanic system to given a peridynamic system? It has been proven that in the limit where to horizon in peridynamics goes to zero, a peridynamic system will converge to classical mechanics [20, 40]. Specifically, from peridynamic deformations of all bonds connected to a peridynamic point one can calculate equivalent deformation gradient tensor at that point [34, 40]:

$$\mathbf{F} = \left(\int_H \underline{\omega}\langle\boldsymbol{\xi}\rangle\mathbf{Y}\langle\boldsymbol{\xi}\rangle\otimes\boldsymbol{\xi}\mathrm{dV}_{\boldsymbol{\xi}}\right).\left(\int_H \underline{\omega}\langle\boldsymbol{\xi}\rangle\boldsymbol{\xi}\otimes\boldsymbol{\xi}\mathrm{dV}_{\boldsymbol{\xi}}\right)^{-1} \tag{1.25}$$

The force interactions in peridynamics however are not contact forces, so the concept of contact surface stress in classical mechanics is not applicable. Thus the equivalent stress on a surface can be computed by summating all the interaction force between bonds that "go through" the area, as shown in the Figure 1.21 [41]. This definition of stress is actually considered to be closer to the original definition of stress in early elasticity theories.

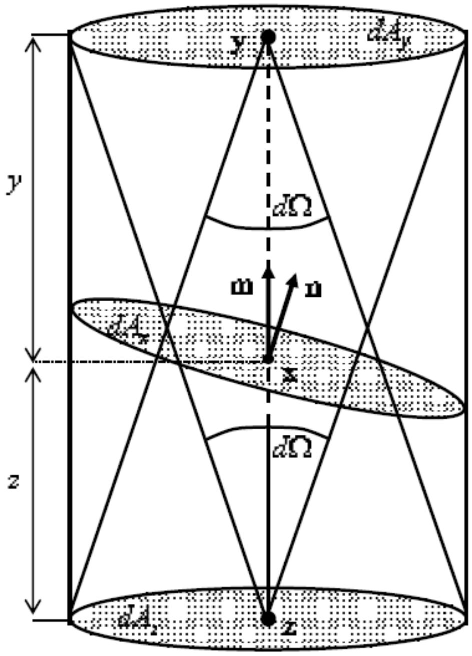

Figure 1.21. Interpretation of the force flux at x across a plane with unit normal n [41].

From this concept, the equivalent Piola stress tensor can be calculated from the force state $\underline{\mathbf{T}}$ via the collapsed stress tensor [20, 35, 40]:

$$\boldsymbol{\sigma} = \int_H \underline{\mathbf{T}}\langle\boldsymbol{\xi}\rangle \otimes \boldsymbol{\xi}\, dV_{\boldsymbol{\xi}} \tag{1.26}$$

The symbol ⊗ denotes the dyadic product between two vectors, which results in a tensor. This collapsed stress tensor has been proven to converge to classical dynamic stress when the horizon goes to zero [40]. Conversely, from deformation and stress in a classical system, an equivalent peridynamic system would have the bond deformation state **Y** and force vector state **T** of the forms [20, 34, 40]:

$$\mathbf{Y}\langle\boldsymbol{\xi}\rangle = \mathbf{F}\boldsymbol{\xi} \tag{1.27}$$

$$\mathbf{T}\langle\boldsymbol{\xi}\rangle = \underline{\omega}\langle\boldsymbol{\xi}\rangle\boldsymbol{\sigma}\left(\int_H \underline{\omega}\langle\boldsymbol{\xi}\rangle\boldsymbol{\xi}\otimes\boldsymbol{\xi}\mathrm{dV}_{\boldsymbol{\xi}}\right)^{-1}\boldsymbol{\xi} \tag{1.28}$$

1.4.3. Peridynamic Applications

Most of applications of peridynamic theory have been on simulations of cracking behaviors in various materials. The majority of these simulations have bond based model since the state based model is relatively new. The applications mostly focus on dynamic cracking behavior of different geometries, which is the strength of the peridynamic theory. Various types of materials and geometries have been studied. In the study by Doh Ha and Bobaru [42], a 3D bond based peridynamic model is used to study crack path instability and branching. Figure 1.22 shows the simulated crack paths in pre-notched samples with sudden mechanical loads. The simulated crack paths show much similarity to the ones obtained from real experiments, as shown in Figure 1.23. Other than sudden force, sudden change of speed at the surface has also been used to induce cracking in peridynamic simulations [43, 44]. In the studies, it is shown that the simulated cracks propagate in “almost identical” fashion as experimental observations.

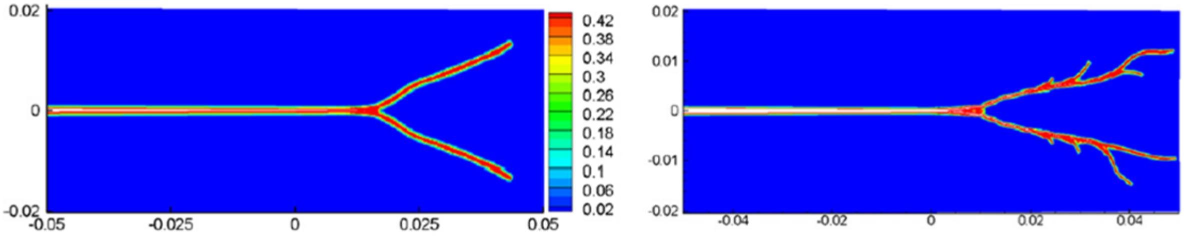

(a) (b)

Figure 1.22. Damaged maps for tests of crack path instability and branching, with sudden loads on top and bottom. (a) 12 MPa load, t = 46 µs. (b) 27 MPa load, t = 38 µs [42].

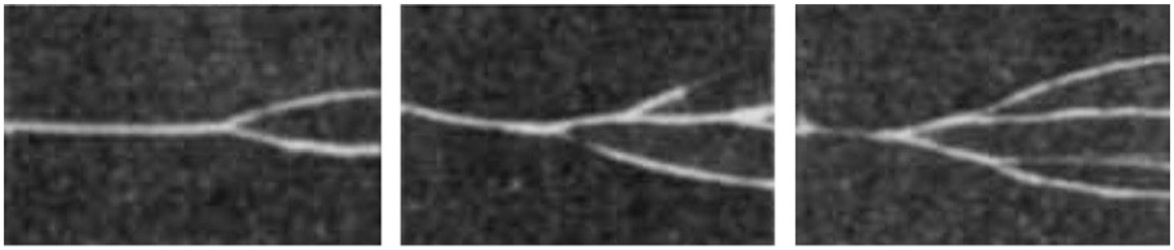

sharp pre-notch blunt pre-notch

Figure 1.23. Experimental results of cracking from sharp and blunt pre-notches [42, 45].

Thermal expansion can also be incorporated into peridynamic models simply by decomposing the total bond stretch into two parts: thermal expansion and mechanical deformation [24, 46]. Non-local heat transfer equation has also been incorporated to the peridynamic theory [47]. Figure 1.24(a) illustrates a real experiment where a single phase glass plate at high temperature is cooled by being pushed from an oven into the water. The crack is induced by internal stress, which is the result of uneven temperature distribution. Figure 1.24(b) shows the peridynamic simulation of crack branching pattern when the temperature difference between the oven and the water is 2500 K [46]. By varying the temperature difference, the researchers find as the difference increases, the crack pattern changes from straight to oscillating to branching cracks. This agrees well with experimental results.

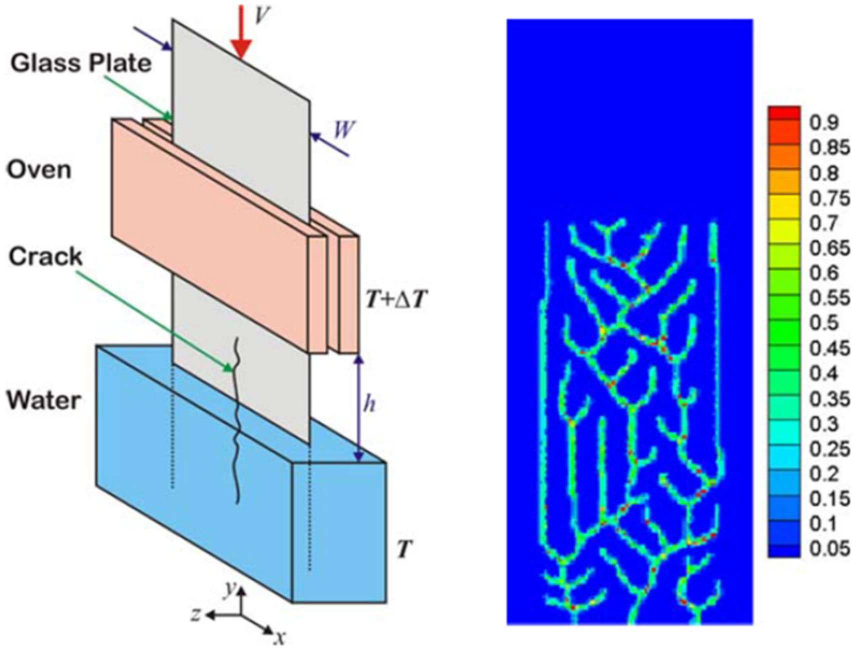

(a) (b)

Figure 1.24. (a) Crack growth in a glass plate under thermal cooling. (b) Peridynamic simulation result when ΔT = 2500 K [46].

Peridynamics has also been used for modelling 2D and 1D structures such as membranes and fibers. Currently only there are only bond based but not state based models for 2D and 1D peridynamic simulations. Figure 1.25(a) shows a 2D peridynamic simulation of a spherical membrane bursting when it is impacted by a sharp object [48]. It can be seen from the Figure that the cracks have irregular and uneven patterns, although the initial simulation conditions are symmetric. It is still not known if such simulation result reflects the instabilities also observed in real experiments, or if it is only due to numerical effects. Figure 1.25(b) shows a network of peridynamic fibers [48]. Both short range and long range, van der Waals forces are incorporated into the 1D peridynamic model. Initially, the fibers were straight, running in horizontal and vertical directions. But due to their force interactions, they deformed into an irregular pattern as shown in the Figure.

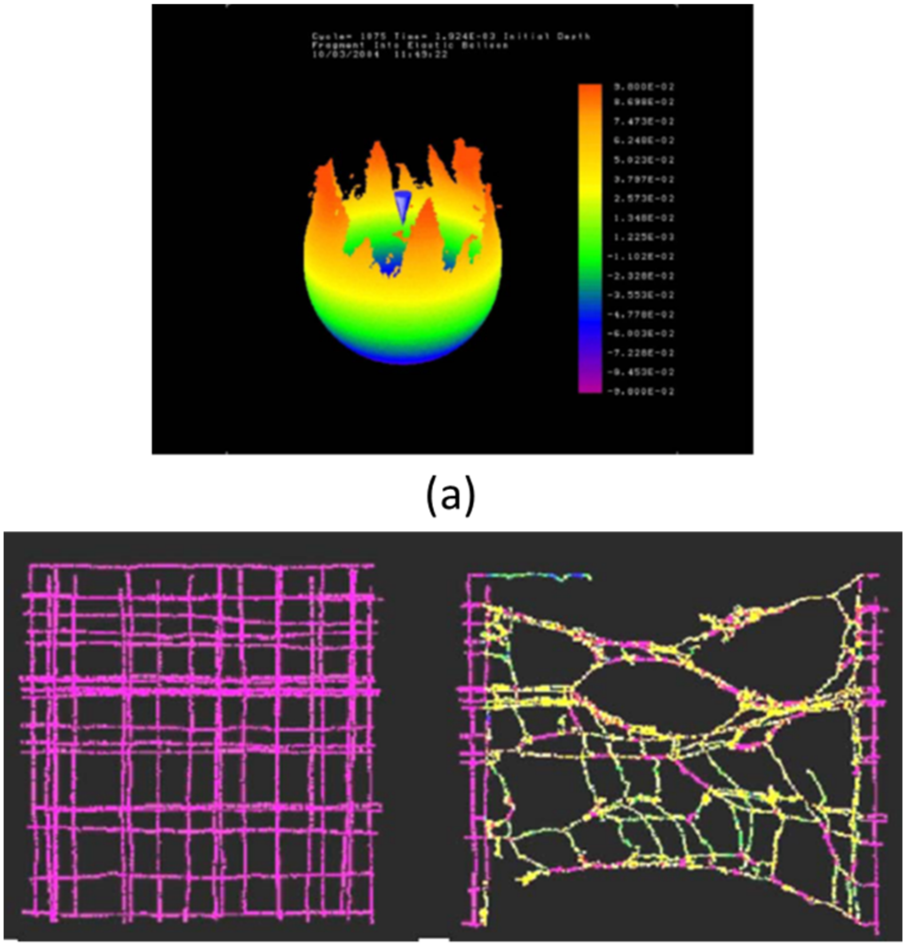

(a)

(b)

Figure 1.25. Peridynamic application in fracture of membrane (a); and a fiber network in initial and deformed configuration (b) [48].

Other than for modeling of single phase materials mentioned previously, the bond based peridynamic model has also been adapted to study mechanical behavior in composite materials [28, 49, 50]. Figure 1.26(a) shows the peridynamic discretization scheme for a material composed of a matrix phase and fibers. After the discretization, there are two types of nodes of peridynamic nodes corresponding to two phases in the system. Figure 1.26(b) shows the simulation result of damage pattern at an interface between two laminas in the study.

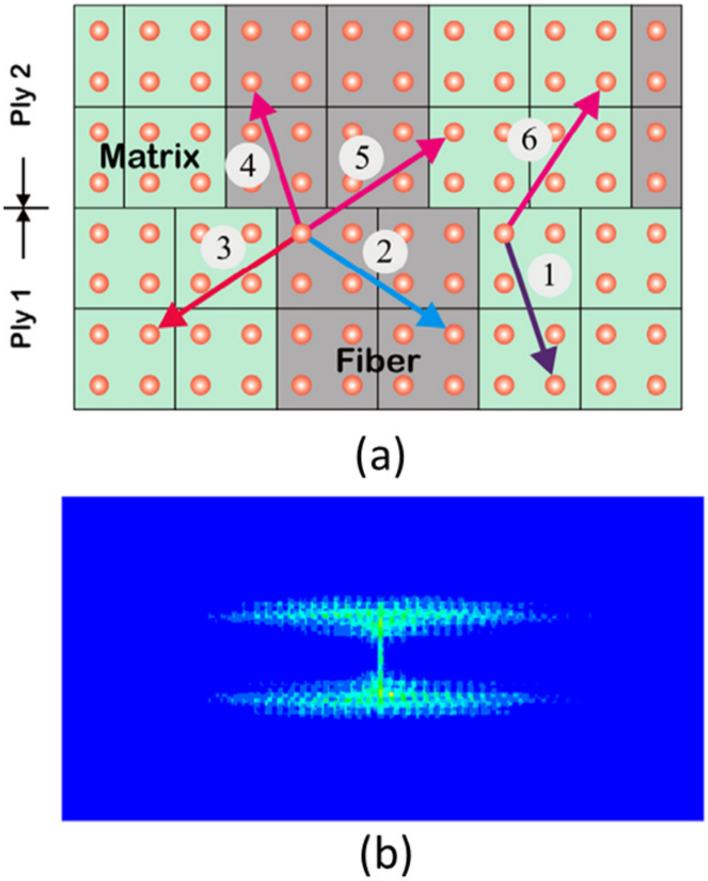

Figure 1.26. (a) Peridynamic discretization scheme of matrix and fibers in a laminate composite. (b) Local damage at interface between two lamina [28].

In contrast with classical mechanic modeling for composite materials, in peridynamic modeling there is no boundary condition at the interface between two phases. Instead, the two peridynamic nodes of different phases just have force interactions, depending on their relative displacement. The formula of force interaction between two nodes of different phase has important influence on the interface characteristics. For example, in a bond based peridynamic model, the interface rigidity can be increased by increasing the spring constant c, while the interface strength could be increased by either increasing the spring constant c or the critical stretch s_0, or both. It is important to note that the bond based model used on these researches can only have a same fixed Poisson's ratio for all phases. In reality materials have different Poisson's ratio, and especially inside a composite the difference in Poisson's ratio can have great influences on stress strain distribution. Thus a state based peridynamic model would be a better fit for composite materials.

Peridynamics shares one challenge similar to molecular dynamics, computation cost. For a typical simulation, each peridynamic subdomain/node has bonds with around a hundred other nodes. This can result in millions of bonds in a whole sample, while calculating interaction forces in just a bond requires several integrations. This results in a huge number of calculations, especially for samples with complex geometries. One way to resolve this issue is by coupling peridynamics with finite element analysis to take the advantages of both methods [22, 29, 51, 52]. Peridynamic model can be implemented within conventional finite element analysis software by using the truss elements [22]. Figure 1.27 shows such schematic for the coupling between peridynamic and finite element models. In the figure, there are two regions: the region on the left is modeled with finite element analysis while the region on the right is with peridynamics. Two regions must be bound to each other somehow to create a seamless system. To do so, an overlapping domain between the finite element and the peridynamics regions is created. In that domain, both peridynamic and finite element equations are used. This combination of two methods can utilize both peridynamics' ability for spontaneous crack growth prediction and finite element analysis' reduced computation cost. The coupling scheme has been used for modeling fracture in a rectangular bar under mechanical loading [29, 51].

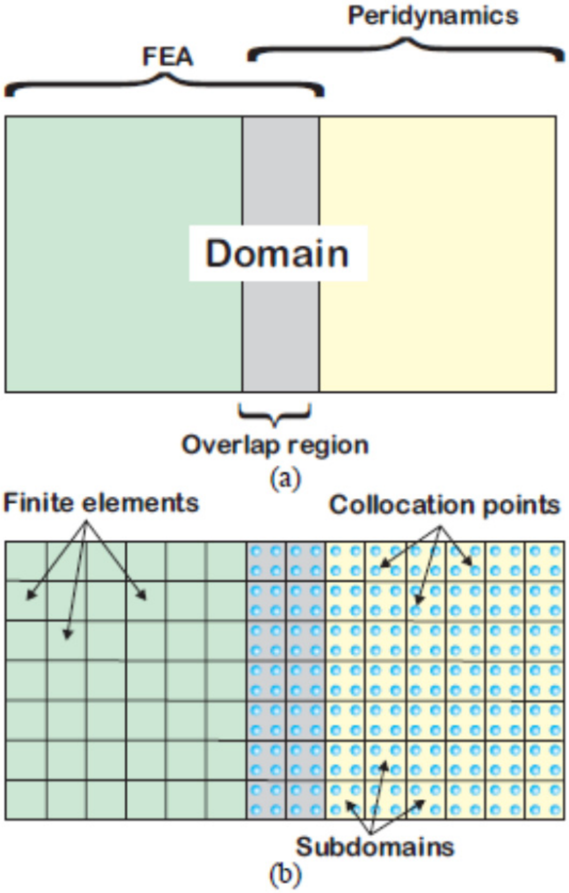

Figure 1.27. Schematic for coupling of finite element method and peridynamics [29].

Another way that has been used to achieve equilibrium state faster in peridynamics simulation is to use adaptive dynamic relaxation with a variable damping coefficient and modified material density [24, 27, 30]. In the method, an artificial damping coefficient value is chosen to make the system go to equilibrium point as fast as possible. Since an optimum value of damping coefficient is not always achievable, the study uses an adaptive algorithm to determine the value of the coefficient at each time step. This means the coefficient is not constant but can be changed during the simulation, thus it might result in unphysical effects in the simulated system.

2. 2D STATE BASED PERIDYNAMICS

2.1. Introduction

As mentioned in chapter 1, currently in peridynamics there are only bond based models for 2D structures. Since the bond based models can only have a fixed Poisson's ratio of 1/3, they are not adequate for modeling materials with different Poisson's ratios. Thus one goal of this study is to develop 2D models for linearly elastic solids in plane stress and plane strain conditions.

In 3D peridynamics, the neighborhood of each node is a sphere whose radius is the horizon δ. In the 2D peridynamics models developed here, only one layer of peridynamic nodes, lying on a flat x-y plane, exists. Thus the neighborhood region is a disk. For a 2D model to correspond to a classical continuum mechanics model, the formulas from 3D peridynamics must be modified accordingly.

The key to ensuring that a peridynamics model corresponds to a classical continuum mechanics model is that under the same strain/displacement condition, both models must have the same energy density. Thus, the peridynamic system behaves the same as the classical system under the same loading conditions. To develop a force vector state of a peridynamics model in 2D, four steps are followed:

- Find the classical strain energy density as a function of strain and elastic constants (k, υ) in 2D.
- Propose a formula of 2D state-based peridynamic energy density as a function of displacements.
- Equalize the two energies to find the relationship between the peridynamics and classical

constants.

- Derive the peridynamic force vector state by taking the Frechet derivative of the peridynamic energy density.

2.2. Peridynamic Model for 2D Plane Stress

Classical strain energy density in plane stress

In continuum mechanics, the linearly elastic strain energy density function is decomposed into two parts, the volumetric energy density and the distortional energy density [34]:

$$\Omega = \frac{k}{2}\left(\frac{\mathrm{d}V}{V}\right)^2 + \mu\varepsilon_{\mathrm{ij}}^{\mathrm{d}}\varepsilon_{\mathrm{ij}}^{\mathrm{d}} \tag{2.1}$$

where k and μ are the bulk and shear moduli, respectively, $\mathrm{d}V/V$ is the volume dilatation, and $\varepsilon_{\mathrm{ij}}^{\mathrm{d}}$ is the ij component of the deviatoric strain tensor. In the second term, the Einstein summation notation is used, meaning a summation is made over all ij components of the deviatoric strain tensor.

To find the energy density function in plane stress, the stress/strain components in the z directions are not independent. Thus the energy density can be written as a function of strains in the x-y plane only. In plane stress, all stress components on the surface normal to the third direction are equal to zero. The ε_{33} component of the strain tensor, however, is non-zero [53]:

$$\boldsymbol{\sigma} = \begin{bmatrix} \sigma_{11} & \sigma_{12} & 0 \\ \sigma_{21} & \sigma_{22} & 0 \\ 0 & 0 & 0 \end{bmatrix} \qquad \boldsymbol{\varepsilon} = \begin{bmatrix} \varepsilon_{11} & \varepsilon_{12} & 0 \\ \varepsilon_{21} & \varepsilon_{22} & 0 \\ 0 & 0 & \varepsilon_{33} \end{bmatrix} \tag{2.2}$$

The ε_{33} component is not independent of other components. Using Hooke's law for an isotropic material, its dependence on ε_{11} and ε_{22} is determined:

$$\varepsilon_{11} = \frac{1}{E}(\sigma_{11} - \nu\sigma_{22} - \nu\sigma_{33}) = \frac{1}{E}(\sigma_{11} - \nu\sigma_{22}) \tag{2.3}$$

$$\varepsilon_{22} = \frac{1}{E}(\sigma_{22} - \nu\sigma_{11} - \nu\sigma_{33}) = \frac{1}{E}(\sigma_{22} - \nu\sigma_{11}) \tag{2.4}$$

$$\varepsilon_{33} = \frac{1}{E}(\sigma_{33} - \nu\sigma_{11} - \nu\sigma_{22}) = \frac{-\nu}{E}(\sigma_{11}+\sigma_{22}) \tag{2.5}$$

where E is the Young modulus and υ is Poisson's ratio.

$$\frac{(2.5)}{(2.3)+(2.4)} \rightarrow \ \varepsilon_{33} = \frac{\nu}{\nu-1}(\varepsilon_{11}+\varepsilon_{22}) \tag{2.6}$$

The volume dilatation is also a function of strain in the x-y plane:

$$\frac{\mathrm{d}V}{V} = (\varepsilon_{11}+\varepsilon_{22}+\varepsilon_{33}) = \frac{2\nu-1}{\nu-1}(\varepsilon_{11}+\varepsilon_{22}) \tag{2.7}$$

Taking $\frac{(2.6)}{(2.7)}$, ε_{33} as a function of the volume dilatation becomes:

$$\varepsilon_{33} = \frac{\nu}{2\nu-1}\frac{\mathrm{d}V}{V} \tag{2.8}$$

Also, from (2.7) the deviatoric strain tensor is:

$$\boldsymbol{\varepsilon}^{\mathrm{d}} = \boldsymbol{\varepsilon} - \frac{1}{3}\frac{\mathrm{d}V}{V}\mathbf{I} = \begin{bmatrix} \varepsilon_{11}^{\mathrm{d}} & \varepsilon_{12}^{\mathrm{d}} & 0 \\ \varepsilon_{21}^{\mathrm{d}} & \varepsilon_{22}^{\mathrm{d}} & 0 \\ 0 & 0 & \varepsilon_{33}^{\mathrm{d}} \end{bmatrix} \tag{2.9}$$

where **I** is the identity tensor. The component $\varepsilon_{33}^{\mathrm{d}}$ is given by:

$$\varepsilon_{33}^{\mathrm{d}} = \varepsilon_{33} - \frac{1}{3}\frac{\mathrm{d}V}{V} = \frac{\nu+1}{3(2\nu-1)}\frac{\mathrm{d}V}{V} \tag{2.10}$$

Substituting (11) into (2), the classical strain energy density in plane stress is:

$$\Omega = \left[\frac{k}{2} + \mu\left(\frac{(\nu+1)}{3(2\nu-1)}\right)^2\right]\left(\frac{\mathrm{d}V}{V}\right)^2 + \mu\sum\nolimits_{\mathrm{i,j}=1,2} \varepsilon_{\mathrm{ij}}^{\mathrm{d}}\,\varepsilon_{\mathrm{ij}}^{\mathrm{d}} \tag{2.11}$$

From (2.7) and (2.11), Ω is only a function of strain components in the x-y plane. Note that in the second term of the right hand side, i and j range from 1 to 2.

Peridynamic strain energy density formula

Now that the energy density in classical mechanics has been established, the peridynamic energy density in 2D to match (2.11) is needed. Similar to the 3D case, first the scalar-valued function θ, is defined. Later it will be proven to be equal to the volume dilatation.

$$\theta = \frac{2(2\nu-1)}{(\nu-1)}\frac{\underline{\omega}\underline{x}\bullet\underline{e}}{q} \tag{2.12}$$

In this model, $\underline{\omega}$ also depends only on the bond length $|\xi|$ but not its direction, $\underline{\omega} = \underline{\omega}_S\langle|\xi|\rangle$. Similar to the 3D case, to see that θ is equal to the volume dilatation, consider the transversely isotropic plane stress condition, $\varepsilon_{11} = \varepsilon_{22} = \varepsilon_0$, in which the peridynamic 2D deformation takes the form $Y = (1+\varepsilon_0)X$. Taking the integration in (2.12), and comparing to (2.7), both result in the same value of $\frac{2(2\nu-1)}{(\nu-1)}\varepsilon_0$.

Now suppose that the peridynamic energy density at a point takes the form:

$$W\left(\theta, \underline{e}^{\mathrm{d}}\right) = \frac{k'\theta^2}{2} + \frac{\alpha}{2}\left(\underline{\omega}\underline{e}^{\mathrm{d}}\right)\bullet\underline{e}^{\mathrm{d}} \tag{2.13}$$

where k' and α are parameters to be found. θ is the volume dilatation in (2.12). Here $\underline{e}^{\mathrm{d}}$ is the deviatoric part of the extension state $\underline{e}$ and still keeps the same form as in 3D case: $\underline{e}^{\mathrm{d}} = \underline{e} - \frac{\theta\underline{x}}{3}$. It is important to note that to calculate W at a point of interest correctly, one must use the value of θ at that point only, not at other points within the neighborhood region of that point since θ varies.

Relationship between the peridynamics and classical constants

First relate the peridynamic extension (elongation) $\underline{e}\langle\boldsymbol{\xi}\rangle$ and the classical strain tensor $\boldsymbol{\varepsilon}$. Since the bond vector ξ can be viewed as a small material element in continuum mechanics, the bond extension $\underline{e}\langle\boldsymbol{\xi}\rangle$ (change in bond length) is the element's elongation [39]:

$$\underline{e}\langle\boldsymbol{\xi}\rangle = |\boldsymbol{\xi}|\,\mathbf{n}\cdot\boldsymbol{\varepsilon}\mathbf{n} = \frac{1}{|\boldsymbol{\xi}|}\boldsymbol{\xi}\cdot\boldsymbol{\varepsilon}\boldsymbol{\xi} = \frac{1}{|\boldsymbol{\xi}|}\varepsilon_{\mathrm{ij}}\xi_{\mathrm{i}}\xi_{\mathrm{j}} \tag{2.14}$$

where **n** is the unit vector in the bond vector's direction, $\mathbf{n} = \boldsymbol{\xi}/|\boldsymbol{\xi}|$. Similar to [34], the deviatoric part of the extension state is given by:

$$\underline{e}^{\mathrm{d}}\langle\boldsymbol{\xi}\rangle = \frac{1}{|\boldsymbol{\xi}|}\varepsilon^{\mathrm{d}}_{\mathrm{ij}}\xi_{\mathrm{i}}\xi_{\mathrm{j}} = \frac{1}{|\boldsymbol{\xi}|}\sum_{\mathrm{i,j}=1,2}\varepsilon^{\mathrm{d}}_{\mathrm{ij}}\,\xi_{\mathrm{i}}\xi_{\mathrm{j}} \tag{2.15}$$

The main difference from the 3D model is that in the 2D model the indices i and j only run from 1 to 2, not to 3. Since all peridynamic nodes lie on a same x-y plane, the third component (ξ_3) is always zero.

Using (2.15) to calculate the second term of (2.13), noting that $\varepsilon^{\mathrm{d}}_{\mathrm{ij}} = \varepsilon^{\mathrm{d}}_{\mathrm{ji}}$:

$$\frac{\alpha}{2}\left(\underline{\omega}\underline{e}^{\mathrm{d}}\right)\bullet\underline{e}^{\mathrm{d}} = \frac{\alpha}{2}\int_{\mathrm{H}}\underline{\omega}\,\langle\boldsymbol{\xi}\rangle\left[\frac{1}{|\boldsymbol{\xi}|}\sum_{\mathrm{i,j}=1,2}\varepsilon^{\mathrm{d}}_{\mathrm{ij}}\,\xi_{\mathrm{i}}\xi_{\mathrm{j}}\right]\left[\frac{1}{|\boldsymbol{\xi}|}\sum_{\mathrm{k,l}=1,2}\varepsilon^{\mathrm{d}}_{\mathrm{kl}}\,\xi_{\mathrm{k}}\xi_{\mathrm{l}}\right]\mathrm{d}V_{\boldsymbol{\xi}} =$$

$$\frac{\alpha}{2}\int_{\mathrm{H}}\frac{\underline{\omega}\langle\boldsymbol{\xi}\rangle}{|\boldsymbol{\xi}|^2}\left[(\varepsilon^{\mathrm{d}}_{11})^2(\xi_1)^4 + (\varepsilon^{\mathrm{d}}_{22})^2(\xi_2)^4 + 4(\varepsilon^{\mathrm{d}}_{12})^2(\xi_1)^2(\xi_2)^2 + 2\varepsilon^{\mathrm{d}}_{11}\varepsilon^{\mathrm{d}}_{22}(\xi_1)^2(\xi_2)^2 +\right.$$

$$\left.4\varepsilon^{\mathrm{d}}_{11}\varepsilon^{\mathrm{d}}_{12}(\xi_1)^3\xi_2 + 4\varepsilon^{\mathrm{d}}_{22}\varepsilon^{\mathrm{d}}_{12}\xi_1(\xi_2)^3\right]\mathrm{d}V_{\boldsymbol{\xi}} \tag{2.16}$$

Since it is assumed that the influence function $\underline{\omega}$ depends on the bond length $|\boldsymbol{\xi}|$ only, but not its direction, terms that have an odd number of any index integrate to zero due to the symmetry of the integration region (a disk). Thus only the integration of terms that contain $(\xi_1)^4$, $(\xi_2)^{4,}$ and $(\xi_1)^2(\xi_2)^2$ are calculated. Due to the symmetry of the 2D integration region, integrations of $(\xi_1)^4$ and $(\xi_2)^4$ are equal. Thus, to evaluate equation (2.16), only two integrations are required.

Using polar coordinates, $\xi_1 = r\cos\Phi$, $\xi_2 = r\sin\Phi$, and $\mathrm{d}V_{\xi} = l_z r\,\mathrm{d}r\,\mathrm{d}\Phi$, where l_z is the thickness of the system or the peridynamic nodes in the z direction. Since this is a 2D simulation, l_z can be set as any value or can be of unit length. l_z is displayed explicitly to keep the units of quantities including volume, energy density, etc., consistent with ones in the classical model or 3D peridynamic model. Thus,

$$\int_{\mathrm{H}} \frac{\underline{\omega}\langle\boldsymbol{\xi}\rangle}{|\boldsymbol{\xi}|^2} \xi_1^4 \mathrm{d}V_{\boldsymbol{\xi}} = \int_0^{\delta} \int_0^{2\pi} \frac{\underline{\omega}_{\mathrm{s}}\langle r\rangle}{r^2} r^4 \cos^4\Phi l_z r \mathrm{d}r \mathrm{d}\Phi = l_z \int_0^{\delta} \underline{\omega}_s\langle r\rangle r^3 \mathrm{d}r \int_0^{2\pi} \cos^4\Phi \mathrm{d}\Phi = \frac{q}{2\pi}\frac{3\pi}{4} = \frac{3q}{8} \tag{2.17}$$

and

$$\int_{\mathrm{H}} \frac{\underline{\omega}\langle\boldsymbol{\xi}\rangle}{|\boldsymbol{\xi}|^2} \xi_1^2 \xi_2^2 \mathrm{d}V_{\boldsymbol{\xi}} = \int_0^{\delta} \int_0^{2\pi} \frac{\underline{\omega}_{\mathrm{s}}\langle r\rangle}{r^2} r^4 \cos^2\Phi \sin^2\Phi l_z r \mathrm{d}r \mathrm{d}\Phi =$$

$$l_z \int_0^{\delta} \underline{\omega}_s\langle r\rangle r^3 \mathrm{d}r \int_0^{2\pi} \cos^2\Phi \sin^2\Phi \mathrm{d}\Phi = \frac{q}{2\pi}\frac{\pi}{4} = \frac{q}{8} \tag{2.18}$$

where in this 2D model it is assumed that the influence function $\underline{\omega}$ depends on the bond length only, $\underline{\omega} = \underline{\omega}_{\mathrm{s}}\langle|\boldsymbol{\xi}|\rangle = \underline{\omega}_{\mathrm{s}}\langle r\rangle$.

To prove that the integration $l_z \int_0^{\delta} \underline{\omega}_s\langle r\rangle r^3 \mathrm{d}r = \frac{q}{2\pi}$, by using polar coordinates one finds that q is given by:

$$q = \underline{\omega}\underline{x}\bullet\underline{x} = \int_{\mathrm{H}} \underline{\omega}_{\mathrm{s}}\langle r\rangle r^2 \mathrm{d}V_{\boldsymbol{\xi}} = 2\pi l_z \int_0^{\delta} \underline{\omega}_{\mathrm{s}} \langle r\rangle r^3 \mathrm{d}r \tag{2.19}$$

Substituting results from (2.17) and (2.18) to (2.16):

$$\frac{\alpha}{2}\left(\underline{\omega}\underline{e}^{\mathrm{d}}\right)\bullet\underline{e}^{\mathrm{d}} = \frac{\alpha}{2}\left[\frac{2q}{8}\sum_{\mathrm{i,j=1,2}} \varepsilon_{\mathrm{ij}}^{\mathrm{d}} \varepsilon_{\mathrm{ij}}^{\mathrm{d}} + \frac{q}{8}\left(\sum_{\mathrm{i=1,2}} \varepsilon_{\mathrm{ii}}^{\mathrm{d}}\right)^2\right] \tag{2.20}$$

By utilizing the property $\varepsilon_{11}^{\mathrm{d}} + \varepsilon_{22}^{\mathrm{d}} + \varepsilon_{33}^{\mathrm{d}} = 0$, the second summation on the right hand side of (2.20) is equal to $-\varepsilon_{33}^{\mathrm{d}}$. Then:

$$\frac{\alpha}{2}\left(\underline{\omega}\underline{e}^{\mathrm{d}}\right)\bullet\underline{e}^{\mathrm{d}} = \frac{\alpha q}{16}\left(\varepsilon_{33}^{\mathrm{d}}\right)^2 + \frac{\alpha q}{8}\sum_{\mathrm{i,j=1,2}} \varepsilon_{\mathrm{ij}}^{\mathrm{d}} \varepsilon_{\mathrm{ij}}^{\mathrm{d}} \tag{2.21}$$

Substituting (2.21) into (2.13) and θ by dV/V, one obtains:

$$W\left(\theta, \underline{e}^{\mathrm{d}}\right) = \frac{k'}{2}\left(\frac{\mathrm{d}V}{V}\right)^2 + \frac{\alpha q}{16}\left(\varepsilon_{33}^{\mathrm{d}}\right)^2 + \frac{\alpha q}{8}\sum_{\mathrm{i,j=1,2}} \varepsilon_{\mathrm{ij}}^{\mathrm{d}} \varepsilon_{\mathrm{ij}}^{\mathrm{d}} \tag{2.22}$$

In plane stress, substitute $\varepsilon_{33}^{\mathrm{d}}$ in (2.10) to (2.22), obtaining:

$$W\left(\theta,\underline{e}^{\mathrm{d}}\right)=\left(\frac{k'}{2}+\frac{\alpha q}{144}\frac{(\nu+1)^2}{(2\nu-1)^2}\right)\left(\frac{\mathrm{d}V}{V}\right)^2+\frac{\alpha q}{8}\sum\nolimits_{\mathrm{i,j=1,2}}\varepsilon_{\mathrm{ij}}^{\mathrm{d}}\,\varepsilon_{\mathrm{ij}}^{\mathrm{d}} \tag{2.23}$$

Equalizing (2.23) and (2.11), the relationships between classical and peridynamic parameters in plane stress are obtained:

$$\frac{\alpha q}{8}=\mu \qquad \text{or} \quad \alpha=\frac{8\mu}{q} \tag{2.24}$$

$$\frac{k'}{2}+\frac{\alpha q}{144}\frac{(\nu+1)^2}{(2\nu-1)^2}=\frac{k}{2}+\frac{\mu}{9}\frac{(\nu+1)^2}{(2\nu-1)^2} \quad \text{or} \quad k'=k+\frac{\mu}{9}\frac{(\nu+1)^2}{(2\nu-1)^2} \tag{2.25}$$

The peridynamic force state

Similar to the 3D model in [34], the model developed here is also an ordinary model: $\underline{\mathbf{T}}$ = $\underline{t}\mathbf{M}$, where **M** is the unit vector along the deformed bond direction ([34], equation (43)). Thus the force vector state is parallel to the bond vector. Here $\underline{t}$ is the magnitude of $\underline{\mathbf{T}}$ and is called "scalar force state". $\underline{t}$ is calculated from the Frechet derivative of the energy density function *W* with respect to the extension state $\underline{e}$. From (2.13):

$$\Delta W=k'\theta\left(\nabla_{\underline{e}}\theta\right)\bullet\Delta\underline{e}+\alpha\left(\underline{\omega e}^{\mathrm{d}}\right)\bullet\Delta\underline{e}^{\mathrm{d}} \tag{2.26}$$

where $\nabla_{\underline{e}}\theta$ is the Frechet derivate of θ with respect to $\underline{e}$; this quantity will be calculated later.

To calculate $\Delta\underline{e}^{\mathrm{d}}$ from the definition in [34]:

$$\underline{e}^{\mathrm{d}}=e-\frac{\theta\underline{x}}{3}\rightarrow\ \Delta\underline{e}^{\mathrm{d}}=\Delta\underline{e}-\frac{\underline{x}}{3}\left(\nabla_{\underline{e}}\theta\right)\bullet\Delta\underline{e} \tag{2.27}$$

Substitute (2.27) to (2.26) and after some rearrangements one obtains:

$$\Delta W=\left[\left(k'\theta-\frac{\alpha}{3}\left(\underline{\omega e}^{\mathrm{d}}\right)\bullet\underline{x}\right)\nabla_{\underline{e}}\theta+\alpha\underline{\omega e}^{\mathrm{d}}\right]\bullet\Delta e=\underline{t}\bullet\Delta e \tag{2.28}$$

This gives $\underline{t}=\left(k'\theta-\frac{\alpha}{3}\left(\underline{\omega e}^{\mathrm{d}}\right)\bullet\underline{x}\right)\nabla_{\underline{e}}\theta+\alpha\underline{\omega e}^{\mathrm{d}}$ (2.29)

To calculate $\nabla_{\underline{e}}\theta$ in plane stress, use the definition of θ in (2.12):

$$\nabla_{\underline{e}}\theta = \frac{2(2\nu-1)}{(\nu-1)}\frac{\underline{\underline{\omega x}}}{q} \tag{2.30}$$

Thus in the 2D plane stress model, the force state $\underline{t}$ takes the form:

$$\underline{t} = \frac{2(2\nu-1)}{(\nu-1)}\left(k'\theta - \frac{\alpha}{3}\left(\underline{\omega e}^{\mathrm{d}}\right)\bullet\underline{x}\right)\frac{\underline{\underline{\omega x}}}{q} + \alpha\underline{\omega e}^{\mathrm{d}} \tag{2.31}$$

where θ, α, and k' are given in (2.12), (2.24) and (2.25). Unlike in the 3D case, the formula for the force state $\underline{t}$ in this 2D case has more terms. Also, $\underline{t}$ is not decomposed into co-isotropic co-deviatoric parts as in the 3D model.

2.3. Peridynamic Model for 2D Plane Strain

Classical strain energy density in plane strain

As opposed to plane stress, in plane strain ε_{33} is zero, but the stress component is not zero [53]:

$$\boldsymbol{\sigma} = \begin{bmatrix} \sigma_{11} & \sigma_{12} & 0 \\ \sigma_{21} & \sigma_{22} & 0 \\ 0 & 0 & \sigma_{33} \end{bmatrix} \quad \boldsymbol{\varepsilon} = \begin{bmatrix} \varepsilon_{11} & \varepsilon_{12} & 0 \\ \varepsilon_{21} & \varepsilon_{22} & 0 \\ 0 & 0 & 0 \end{bmatrix} \tag{2.32}$$

Because ε_{33} is now zero, even with the same strains in the x-y plane, volume dilatation in the plane strain condition is different from that in the plane stress condition (2.7) by a factor:

$$\frac{\mathrm{d}V}{V} = (\varepsilon_{11}+\varepsilon_{22}+\varepsilon_{33}) = (\varepsilon_{11}+\varepsilon_{22}) \tag{2.33}$$

Compared to (2.7), volume dilatation in (2.33) does not have the factor $\frac{2\nu-1}{\nu-1}$.

Similarly, the component $\varepsilon_{33}^{\mathrm{d}}$ is given by:

$$\varepsilon_{33}^{\mathrm{d}} = \varepsilon_{33} - \frac{1}{3}\frac{\mathrm{d}V}{V} = -\frac{1}{3}\frac{\mathrm{d}V}{V} \tag{2.34}$$

Substituting (2.34) into (2.1), the classical strain energy density in plane strain is obtained:

$$\Omega = \left[\frac{k}{2} + \frac{\mu}{9}\right]\left(\frac{\mathrm{d}V}{V}\right)^2 + \mu \textstyle\sum_{\mathrm{i,j=1,2}} \varepsilon_{\mathrm{ij}}^{\mathrm{d}}\, \varepsilon_{\mathrm{ij}}^{\mathrm{d}} \tag{2.35}$$

Peridynamic strain energy density

In plane strain the volume dilatation differs from that of plane stress, so the peridynamic function θ now is given by:

$$\theta = 2\frac{\underline{\omega x}\bullet\underline{e}}{q} \tag{2.36}$$

Again assume that the form of 2D peridynamic energy density remains as in (2.13). Matching (2.13) and (2.35), the values of k' and α for plane strain are obtained.

Relationship between the peridynamics and classical constants

Since the 2D peridynamic energy is still of the same form as in (2.13) with θ, k', and α taking new values, the relationships are the same as in (2.22):

$$W\left(\theta, \underline{e}^{\mathrm{d}}\right) = \frac{k'}{2}\left(\frac{\mathrm{d}V}{V}\right)^2 + \frac{\alpha q}{16}\left(\varepsilon_{33}^{\mathrm{d}}\right)^2 + \frac{\alpha q}{8}\textstyle\sum_{\mathrm{i,j=1,2}} \varepsilon_{\mathrm{ij}}^{\mathrm{d}}\, \varepsilon_{\mathrm{ij}}^{\mathrm{d}} \tag{2.37}$$

In plane strain, the relationship between $\varepsilon_{33}^{\mathrm{d}}$ and dV/V is in (2.34). Substituting (2.34) into (2.37):

$$W\left(\theta, \underline{e}^{\mathrm{d}}\right) = \left(\frac{k'}{2} + \frac{\alpha q}{144}\right)\left(\frac{\mathrm{d}V}{V}\right)^2 + \frac{\alpha q}{8}\textstyle\sum_{\mathrm{i,j=1,2}} \varepsilon_{\mathrm{ij}}^{\mathrm{d}}\, \varepsilon_{\mathrm{ij}}^{\mathrm{d}} \tag{2.38}$$

Comparing (2.38) and (2.35):

$$\frac{\alpha q}{8} = \mu \qquad \text{or} \quad \alpha = \frac{8\mu}{q} \tag{2.39}$$

$$\frac{k'}{2} + \frac{\alpha q}{144} = \frac{k}{2} + \frac{\mu}{9} \quad \text{or} \quad k' = k + \frac{\mu}{9} \tag{2.40}$$

The peridynamic force state

As the 2D peridynamic energy density still takes the same form, (2.29) still applies for $\underline{t}$ but just with new values of θ, α, and k' given in (2.36), (2.39) and (2.40). To calculate $\nabla_{\underline{e}}\theta$ for plane strain, use the definition of θ in (2.36), so in 2D plane strain:

$$\nabla_{\underline{e}}\theta = 2\frac{\underline{\omega x}}{q} \tag{2.41}$$

The force state $\underline{t}$ becomes:

$$\underline{t} = 2\left(k'\theta - \frac{\alpha}{3}\left(\underline{\omega e}^{\mathrm{d}}\right)\bullet\underline{x}\right)\frac{\underline{\omega x}}{q} + \alpha\underline{\omega e}^{\mathrm{d}} \tag{2.42}$$

2.4. Simulation Approach

2.4.1. Finding the Peridynamic Steady-State Solution

To obtain steady state in the 2D peridynamics simulation, two different approaches are applied: dynamic relaxation and energy minimization. The purpose of using both these methods is to prove that the 2D peridynamic model is stable and results can be achieved with either of them. With dynamic relaxation, a viscous force is added to dissipate the kinetic energy of the system such that, after a sufficiently long time, the system approaches the steady state. In the 2D model, viscous forces between a pair of peridynamic nodes are parallel to the bond vector. Their values are given by:

$$\mathbf{F}_{12} = -\mathbf{F}_{21} = \gamma\frac{\mathbf{v}_2^{\mathrm{para}} - \mathbf{v}_1^{\mathrm{para}}}{|\boldsymbol{\xi}|}\mathrm{d}V_1\mathrm{d}V_2 \tag{2.43}$$

Figure 2.1 shows a schematic of the velocities of two bonded peridynamic nodes. Only the relative velocity between them results in a friction force. More specifically, only the parallel component of the velocity is used to ensure that there is no damping force when the system undergoes a rigid body rotation or translation. This allows the model to mimic the dynamic behavior of a real-life system more closely because it is analogous to the dynamic viscosity of solids in classical mechanics. But if only the steady state results are of interest, as shown previously, adaptive dynamic relaxation can be used [24, 28, 30] with the advantage of less computation. It may, however, result in unphysical effects due to a variable viscosity coefficient.

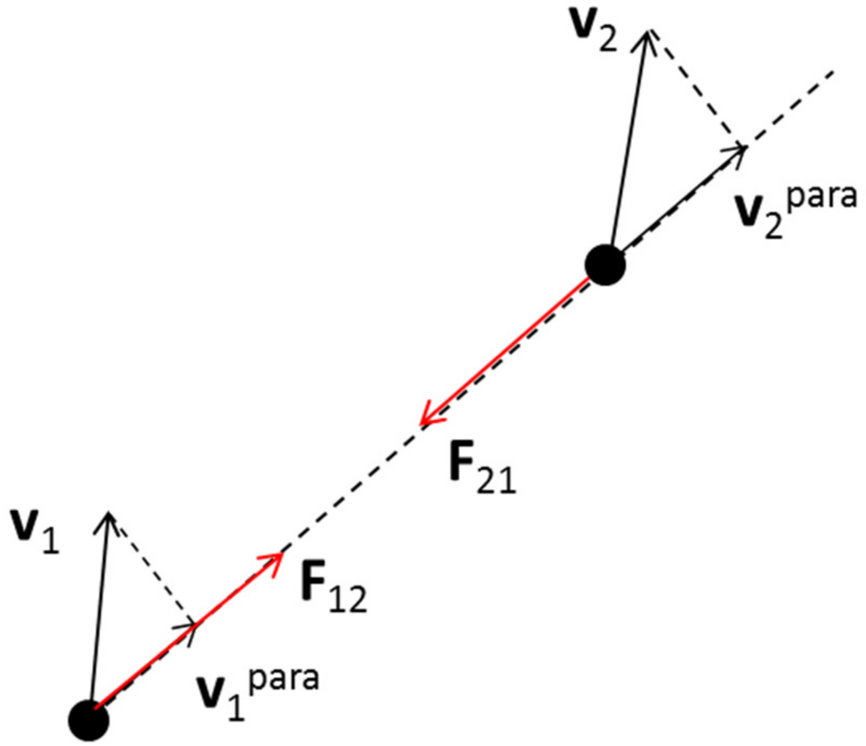

Figure 2.1. Viscous interaction forces between two peridynamic nodes.

To implement the dynamic relaxation simulation, velocity-Verlet algorithm is used in the simulation code to calculate trajectories and velocities of peridynamic nodes:

$$\mathbf{y}_{n+1} = \mathbf{y}_n + \mathbf{v}_n \Delta t + \frac{1}{2}\mathbf{a}_n (\Delta t)^2 \tag{2.44}$$

$$\mathbf{v}_{n+1} = \mathbf{v}_n + \frac{1}{2}(\mathbf{a}_n + \mathbf{a}_{n+1})\Delta t \tag{2.45}$$

where $\mathbf{y}_n$, $\mathbf{v}_n$, and $\mathbf{a}_n$ are position, velocity, and acceleration of the peridynamic node at the simulation step *n*. Similarly, $\mathbf{y}_{n+1}$, $\mathbf{v}_{n+1}$, and $\mathbf{a}_{n+1}$ are position, velocity, and acceleration of the peridynamic node at the simulation step *n+1*. The acceleration $\mathbf{a}_n$ is known since it is proportional to the total force acting on the node, which a function of coordinates at step *n*. After $\mathbf{y}_{n+1}$ is calculated in (2.44), $\mathbf{a}_{n+1}$, which depends on $\mathbf{y}_{n+1}$, is also known. Thus $\mathbf{v}_{n+1}$ in (2.45) is also known.

Similar to adaptive dynamic relaxation, energy minimization methods can be used when only the steady-state condition is of interest. The steady state or equilibrium point is where the total force on each and every node is zero; this also occurs when the total potential energy of the system is minimized. Here an iterative minimization technique based on the nonlinear conjugate gradient method using Polak-Ribiere formula for finding search line direction is used. The algorithm is chosen because of its high convergence speed and robustness. The outline of the algorithm is: the total energy of a system is a function of all peridynamic nodes' coordinates. So in the multidimensional space formed from those coordinates, the energy function is a multidimensional surface. At each iteration, the conjugate gradient algorithm chooses a line on the energy surface and searches for point of minimum energy on that line, which is equivalent to finding where the projection of the total force on that line is zero. The force function on a specific search line is a one-variable function, thus various root finding methods can be used for finding the zero point, such as bisection, Newton–Raphson, or secant method. In this study, the secant method is used because it does not require to calculate the second derivative of energy, it only requires to calculate the first derivate of energy, which is force and is already formulated. The key of the method is optimizing the line search direction. Initially, this direction $\mathbf{d}_0$ is actually the total residual force $\mathbf{f}_0$ at time zero. In other words, the initial search direction of the conjugate gradient method is the same as the search direction of the steepest descent method [54]:

$$\mathbf{d}_0 = \mathbf{r}_0 = -W'(\mathbf{y}_0) \tag{2.46}$$

At a step *i,* on the search line $\mathbf{d}_i$, find the scalar variable α_i that minimizes the energy $W(\mathbf{y}_i + \alpha_i \mathbf{d}_i)$.

At next step *i*+1, the new coordinates are $\mathbf{y}_{i+1} = \mathbf{y}_i + \alpha_i \mathbf{d}_i$. The new search direction $\mathbf{d}_{i+1}$ is updated, using the information of the total residual forces at the last two steps $\mathbf{r}_i$ and $\mathbf{r}_{i+1}$:

$$\mathbf{d}_{i+1} = \beta_{i+1}\mathbf{d}_i + \mathbf{r}_{i+1} \tag{2.47}$$

where β_{i+1} is a non-unit, scalar number. There are various formulas for this variable. In this study, the Polak-Ribiere formula is used [54]:

$$\beta_{i+1}^{PR} = \frac{\mathbf{r}_{i+1}^T(\mathbf{r}_{i+1} - \mathbf{r}_i)}{\mathbf{r}_i^T\,\mathbf{r}_i} \tag{2.48}$$

The superscript *T* in (2.48) denotes the mathematical transpose. Thus the product used in (2.48) is the inner product between two vectors. The Polak-Ribiere formula has the advantage of fast convergence speed, but it can in some cases cycle infinitively [54]. To avoid this problem, the line search can be reset to the direction of the residual force when this happens. Mathematically, this is done simply by resetting β_{i+1}^{PR} to zero whenever the calculated value in (2.48) is negative:

$$\beta_{i+1}^{PR} = \max\left(\frac{\mathbf{r}_{i+1}^T(\mathbf{r}_{i+1} - \mathbf{r}_i)}{\mathbf{r}_i^T\,\mathbf{r}_i}, 0\right) \tag{2.49}$$

Figure 2.2 plots of the average von Mises stress vs. simulation step of a typical simulation. In Figure 2.2(a), dynamic relaxation with a constant viscosity coefficient is used. Each simulation step in this figure corresponds to a real time step of 5 nanoseconds. The viscosity coefficient is chosen large enough so the system goes to the final result as quickly as possible (near critical damping condition). In Figure 2.2(b), each step is simply a conjugate gradient step that does not correlate to any real time step. With energy minimization, peridynamic forces are elastic forces only, there is no need to add viscous forces to the system to find the solution. Though different in implementation, both methods give the same final result. However, the conjugate gradient method requires much fewer steps and is orders of magnitude faster than the dynamic relaxation method.

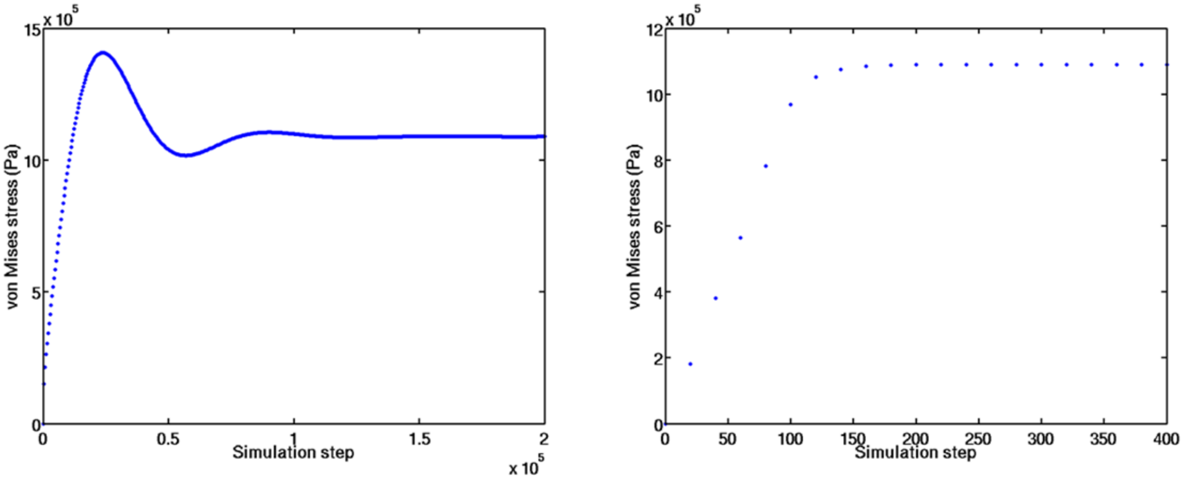

(a)

(b)

Figure 2.2. von Mises stress vs. simulation step in a system of 33144 nodes with (a) dynamic relaxation and (b) energy minimization.

2.4.2. Modifying the Node Interaction Volume

In peridynamic theory, each infinitesimal volume interacts with an infinite number of other volumes within a perfectly circular disk region. But in discrete numerical implementation, each peridynamic node has a finite volume defined by the node size r_i. Figure 2.3(a) shows two neighboring nodes with a horizon centered at node 1. Node 2 has a center located near the cut off distance of the horizon; only a part of its volume is inside the horizon. Thus, for interaction between node 2 and node 1, only the volume fraction inside the horizon is counted. In [19], the volume fraction around the cut-off distance decreases continuously from 1 to 1/2, then abruptly from ½ to 0 as the bond length increases. Here a volume fraction scheme similar to the one in [19] is used. The difference is that in this study, the volume fraction decreases continuously from 1 to 0 around the cut-off distance. In the 2D implementation, the volume fraction is approximated by a linearly decreasing function near the neighborhood boundary:

$$\nu(\mathbf{x}_\mathrm{p} - \mathbf{x}_\mathrm{i}) = \begin{cases} 1 & \text{if } |\mathbf{x}_\mathrm{p} - \mathbf{x}_\mathrm{i}| \leq \delta - \frac{r_\mathrm{p}}{2} \\ \frac{1}{2} + \frac{\delta - |\mathbf{x}_\mathrm{p} - \mathbf{x}_\mathrm{i}|}{r_\mathrm{p}} & \text{if } \delta - \frac{r_\mathrm{p}}{2} < |\mathbf{x}_\mathrm{p} - \mathbf{x}_\mathrm{i}| < \delta + \frac{r_\mathrm{p}}{2} \\ 0 & \text{if } |\mathbf{x}_\mathrm{p} - \mathbf{x}_\mathrm{i}| \geq \delta + \frac{r_\mathrm{p}}{2} \end{cases} \tag{2.50}$$

where $\mathbf{x}_\mathrm{i}$ and $\mathbf{x}_\mathrm{p}$ are positions of a node and its neighbor and r_p is the neighbor node's size. This volume fraction function is plotted in Figure 2.3(b). The benefit of this volume modification scheme is that it reduces the discretization effect, resulting in a more stable, faster m-convergence. Here m-convergence is the convergence of simulation results when the horizon is fixed while the node size is reduced, which is discussed further in the sections about convergence.

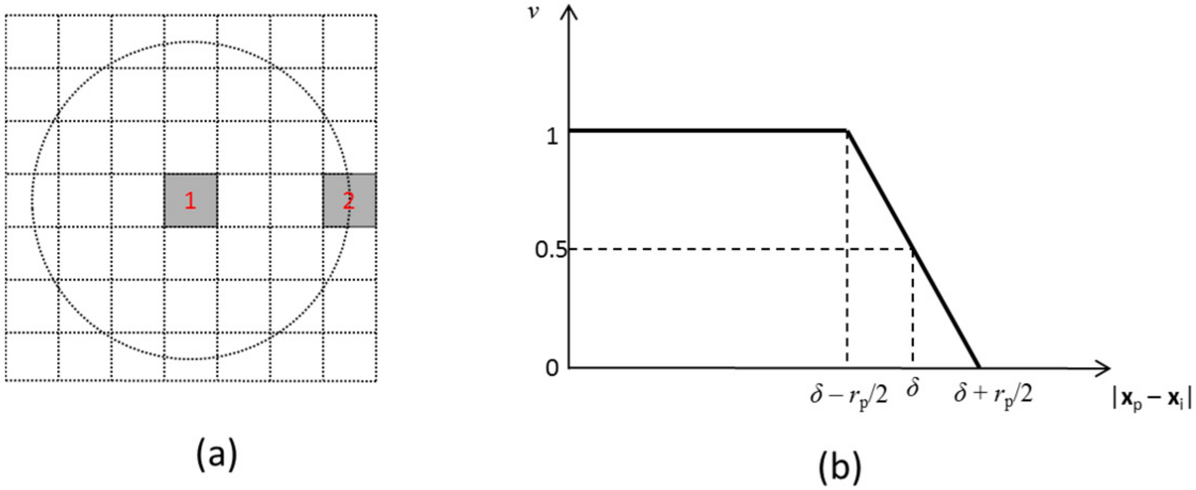

Figure 2.3. (a) Two-dimensional diagram showing discrete nodes with boundaries (dotted lines), node 2 has about half of its volume inside the horizon region of node 1. (b) Volume fraction as a function of distance.

2.5. Verification with FEM Analysis

The 2D peridynamics model for plane stress is implemented using Matlab code. The simulations are run on a CUDA-enabled, 384-core Graphic Processing Unit (GPU) installed on a personal computer with a 4-core Intel CPU. The simulations are written in parallel Matlab code to improve computation speed. Matlab's GPU-enabled functions enable the peridynamics code to be run in parallel in GPU computing, which results in a processing time 6 to 7 times faster than running on the CPU of the same computer. A simple rectangle plate with a hole in the center, shown in Figure 2.4, is used to validate the 2D peridynamics model. The plate is 50 mm by 100 mm and the hole has a radius of 10 mm. The left side of the plate is fixed while the right side is stretched under an evenly distributed tensile stress of 1 MPa.

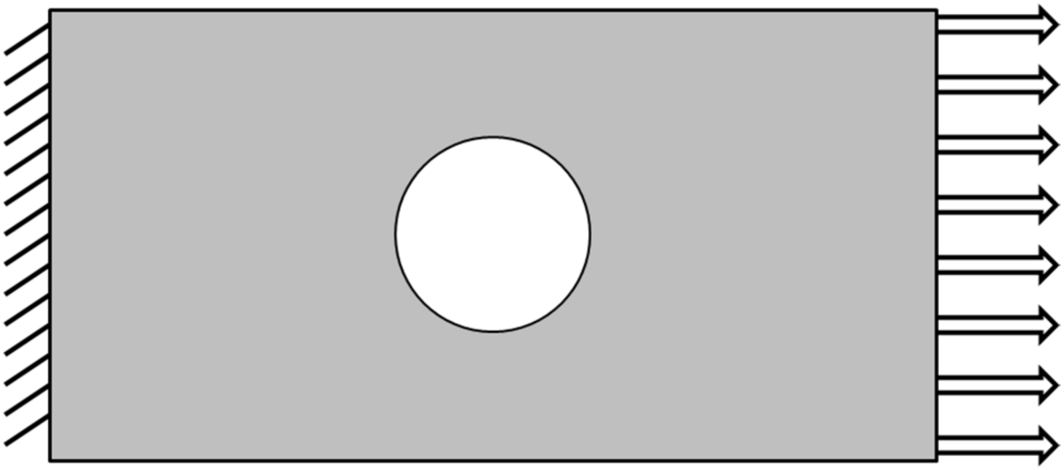

Figure 2.4. Rectangular plate with a hole in the middle. The left side is fixed and a tensile load is applied to the right.

The bulk modulus is set at k = 100 GPa and Poisson's ratio is set at v = 0.4. For computer simulation, the system is discretized by a uniform grid into a finite set of peridynamic nodes. The nodes that fall inside the hole are simply uncounted. Since the hole is of circular shape while the grid is a rectangular one, some geometry detail is lost around the hole edge, especially if the grid is coarse. A non-uniform grid that follow the geometrical contour as shown in [25] will preserve the hole's geometry better and might give more accurate results. The stationary displacements and von Mises stress distributions measured along the center horizontal and vertical lines are then compared to the same quantities obtained from a counterpart finite element model. To estimate the stress tensor in the 2D peridynamics model, the peridynamics "collapsed stress tensor" function [40] is used. It has been proven that the collapsed stress tensor is equivalent to the first Piola-Kirchoff stress tensor [40].

The results from peridynamic simulations are then matched with ones from finite elements simulations of the exact same sample geometry, physical properties, and testing conditions. All the finite element simulations are done with very fine meshes and quadratic shape functions to ensure that all the results converged accurately.

2.5.1. Convergence to Continuum Peridynamics

The peridynamics quantities are defined by integral equations. In numerical simulation, however, the continuum body is approximated by a system of a finite number of nodes, with each node interacting with a finite number of neighbor nodes and the peridynamics integrations are approximated by numerical integrations. Here a simple summation of every node is used in this article. In order to approximate the integrations adequately, each peridynamic node must have a sufficiently large number of neighbors. In other words, the ratio between the horizon size and node size must be sufficiently large.

To test the convergence in the 2D numerical simulation, the horizon is kept at a fixed value, $\delta = 3$ mm, while the node size r is reduced from 1.5 mm to 0.375 mm (in a single simulation, every node has the same size $r_i = r$). Thus, the ratio $m = \delta/r$ ranges from 2 to 8, as shown in Figures 2.5 and 2.6. This type of convergence is called "m-convergence" in [33, 47]. Figure 2.5 shows displacement and von Mises stress profiles observed on the central horizontal line of the samples (the red lines across the rectangles in Figure 2.5) with a fixed horizon size $\delta =$ 3mm and values of m ranging from 2 to 8, where $m = \delta/r$ is the ratio between the horizon and node sizes. Similarly, Figure 2.6 shows the displacement and stress profiles observed on the central vertical lines with the same fixed δ and m varying over the same range. From the graphs in Figures 2.5 and 2.6, both the displacement and stress profiles start to converge for

m >= 5, meaning that at m = 5 the discrete peridynamics implementation is close enough to the continuum peridynamic theory.

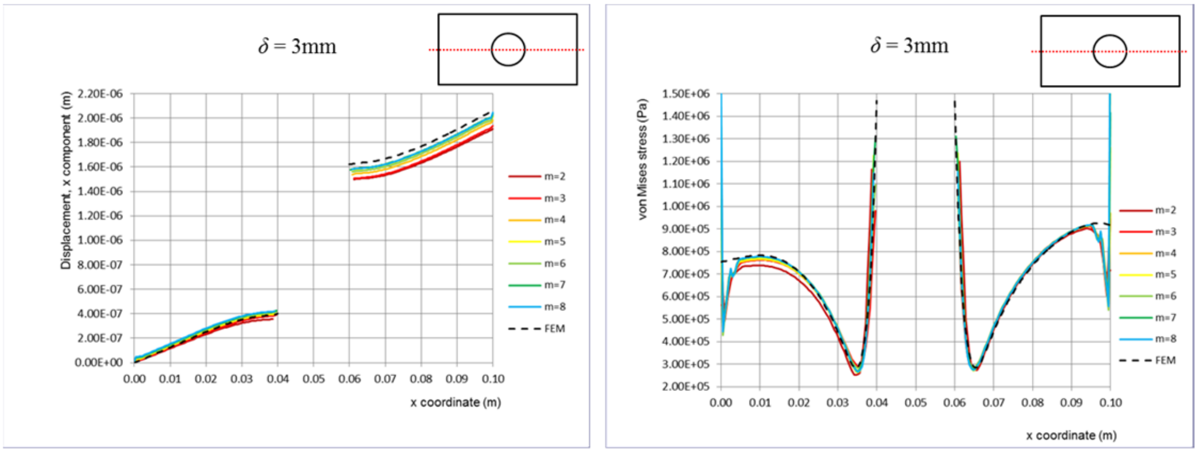

(a) (b)

Figure 2.5. Distribution along the horizontal line with different m values and a fixed δ. (a) Displacement vs. position (b) von Mises stress vs. position.

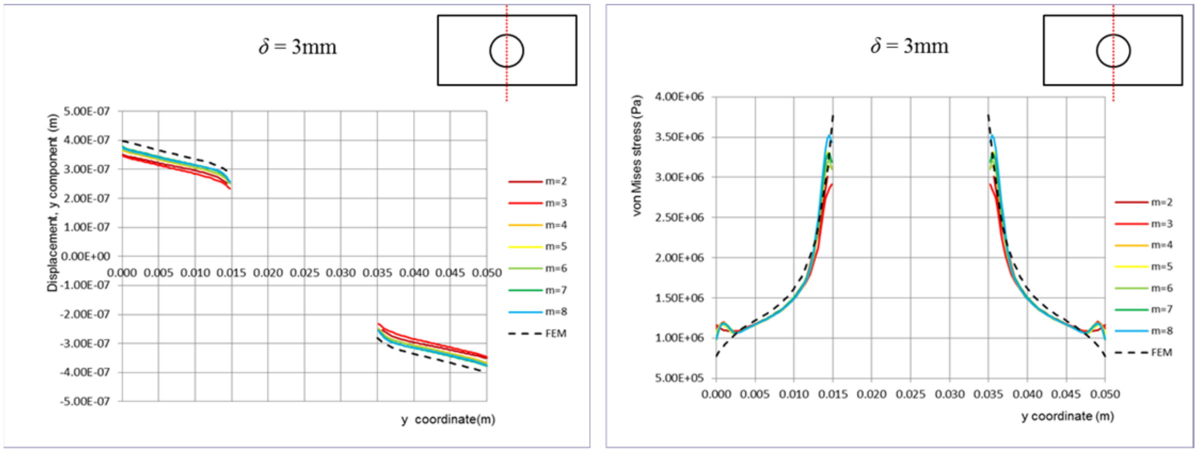

(a) (b)

Figure 2.6. Distribution along the vertical line with different m values and a fixed δ. (a) Displacement vs. position. (b) von Mises stress vs. position.

Figures 2.5(b) and 2.6(b) also show that, near the free boundaries, the von Mises stress shows some anomalies. In the thickness of about 2δ near the free boundaries, the stress in the peridynamic model always deviates from the FEM model, no matter what the values of *m* is. This is expected because the peridynamic collapsed stress tensor only converges to the classical mechanics stress tensor when there is a full neighborhood region (a disk in this case). A peridynamic node at an edge has only a half disk neighborhood region, while a node at a corner has only a quarter of a disk. Thus, near the boundaries, the system deviates from the theoretical model. This “skin effect” is a general issue in peridynamics models [42]. The thickness of this skin layer is reduced when the horizon size δ is reduced, however at the outermost peridynamic nodes, the peridynamic system will always be different from classical system regardless of horizon size. To reduce this effect, Macek and Silling [22] proposed a method to reduce this effect in bond-based models. Also see [55] for another possible method that may be applicable to both bond- and state- based models.

2.5.2. Convergence to Classical Mechanics

Peridynamic theory is a non-local theory based on integral equations, while classical mechanics is a local theory based on partial differential equations. It has been proven theoretically that peridynamics results converge to classical mechanics results when the horizon size goes to zero [40]. In practice, for steady-state problems this convergence occurs when the horizon size is small enough compared to the length scale of the stress/strain field in the system. For dynamic problems such as simulations of cracks, wave dispersion is strongly dependent on the horizon size [38]. In such cases the horizon should be chosen as small as possible while keeping m, the ratio between the horizon size and node size, sufficiently large, to have matching results to classical model. Also when the horizon is small, the skin effect is reduced as well since the skin's thickness is reduced. This convergence, when reducing horizon size, is called δ-convergence [33, 47].

To study δ-convergence, the 2D simulations are performed with horizon sizes decreasing from 3 mm to 1 mm. To study the influence of horizon size only, without the influence of m-convergence, the ratio m is fixed at $m = 5$ in Figures 2.7 and 2.8. Figures 2.7 and 2.8 show the displacement and stress profiles on the central horizontal and vertical lines δ varying from 3 mm to 1mm. Figures 2.7 and 2.8 show that as δ decreases, the peridynamic displacement and stress profiles match more closely to the finite element results, again except at the nodes at the free boundaries. This is because at those nodes, the neighborhood within a horizon is not a full circle, regardless of the horizon size, thus causing the skin effect to happen. The difference between Figures 2.7(b) and Figure 2.5(b), and between Figure 2.8(b) and Figure 2.6(b) is, now as the horizon decreases, the skin layer where there are stress anomalies reduces in thickness. Figure 2.8(b) also shows that at the uppermost and lowermost points of the hole, the stress concentration factor of both the peridynamic and the FEM model is about 3.7. It is worthy to note that in theoretical analysis of stress concentration factor around a hole in an infinite media under uniaxial stress condition, the concentration factor at those points is 3, which is of similar range but not the exact value found here. The reason of difference is in these numerical simulations, the media is not infinite. Also, in the peridynamic and FEM simulations here, the left edge of the rectangle is fixed and not allowed to shrink vertically; thus the externally applied stress condition is not purely uniaxial like in the theoretical analysis.

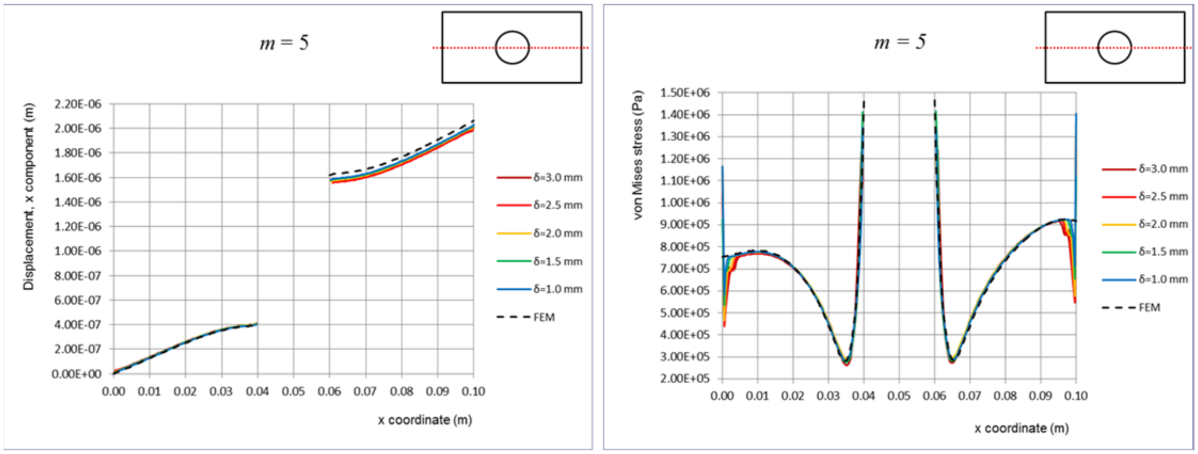

(a)

(b)

Figure 2.7. Distribution along the horizontal line with different horizon sizes and a fixed m. (a) Displacement vs. position. (b) von Mises stress vs. position.

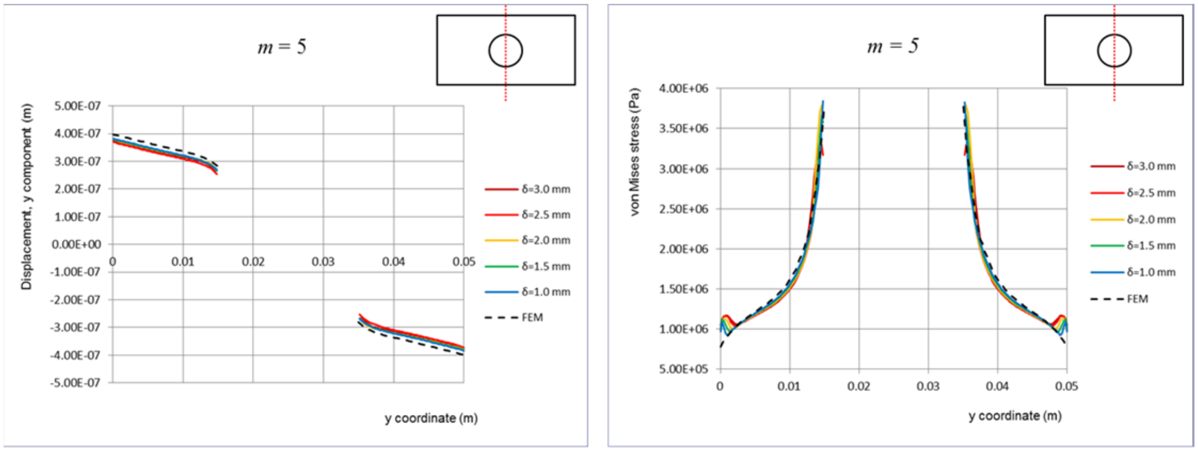

(a)

(b)

Figure 2.8. Distribution along the vertical line with different horizon sizes and a fixed m. (a) Displacement vs. position. (b) von Mises stress vs. position.

For a visual comparison, Figure 2.9 shows both FEM and peridynamics samples with displacements magnified 15,000 times. In Figure 2.9(b), the horizon is set at smallest value $\delta = 1$ mm, and $m = 5$. The colors denote the von Mises stress levels. Again, the two samples have similar deformed shapes and stress distribution patterns except near the free boundaries.

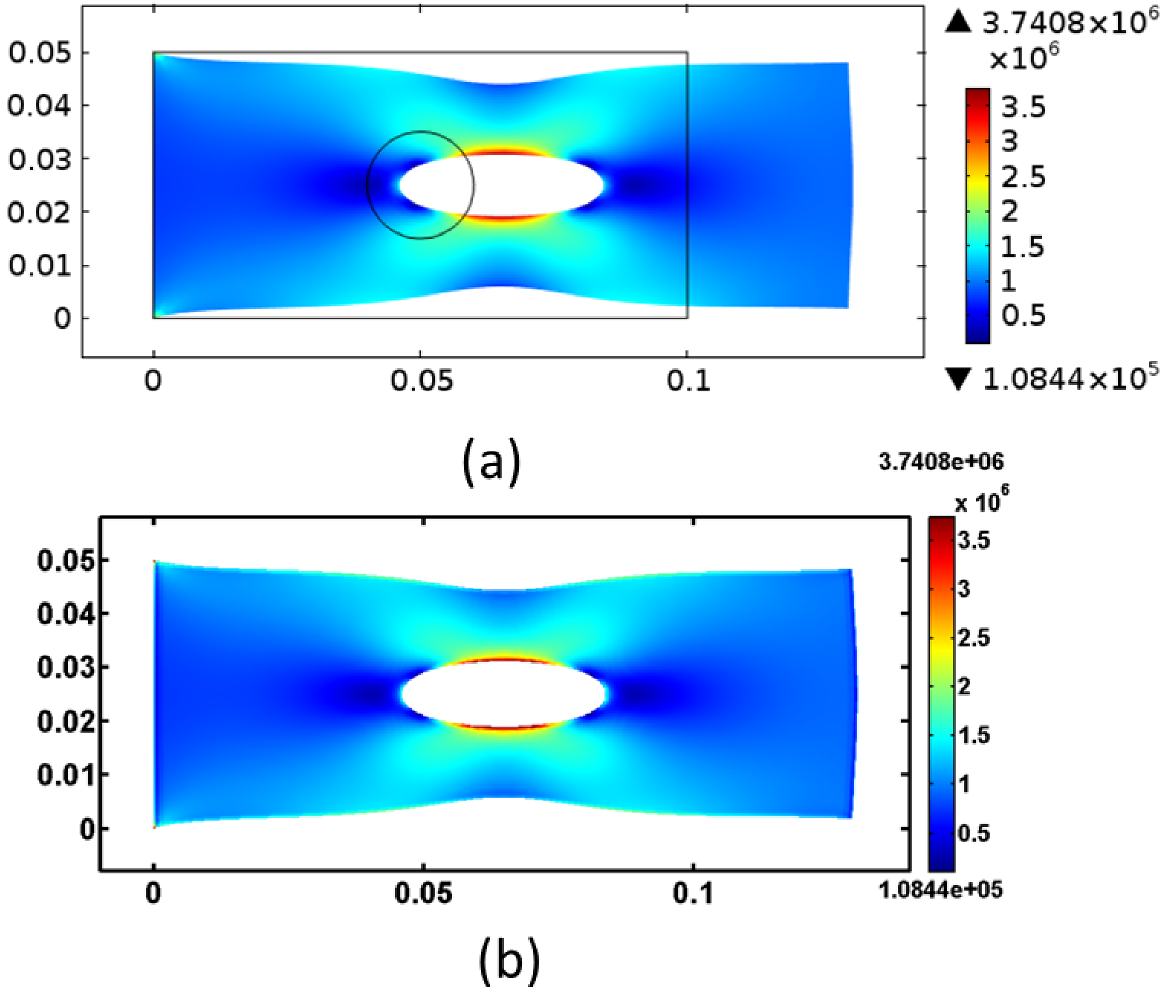

Figure 2.9. von Mises stress distribution of (a) finite element simulation and (b) peridynamics simulation. Colors denote stress levels. Displacements are magnified 15,000 times in both cases.

2.6. Peridynamics Stress at the Sharp Corners

It is known that in FEM simulation using classical mechanics, the stress at a sharp corner/notch may increase to infinity when the element size is reduced to zero. Does the same phenomenon happen in peridynamics, when horizon size is reduced to zero? To answer this question, a rectangle plate with a square hole in its center is simulated to investigate the stress concentration. The plate is 50 mm by 100 mm and the square hole has the edge dimension of 14.14 mm. The plate and the testing conditions are illustrated in Figure 2.10. Similar to previous sample, the left side of the plate is fixed while the right side is stretched under an evenly distributed tensile stress of 1 MPa. While the bulk modulus is also set at k = 100 GPa and Poisson's ratio at v = 0.4. Figure 2.11 shows not all sharp corners of the hole have stress concentration, only the uppermost and lowermost corners are where the stress concentrates. While Figure 2.12 shows that as the horizon size reduces, the stress at the corner increases and does not show any sign of saturation. This is similar to the result observed in classical mechanics simulation. This is understandable because when the horizon size is the length scale of the non-local peridynamic theory, thus the smaller the horizon size the more local the peridynamic theory becomes. Classical mechanics can be viewed as the convergence limit of peridynamics when the horizon size vanishes [20]. This simulation shows that 2D state based peridynamic model proposed in this research also shows the convergence to classical mechanics behavior observed in previous peridynamic models.

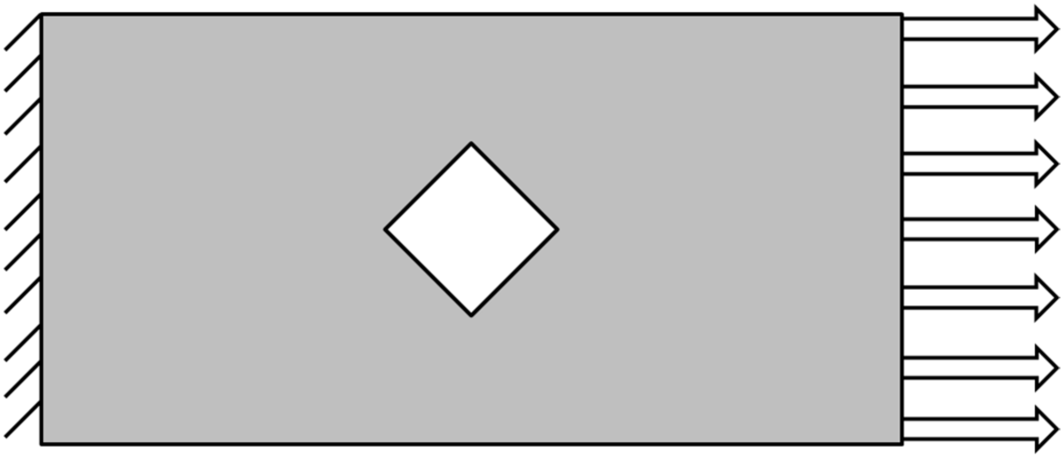

Figure 2.10. Rectangular plate with a square hole in the middle. The left side is fixed and a tensile load is applied to the right.

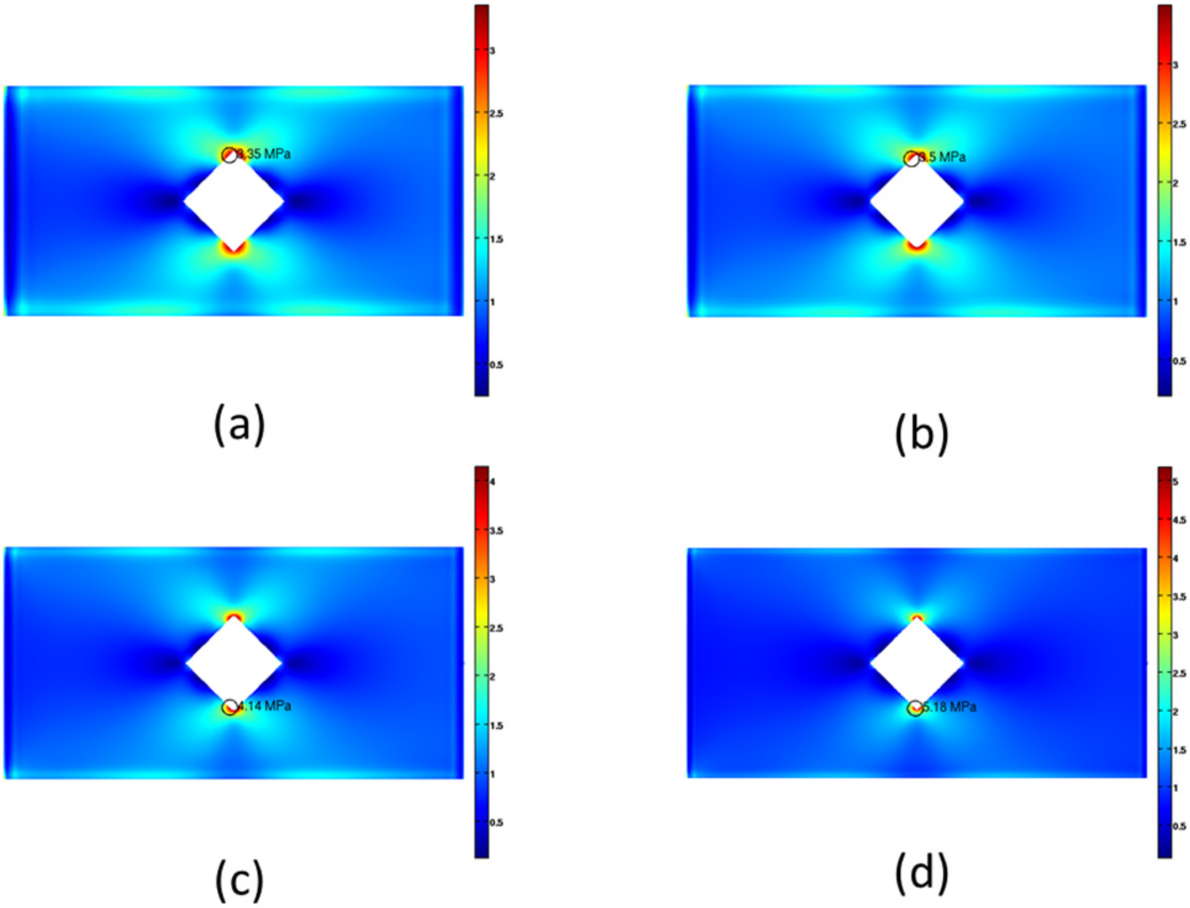

Figure 2.11. Tensile test with different values of horizon size δ. (a) δ = 5 mm. (b) δ = 4 mm. (c) δ = 3 mm. (d) δ = 2mm.

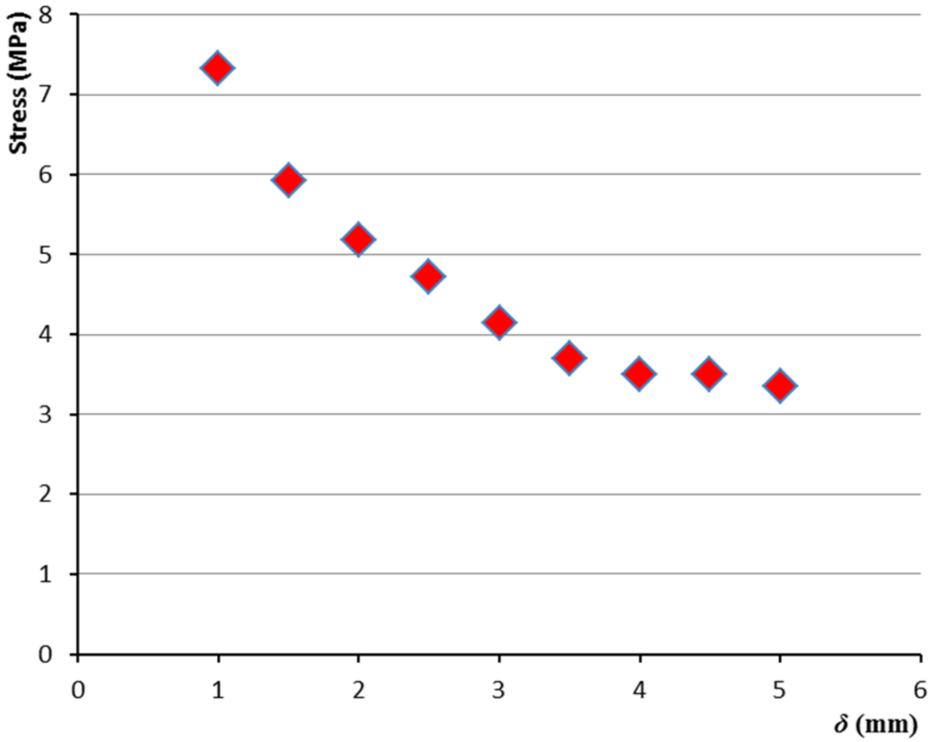

Figure 2.12. Dependence of von Mises stress at the sharp corner on horizon size.

3. Bi2212 STUDY RESULTS

3.1. Scanning Electron Microscopy Image Analysis

The simulations use longitudinal and cross-sectional SEM images as input for the peridynamic system. Figure 3.1 shows the longitudinal SEM images of (a) single and (b) multiple Bi2212 filaments embedded in silver matrix. These two images are used as initial input for peridynamic simulations. As seen on the images, the silver is of a light grey color while the superconducting filaments actually contain many phases: the Bi2212 with dark grey color, the Bi2201 phase of light grey color, holes and AEC phases usually appear as dark regions in the SEM images. Thus for the simulation program to recognize different phases and to simplify the microstructure, silver and Bi2212 regions are selected either by their grayness levels or by using magic wand tool in Photoshop software. Then the silver regions are marked with white color, Bi2212 regions with black color, while defects are marked with red color. Figure 3.1(c) and 3.1(d) show the processed images from Figures 3.1(a) and 3.1(b). Notice that the black region in Figure 3.1(b) is marked with the red color in Figure 3.1(d). The simulation program will then read the processed images and assign the black/white/red colors to different phases with their matching physical constants.

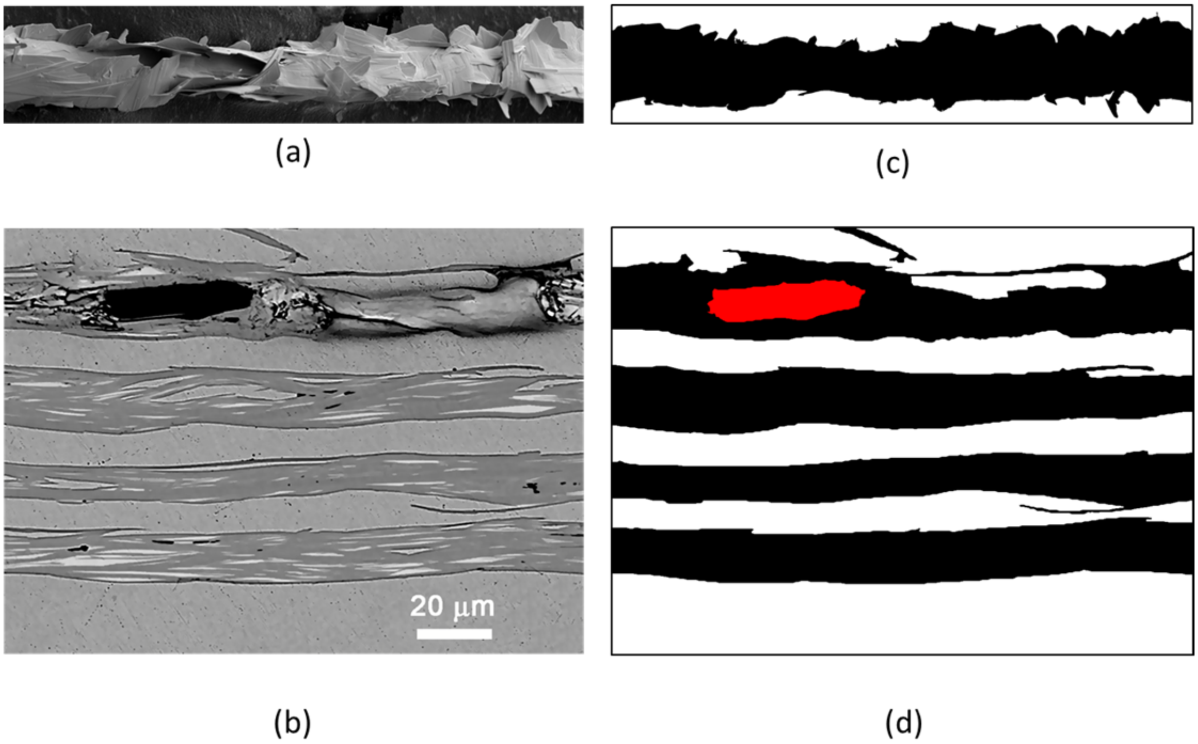

Figure 3.1. (a) Longitudinal SEM image of a Bi2212 filament. (b) Longitudinal SEM image of multiple Bi2212 filaments. (c) Processed microstructure from (a). (d) Processed microstructure from (b).

Using the natural defects has the disadvantage that there is no control of the defect size and shape. And currently, there is little experimental study that link specific defect geometries and macroscopic properties. To study the effects of defect size and shape, artificial defects are also introduced into the system by also marking certain region with red color. Figure 3.2 shows all different types of defect geometries used in this study, including natural and artificial defects. The reason to introduce artificial defects into the simulation is because of the lack of high resolution SEM images with desired variation in defect geometries. Also, artificial defects allow the study to isolate and control influences of a single defect type. While in "real life" SEM images, different defects and phase shapes co-exist in one sample thus experimentally, it is difficult to attribute which microstructure feature dominates the macroscopic properties of the wires.

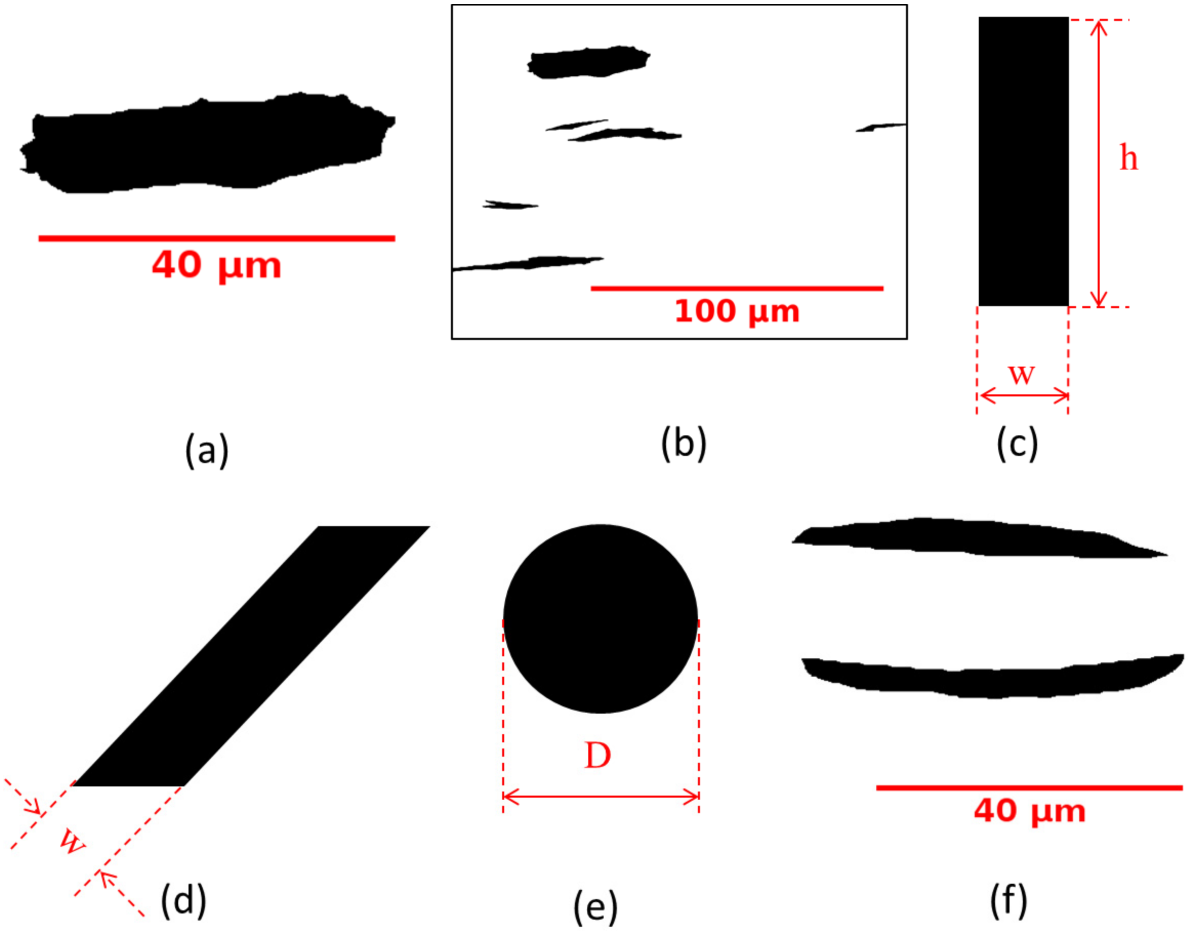

Figure 3.2. Different defect shapes studied. (a) Single real defect. (b) Multiple real defects. (c) Artificial rectangle defect. (d) Artificial 45 degree slanted defect. (e) Artificial circular defect. (f) Artificial irregular defect.

After being processed, the images are put into a Matlab program for discretization to generate a discrete peridynamic system. In the discretization program, the red areas will be either ignored to create voids (no peridynamic node) or set up as solid defects with certain bulk modulus and Poisson's ratio.

3.2. Peridynamics System Construction

The peridynamics theory is a continuum theory in the sense that the media is continuous. Though analytic solution can be found in very simple cases, the vast majority of peridynamic applications use numerical simulation which requires approximating the continuous media by a discrete set of peridynamic nodes. In this article, an even rectangular grid is used to set up these nodes. Figure 3.3(a) illustrates the discretization scheme on a processed SEM image, in which the grid is drawn much coarse that what is really used to give a clear illustration. Each square of the grid has a finite volume and is assigned to a peridynamic node located at the center of the square. Since each peridynamic node is associated with a finite volume, peridynamic volume integrations are simply estimated by summations in numerical simulation. It's important to note that after discretization, each peridynamic node is simply a computation point and does not "remember" its shape anymore. In other words, geometrical details at the node level are lost.

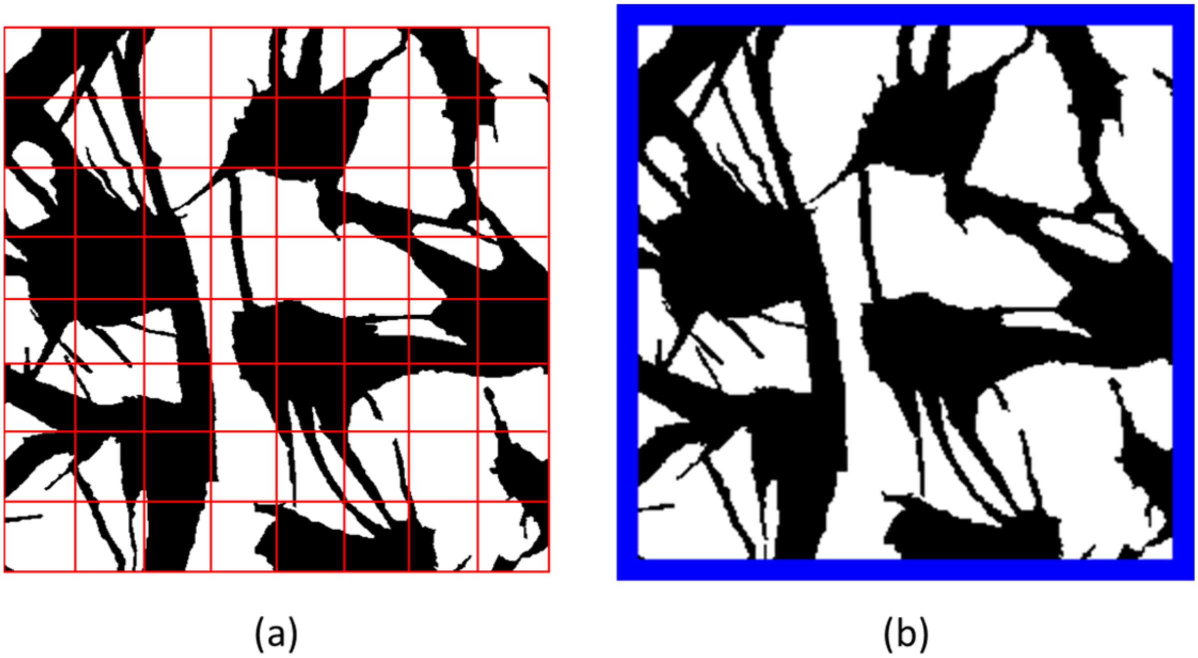

Figure 3.3. (a) Discretization scheme from SEM image to peridynamic system. (b) Additional peridynamic nodes are added at the free boundary.

Each peridynamic node is assigned a phase based on the phase of the original square. So at the phase boundary in the image, there could be squares that contain pixels of multiple phases. For these heterogeneous squares, the phase of the peridynamic node is assigned to the phase of the center pixel in that square. So the grid size determines what how much of original geometry in the SEM image is conserved: the smaller the grid size, the more detail is conserved in the peridynamic system. Also, after the discretization process from the processed SEM image to a finite set of peridynamic nodes, 10 additional layers of peridynamic nodes are added around the outer boundary of the system as illustrated in Figure 3.3(b). In Figure 3.3 (b), these peridynamic nodes are of blue color. In the simulations, these nodes are set up of the same mechanical constants as the nodes in the silver phase (white color). Later in final visualization of results, these additional nodes are ignored. The reason for adding then removing them later is, at the outer boundary the peridynamic stress shows deviation from classical mechanics stress especially when there is externally applied force on these outer nodes (the $\mathbf{b}(\mathbf{x}, t)$ in the equation of motion). This effect has been shown in [56]. So adding then removing these dummy nodes helps removing those anomalies.

The limitation using the digital image directly and the uniform mesh to discretize the microstructure into a discrete peridynamics system is, in order to have good approximation of the microstructure and test the convergence, one would want to refine the mesh size and the horizon size of the peridynamics model. The finer the grid is, the less relative amount of these heterogeneous squares will become and the closer the peridynamic system will be to the original SEM image. But if the grid is too fine, the system will also include artificial sharp corners caused by the nature of the digital, pixel images. Figure 3.4(a) shows the discretization scheme where the grid size is equal to pixel size, and Figure 3.4(b) shows another where grid size is only half of pixel size. In Figure 3.4(a), at the phase interface the red and blue peridynamic nodes align to smooth straight lines; while in Figure 3.4(b), they do not: the red and blue nodes now form jagged lines at their interface. In other words, oversampling in Figure 3.4(b) introduces artificial sharp corners to the peridynamic system. Thus it is advantageous to never get the grid size smaller than pixel size. In this study, the grid size is set to 2 times of the pixel size. The horizon is set up of 5 times the peridynamic node size in all simulations.

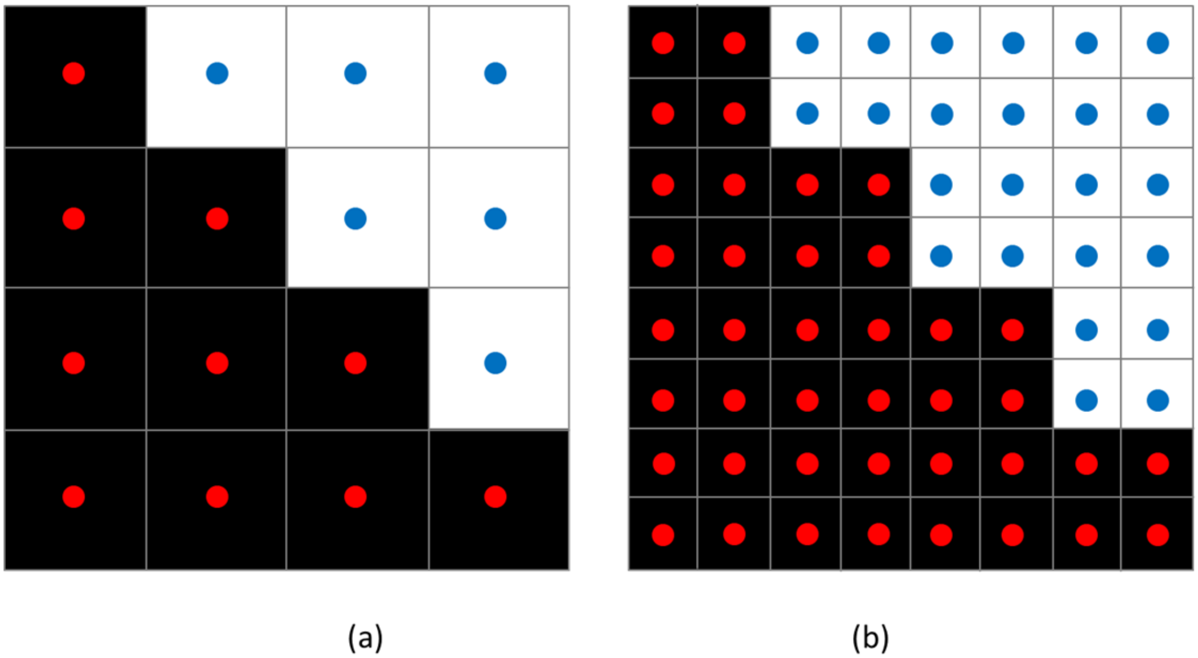

Figure 3.4. Effects of discretization grid size on phase boundary. (a) When grid size is equal to pixel size. (b) When grid size is half of pixel size.

After discretization, in simulation each peridynamic node is set up with specific mechanical properties according to their associated phase. Silver's mechanical properties are set at: bulk modulus 91.0 GPa, Poisson's ratio 0.37. Bi2212 phase's bulk modulus is 21.9 GPa, Poisson's ratio is 0.2. Since there is no experimental information of mechanical properties of non-superconducting phases (such as AEC and Bi2201), their Poisson's ratio is also set at 0.20 like Bi2212. But their bulk modulus is set either half that of Bi2212 (10.95 GPa) or twice of it (43.80 GPa).

3.3. Peridynamic Simulation Method

Similar to molecular dynamics, in peridynamics the static or steady state could be achieved by either adding a viscous force to dynamically relaxing the system into equilibrium position or by directly finding it with energy minimization. Dynamic adaptive relaxation technique has been used in other peridynamics studies to find static solutions with improved speed compared to regular relaxation with fixed coefficient of viscosity [24, 28, 30]. In this study, static stress distribution in Bi2212 wires is achieved by energy minimization with non-linear conjugate gradient algorithm using Polak-Ribiere line search, the same method used in chapter 2 for verification of the theory. The 2D plane stress model developed in chapter 2 is used for computer simulations. Typically, peridynamic systems contain from 100,000 to 400,000 computation nodes and require 1 to 2 hours per simulation. Each simulation is stopped when the stress distribution in the sample becomes stable and no longer changes with additional iteration steps.

Stress tensor estimation:

In classical mechanics, interactions are contact forces where interactions happen at infinitesimal distances, and stress is defined as force per unit surface area. But in peridynamics, interactions happen over finite distances. As mentioned in chapter 1, the "collapsed stress tensor" is defined and proven to be equivalent to the Piola-Kirchhoff stress in classical mechanics [20, 35, 40]. In this article, a slightly modified form of collapsed stress tensor (equation (1.26)) is used to calculate stress tensor at a point $\mathbf{x}$:

$$\boldsymbol{\sigma}(\mathbf{x}) = \frac{1}{2}\int_{\mathrm{H}}(\underline{\mathbf{T}}[\mathbf{x}, t]\langle\mathbf{x}' - \mathbf{x}\rangle - \underline{\mathbf{T}}[\mathbf{x}', \mathrm{t}]\langle\mathbf{x} - \mathbf{x}'\rangle) \otimes (\mathbf{x}' - \mathbf{x})\mathrm{d}V_{\mathbf{x}'}, \tag{3.1}$$

where $\boldsymbol{\sigma}$ is the stress tensor**,** $\mathbf{x}$ is the point/node of interest, **x'** is another peridynamic node interacting with the node $\mathbf{x}$, thus **x'-x** is the bond vector. The $\otimes$ is the symbol for dyadic product of two vectors, which results in a tensor.

The reason for using this modified formula is, the formula of collapsed stress tensor in equation (1.26) is more suitable for a single phase peridynamics system, where all the nodes are of the same phase. It is because when the horizon size is small enough: $\underline{\mathbf{T}}[\mathbf{x},t]\langle\mathbf{x}'-\mathbf{x}\rangle \approx -\underline{\mathbf{T}}[\mathbf{x}',\mathrm{t}]\langle\mathbf{x}-\mathbf{x}'\rangle \approx \frac{1}{2}\left(\underline{\mathbf{T}}[\mathbf{x},t]\langle\mathbf{x}'-\mathbf{x}\rangle - \underline{\mathbf{T}}[\mathbf{x}',\mathrm{t}]\langle\mathbf{x}-\mathbf{x}'\rangle\right)$. So for one phase material, the equations (1.26) and (3.1) are essentially equal. But in this article, there are multiple phases in the peridynamic systems, and for interactions between 2 peridynamic nodes of different phases, $\underline{\mathbf{T}}[\mathbf{x},t]\langle\mathbf{x}'-\mathbf{x}\rangle$ and $-\underline{\mathbf{T}}[\mathbf{x}',\mathrm{t}]\langle\mathbf{x}-\mathbf{x}'\rangle$ will always be different from each other no matter how small the horizon size is, thus in this case equation (3.1) is chosen for stress calculation. It is worth noting that equation (3.1) is also applicable for one phase, not just multiphase, materials.

3.4. Simulation Results

Because of the complex phase arrangements, stress state at a local point inside the Bi2212 wires is almost always multi-axial, even when the externally applied load is uniaxial. Thus von Mises stress is used to investigate the stress distribution and concentration inside the wires. von Mises stress is directly related to deviatoric strain energy density and is a commonly used criterion to assess stress states in metallic materials. It is important to note that if the stress state is homogeneous and uniaxial, von Mises stress is equal to the externally applied, macroscopic stress.

All the simulations in this study are 0.1% macroscopic strain tests, implemented by moving the outermost nodes on the left and right side of the peridynamic system a total distance of 0.1% the sample length then keep them fixed. The fixed macroscopic strain (instead of stress) tests are chosen to minimize the extensive effect of a defect's volume relative to the whole sample on the outcome. Also, different SEM images have slightly different ratios of silver and non-silver phases. Fixed macroscopic stress tests would make comparing results between images less meaningful, because the results would also be influenced by phase volume ratio, not just microscopic structure which is the focus of this study.

3.4.1. Samples with no defect

Figure 3.5(a) shows stress distribution in a sample with a single Bi2212 filament in the middle, at 0.1% macroscopic strain condition. Here the colors denote the von Mises stress levels, with red color being the highest and blue color the lowest value in the color bar. Figure 3.5(b) is the 3D presentation of the stress distribution on the same sample, with the von Mises stress displayed both by color and by height (z axis). The average, macroscopic stress applied on the two ends of the sample is 56.4 MPa. The highest von Mises stress in Bi2212 phase is 70.6 MPa, while in silver the highest value is 88.9 MPa, both are higher than the macroscopic stress. As Figure 3.5(b) shows, the stress in both Bi2212 and silver tends to concentrate at their interface where the Bi2212 is of convex shape and conversely, silver phase is concave. This is similar to the findings in [15], except that in this study a real microstructure from SEM image is used. Experimental studies have shown the intrinsic fracture strain in Bi2212 phase is about 0.12% [57, 58], which is equivalent to fracture stress of 47.3 MPa; while the yield point in silver is generally accepted at 0.076% strain or 54MPa stress. Thus at this test condition in a real experiment, certain parts of Bi2212 and silver phases would have past the fracture/yielding point and the assumed linear elasticity of the model would not be adequate for them. The value of the results is that they show the relative stress distribution in the elastic region, because in the elastic region spatial distribution of stress is independent of strain. Meanwhile, the magnitude of stress (both average and maximum stress) is proportional to the applied strain. So by linear interpolation, it could be calculated from Figure 3.5 results that the maximum stress in silver will reach the yielding value 54MPa when the macroscopic strain is approximately 0.061%. At that 0.061% macroscopic strain condition, the maximum stress in Bi2212 would be 42.9 MPa, slightly below the fracture stress for the material. It is worthy to note that as Figure 3.5 shows, due to the complex microstructure there is a large variation of local stress in Bi2212 and silver, so not every point in a same phase reaches the yielding/fracture stress at the same time. In fact, even at 0.1% strain condition, stress in a large proportion of Bi2212 is still under the limit. This explains why in experiments, the material does not show the sudden degradation of critical current with increasing strain. Due to variation in stress concentration factor, different parts of Bi2212 phase would break at different strain values.

It is worth noting that in all simulations in this article, the Bi2212 is set up as an isotropic, continuous phase. But experimental studies have shown that there are colonies of grains inside the Bi2212 phase, and it is suggested that the boundaries between the colonies are mechanically weaker and could be prone to breakage [59, 60]. There have not been quantitative experimental results for the mechanical properties of these boundaries, thus they are not included in this study. A more complex model including these boundaries would yield a more complete understanding of the Bi2212 wires' mechanical behavior.

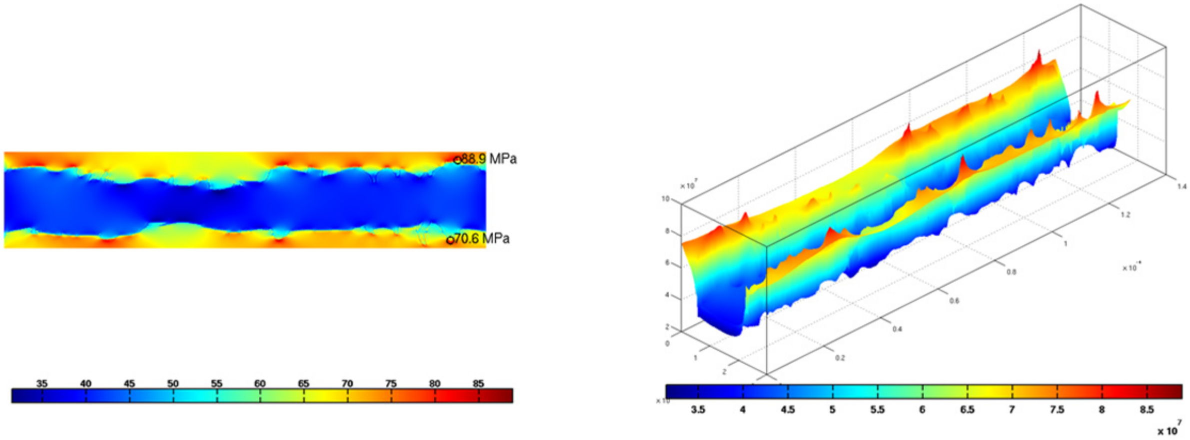

(a) (b)

Figure 3.5. von Mises stress distribution in single-filament sample (a) 2D representation of the stress. (b) 3D representation of the stress, showing the concentrations at the phase boundary.

In Figure 3.5, there is only one filament in the sample, one may question if the result from the simulation could be representative of the Bi2212 wires, which may contain hundreds of filaments. Thus in Figure 3.6, multiple filament SEM images are used for simulation to investigate possible interactions. Figure 3.6(a) shows simulation result of von Mises stress distribution in the sample with no defect; this figure is frequently used later to compare with other figures with defect throughout the whole study. The maximum stresses in Figure 3.6(a) are in the same range as Figure 3.5(a), 67.7 MPa in Bi2212 and 88.1 MPa in silver. This is understandable because both Figures 3.5(a) and 3.6(a) are of defect-free samples; the only difference between them is single filament versus multiple filaments in a sample.

The simulations using the longitudinal SEM images do not show an important microstructure feature of Bi2212 wires, the interfilament bridges. Usually, in longitudinal SEM images, these intergrowths are not well captured due to the difficulties in the sample preparing process. So a cross-sectional image with visible bridges is used in Figure 3.6(b) to study the effects of the bridges to stress concentration. The highest von Mises stresses in Figure 3.6(b) are of the similar range as in Figures 3.5(a) and 3.6(a), 72.1 MPa in Bi2212 and 81.6 MPa in silver. The only difference is now the stress is located in the bridges that run in the vertical direction, perpendicular to the external force direction (horizontal). The protruding parts of Bi2212 phase in Figure 3.5(a) could be also viewed as unconnected bridges. So the simulations indicate that in Bi2212 wires, while bridges are important to carrying current yet they also bear more mechanical load than the main filament thus will break first if external forces are high enough.

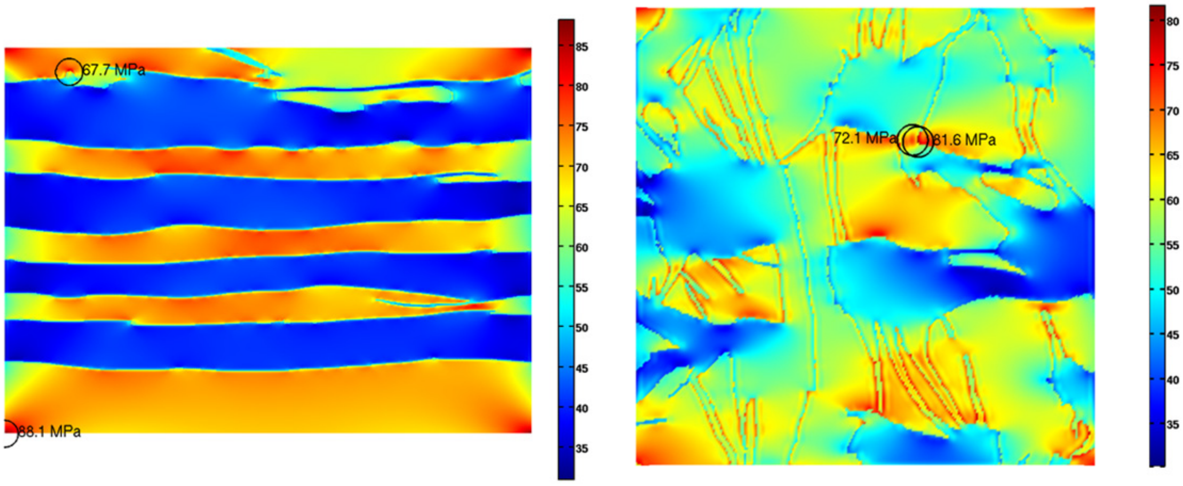

(a) (b)

Figure 3.6. von Mises stress distribution in a cross-sectional microstructure with multiple filaments. (a) Longitudinal image. (b) Cross-sectional image.

3.4.2. Samples with a single natural defect from a SEM image

In the samples in the previous section, there are no defects such as voids or secondary phases. But numerous experiments have shown there are such defects in in Bi2212 wires. For example, Figure 3.1(b) one can see multiple defects inside the Bi2212 filaments. The black area defect in the uppermost filament is of the shape (a) in Figure 3.2. This natural defect is set up either as a void or a solid phase in the simulations in this section. In reality, defects always vary in both shape and stiffness, thus it is difficult to compare and attribute the macroscopic outcome to the influence of the microscopic defect geometry or stiffness. Thus this is one advantage of using simulations: because the same geometry is set up for different defect phases, the influence of defect geometry when comparing the different results is eliminated.

In Figure 3.7(a) the defect is set up as a void. While in Figure 3.7(b) it is set up as a phase with same Poisson's ratio but half the bulk modulus of Bi2212 phase (10.95 GPa), this phase is referred to as "soft phase" in this study. In Figure 3.7(c) it is set up with twice the bulk modulus of Bi2212 phase (43.80 GPa), and is referred to as "hard phase". Figure 3.7(a) shows when the defect is a void, the maximum stress in Bi2212 phase increases significantly from 67.7 MPa (Figure 3.6(a)) to 111 MPa, and the maximum stress in Bi2212 no longer stays at the interface but rather at the void boundary. The maximum stress in silver also increases from 88.1 MPa to 89.9 MPa and is now at the Bi2212/silver boundary near the void defect. This indicates that voids may have more negative influence on the wire strength than the rough Bi2212/silver interface.

Secondary phases do not seem to impact the stress concentration in Figures 3.7(b, c). Compared with Figure 3.6(a), the maximum stress in Bi2212 phase in Figures 3.7(b, c) stays at the same place and is of nearly the same value. And the maximum stress in silver is still at a corner of the figures.

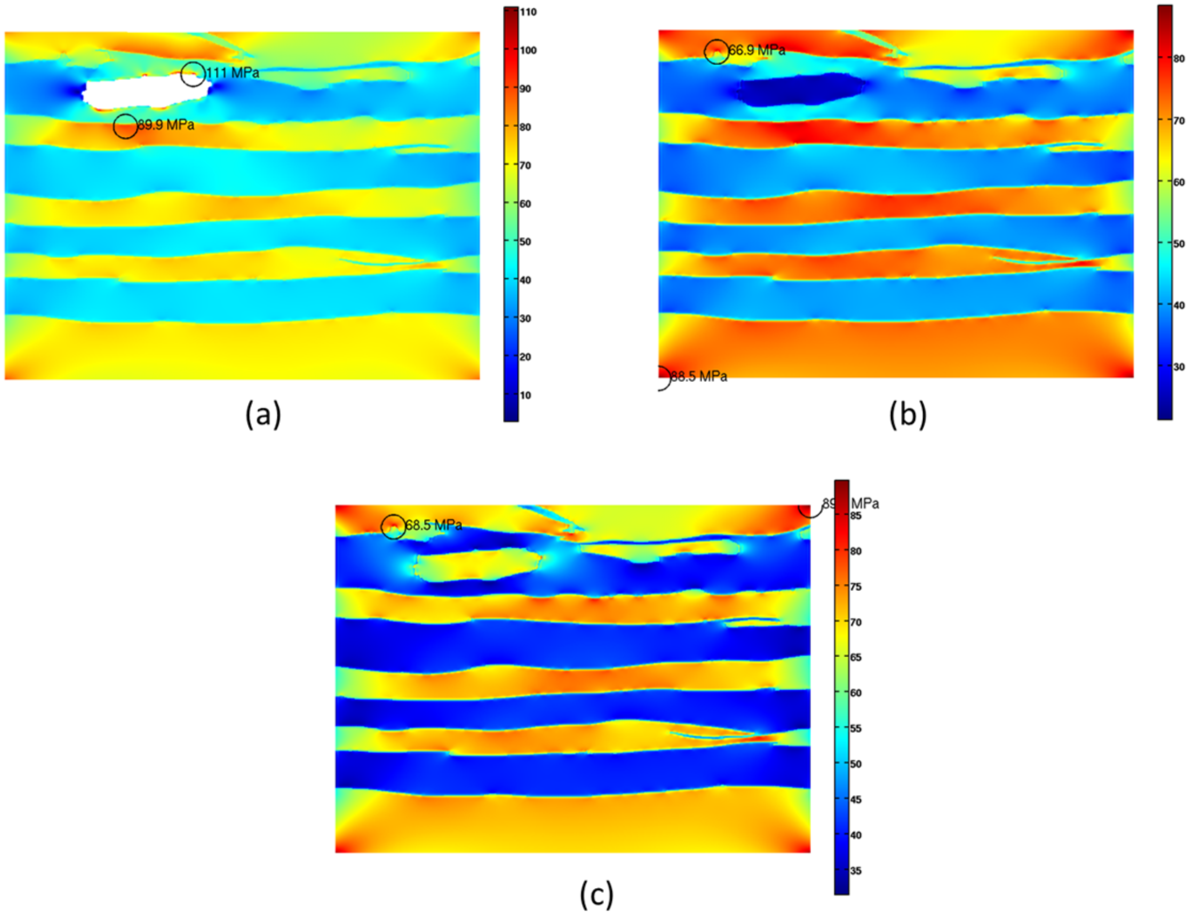

Figure 3.7. von Mises stress distribution in the multiple-filament SEM image. (a) When there is a single void defect. (b) When the defect is a soft phase. (c) When the defect is a hard phase.

3.4.3. Samples with a multiple natural defects from a SEM image

To study the effects of multiple defects, in Figure 3.8(a) von Mises stress distribution in the presence of multiple voids is presented. Similar to the previous case, in Figure 3.8(b) the voids are replaced by the "soft phase" with half the bulk modulus of Bi2212; and in Figure

3.8(c) the defects are of a “hard phase” with twice the bulk modulus of Bi2212. These defects are also natural defects and are of shape (b) Figure 3.2.

Figure 3.8 differs from Figure 3.7 because of multiple defects instead of only one defect. The results however are remarkably similar: the stress concentration is the highest in the sample with voids, while samples with soft and hard secondary phases do not result in significant change in maximum stresses (compared to the sample without defect). The similarity between them suggests that there is little mechanical interaction of defects in different filaments: defects in a filament seem to only influence stress concentration in that filament and not others, in other words they are isolated from each other by the silver matrix. This could be because of sufficient silver thickness between filaments. It still remains to see whether a thinner silver insulation layer between the filament would result in more interaction between defects or not.

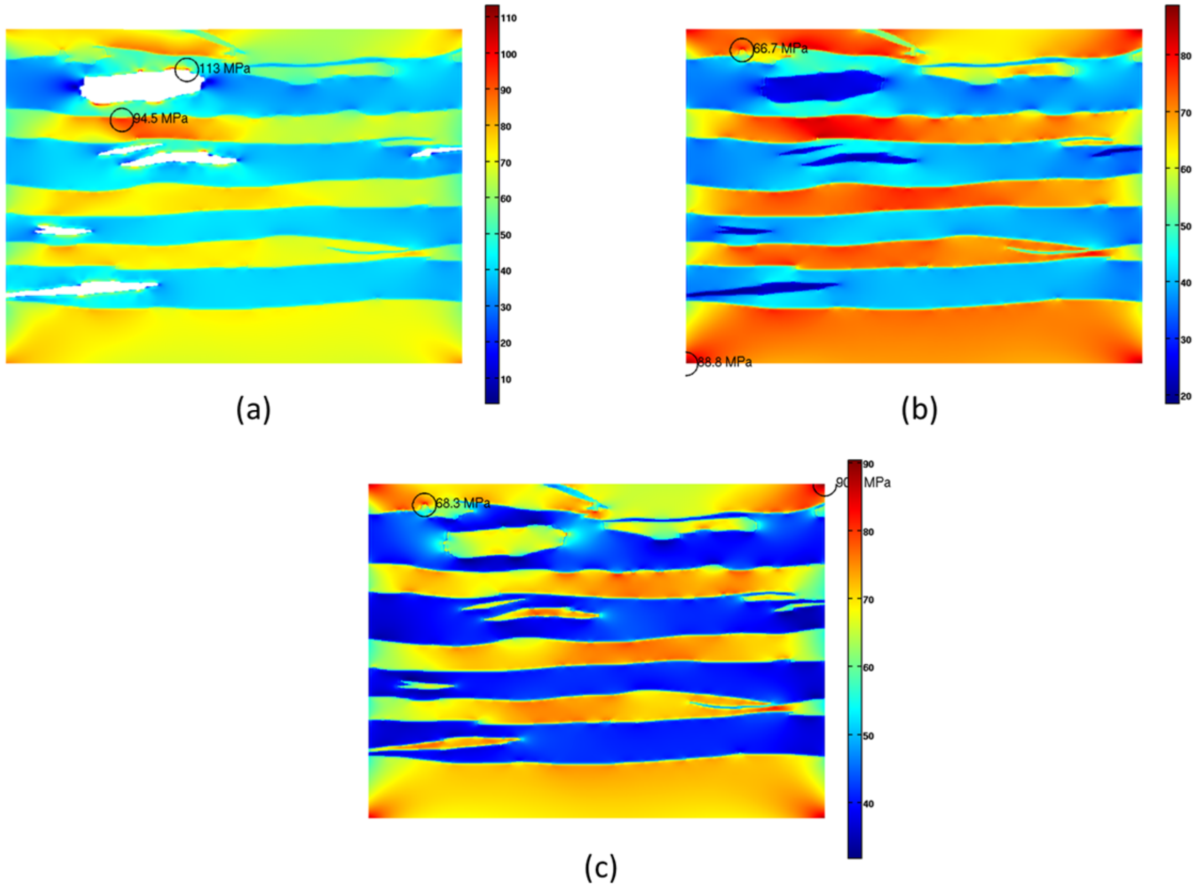

Figure 3.8. von Mises stress distribution. (a) When there are multiple void defects. (b) When there are multiple soft phase defects. (c) When there are multiple hard phase defects.

3.4.4. Samples with rectangle artificial defects of different vertical lengths

The simulation using SEM images with natural defects have one difficulty; the defect size and shape are not controllable. Thus it is difficult to have a quantitative assessment on influence of defect geometry on mechanical behavior. So the artificial defects of shape (c) in Figure 3.2 are included to study stress concentration in the wires. Figure 3.9(a) shows von

Mises stress distribution when a void defect introduced into the processed SEM image. The void defect in Figure 3.9(a) represents a pre-existing void in a Bi2212 filament. The defect has the lower edge in silver phase and upper end in Bi2212 phase, with the horizontal thickness of 2.8 μm and vertical length of 7.56 μm. To study the effect of defect length on stress concentration, the defect horizontal width (w) is fixed, but its vertical length (h) is increased from 0 to 15.2 μm by fixing the lower edge while raising the upper edge until the defect is long enough to cut through the whole filament.

Other than geometry, the influence of defect phase type could also be studied with artificial defects. So, in Figure 3.9(b) the same defect geometry as in Figure 3.9(a) is set up as the soft phase; while in Figure 3.9(c) it is set up as the hard phase. For meaningful comparison, it is important to note that in this study, results are only compared between defects of same type but different geometries, or of same geometry but different types. In other words only one variable is varied at a time when making comparison. Figure 3.9 shows the same trend as previous section when comparing defects of different types: stress is highest in sample with void, while no significant change of maximum stress is observed with "soft phase" and "hard phase" defects.

Figures 3.10(a, b, c) show the influence of defect length on maximum von Mises stress in the sample when the defect is a void, a soft phase, and a hard phase, respectively. Note that the result at zero length is obtained from the defect-free sample in Figure 3.6(a), while the longest defect at 15.12 μm is when the red area completely cuts through the Bi2212 filament. As shown in the graph in Figure 3.10(a), when the void expands its length across a Bi2212 filament vertically, the maximum stress in both silver and Bi2212 increases. This is somewhat similar to the classic case of elliptical hole in a single phase with its long axis aligned perpendicular to the applied force: the higher the ratio between the major and minor axis, the higher the stress concentration. Also, the fact that the longer void has higher stress concentration means that once a gap starts to develop, it will not stop until it cuts through the whole filament. But when the void completely cuts through the Bi2212 filament, there is a sudden reduction of stress concentration in Bi2212 phase while stress still continues to increase in silver phase. This means that the load has been transferred from the broken Bi2212 filament to the adjacent silver matrix but not to other Bi2212 filaments; and silver matrix therefore may have the potential to blunt the void from continuing to develop (if the strain is not increased any further). This agrees with experimental results that critical current in a wire degrades gradually, not suddenly with strain [10]. It's noteworthy to mention that these simulations are based on equilibrium stress distribution calculation, thus ignoring the yielding characteristics of Bi2212 and silver at high strain/stress. A more sophisticated model that includes yielding and/or plastic behavior could give more understanding. Also, similar to previous simulations, Figures 3.10(b, c) also show when the defect is a soft or hard solid phase, maximum stresses are very similar to defect-free case of Figure 3.6(a) with no significant change in maximum stress.

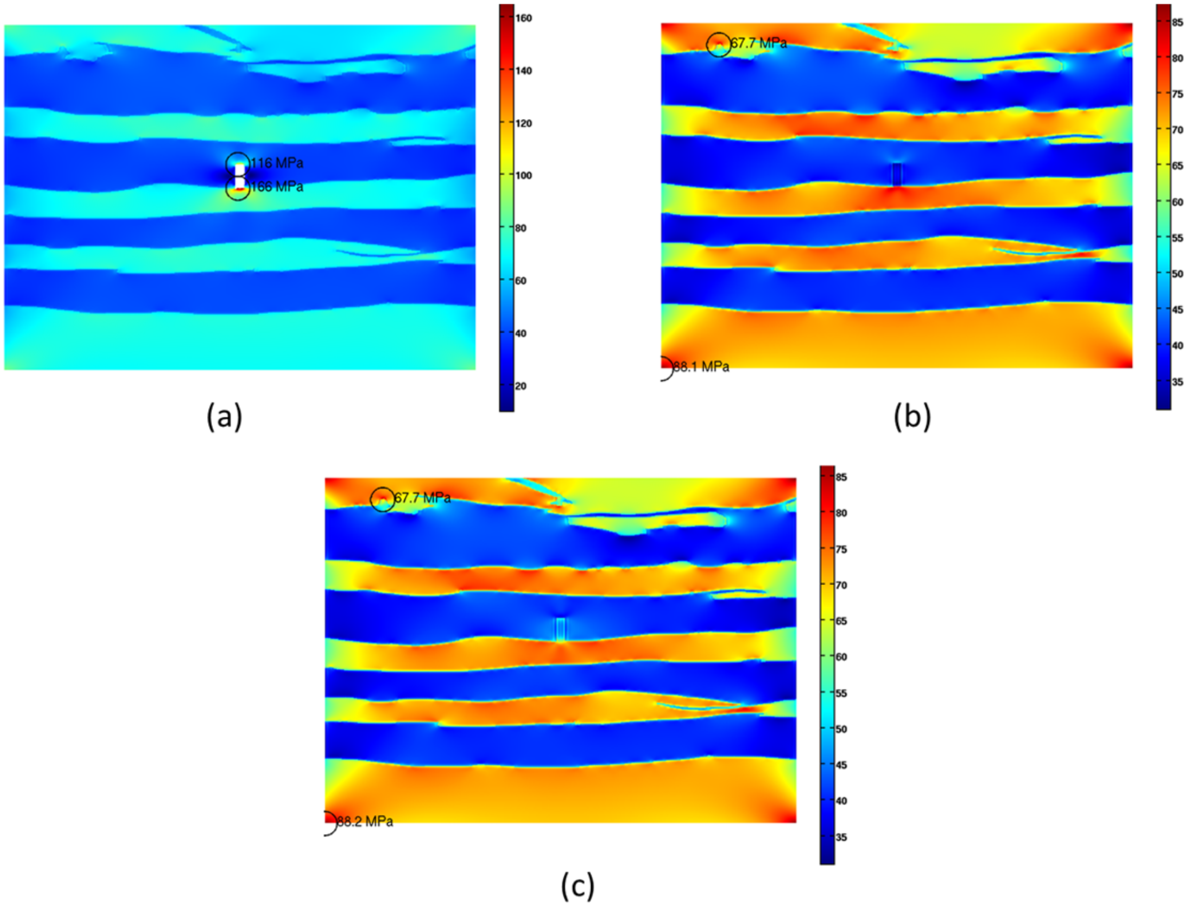

Figure 3.9. von Mises stress distribution when there is a rectangle defect. (a) When defect is a void. (b) When defect is a soft phase. (c) When defect is a hard phase.

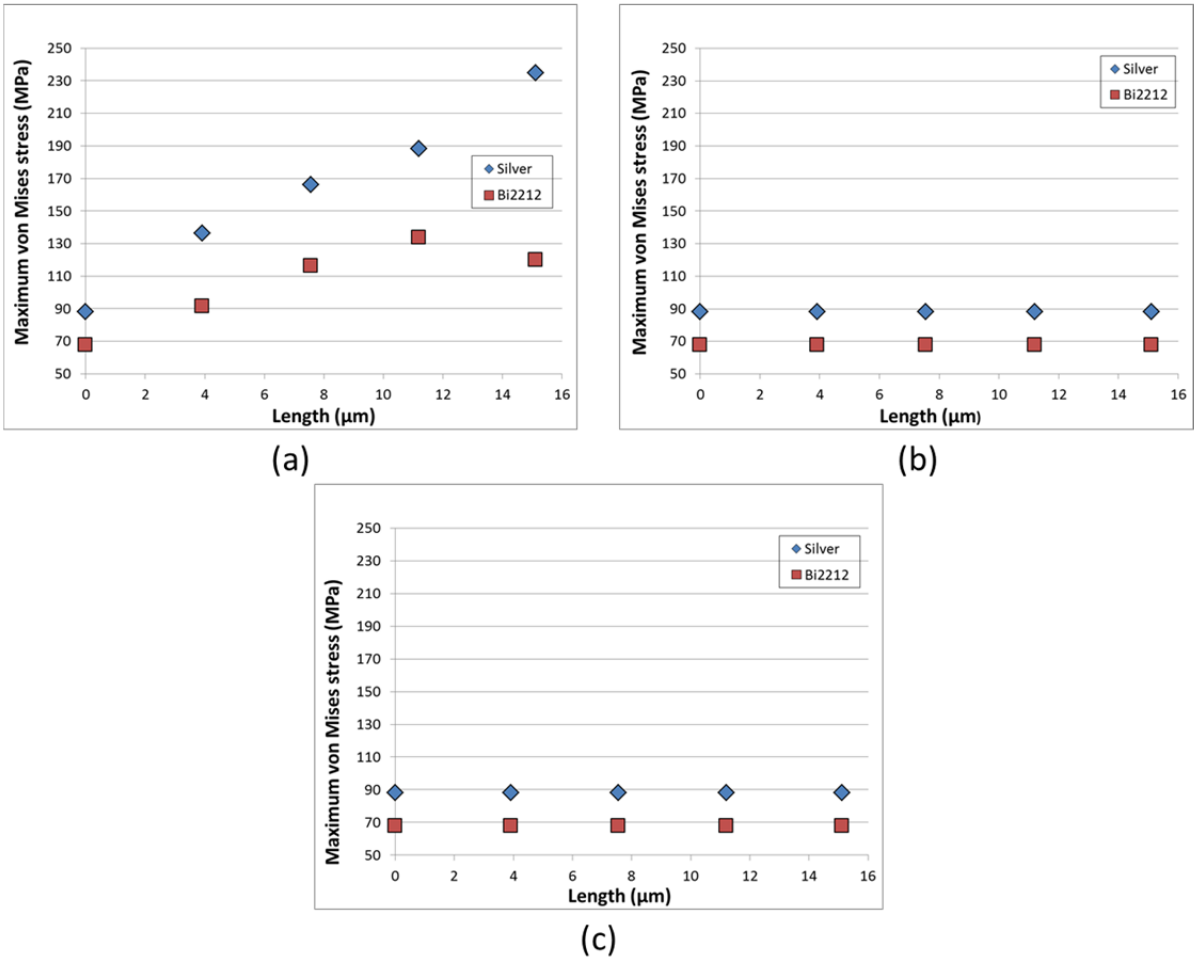

Figure 3.10. Dependence of maximum von Mises stress on rectangle defect's vertical length. (a) When defect is a void. (b) When defect is a soft phase. (c) When defect is a hard phase.

3.4.5. Samples with rectangle artificial defects of different horizontal widths

In the previous section, the rectangle defects' width w is fixed while the length h is varied. In contrast, in this section the width w is varied from 0 to 11.2 µm, while the defect length h is fixed at 15.2 µm. All the defects in this section have cut through the Bi2212 filament, as shown in Figure 3.11. Figure 3.11(a) shows the stress distribution when there is a void defect expanding through the whole filament. In Figure 3.11(b) the defect is the soft phase, and in Figure 3.11(c) it is the hard phase. The effect of the thickness on maximum von Mises stress is shown on Figures 3.12(a, b, c) when the defect is respectively a void, a soft phase, and a hard phase.

For vertical voids that have cut through the Bi2212 filament in Figure 3.11(a), there is a slight decrease of maximum stress in both Bi2212 and silver when the void's horizontal thickness increases as shown in Figure 3.12(a). This could be also explained by the decreasing vertical/horizontal size ratio mentioned above. This means a thinner void weakens the Bi2212 wire more than a thicker one. Meanwhile, Figures 3.12(b, c) also indicate that soft and hard solid defects will not have much influence on stress concentration of the system.

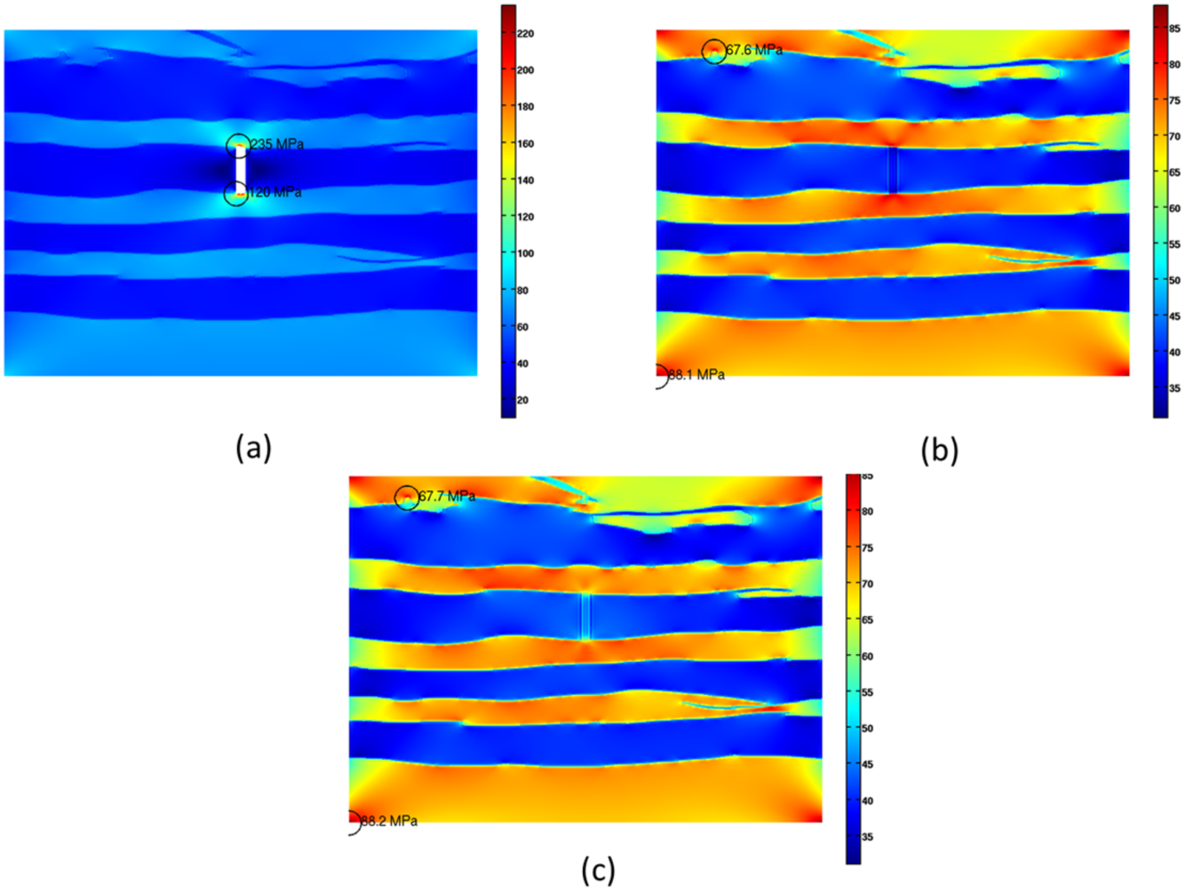

Figure 3.11. von Mises stress distribution when there is a vertical defect cutting through the whole filament. (a) When defect is a void. (b) When defect is a soft phase. (c) When defect is a hard phase.

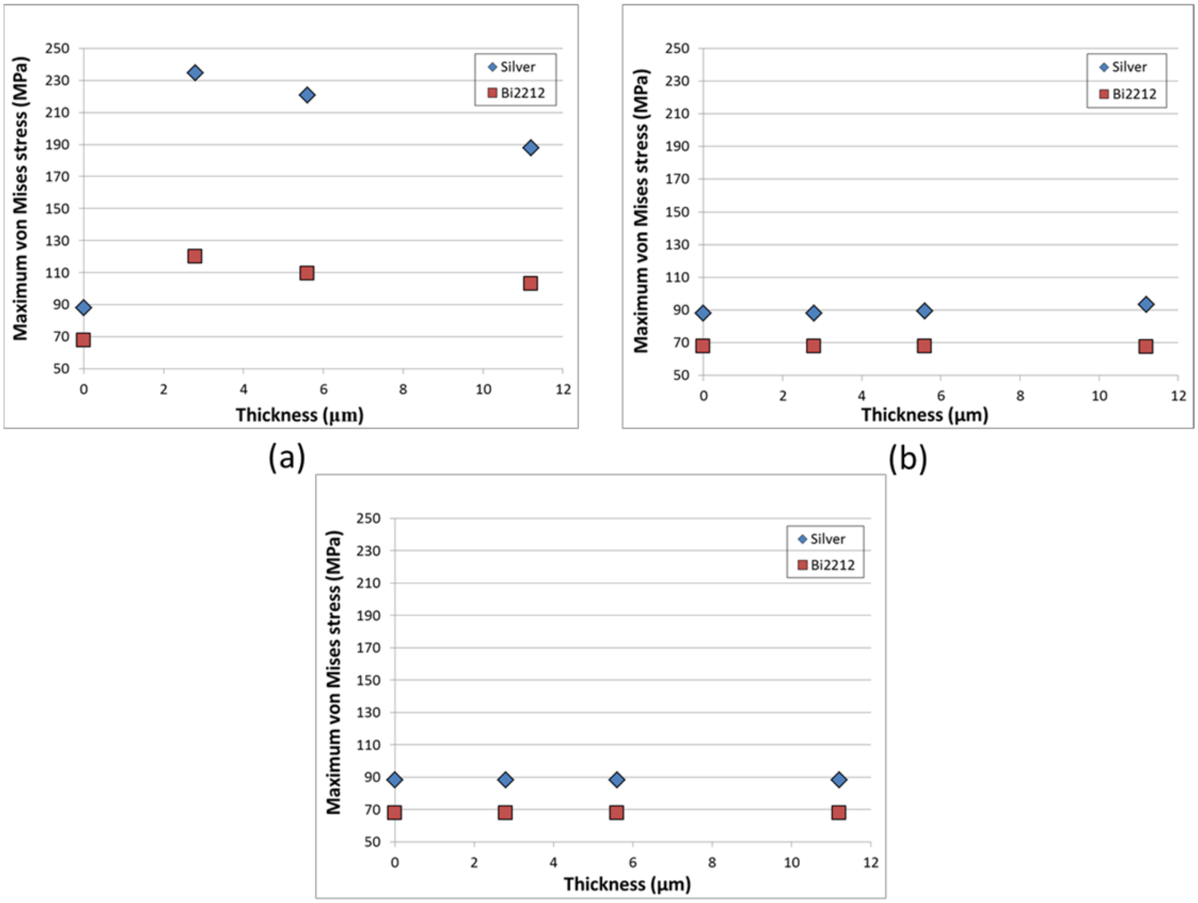

(a)

(b)

(c)

Figure 3.12. Dependence of maximum von Mises stress on vertical defect's horizontal width. (a) When defect is a void. (b) When defect is a soft phase. (c) When defect is a hard phase.

3.4.6. Samples with 45 degree slanted artificial defects of different widths

In this section, the defects are of shape (d) in Figure 3.2 are used for simulation. Figures 3.13(a) shows simulation result with a defect at 45 degree angle crossing the whole the Bi2212 filament when the defect is a void. The defect thickness (w) is varied from 0 to 11.2

μm to study the influence of void thickness to stress concentration. In Figure 3.13(b), the same defect geometry is set up as a soft phase; while in Figure 3.13(c) it is a hard phase. The influence of defect thickness on highest von Mises stress value is shown on Figure 3.14.

For defects of void type, Figures 3.13(a) shows very similar trend as the vertical defects in previous section, just with slightly lower stress concentration. Also, there is some slight increase of maximum stress in Bi2212 phase with the thickest void. This slight increase may not have something to do with the void thickness but with the specific boundary roughness of that void at the void/Bi2212 interface. And as expected, soft and hard solid defects in this case also do not change the maximum stress in the system.

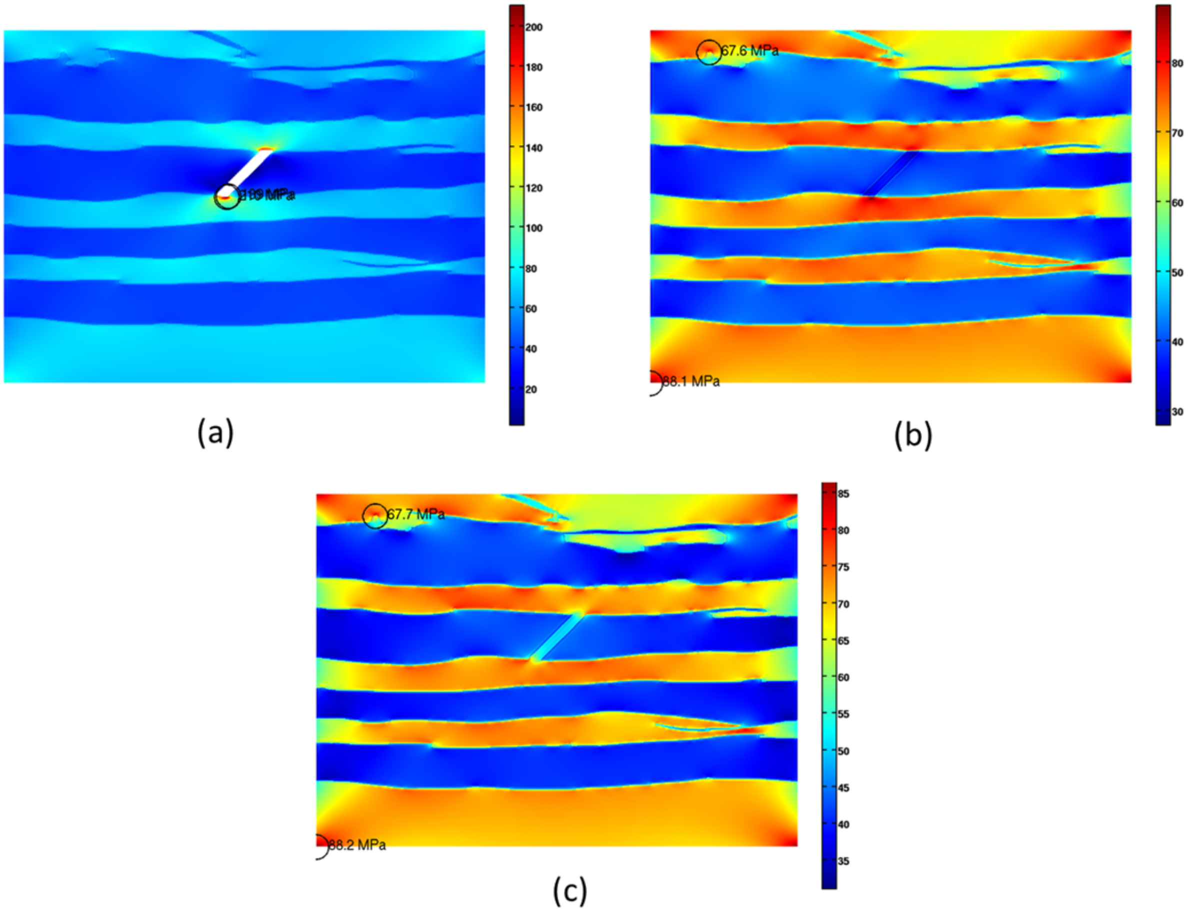

Figure 3.13. von Mises stress distribution when there is a 45 degree defect crossing the whole filament. (a) When defect is a void. (b) When defect is a soft phase. (c) When defect is a hard phase.

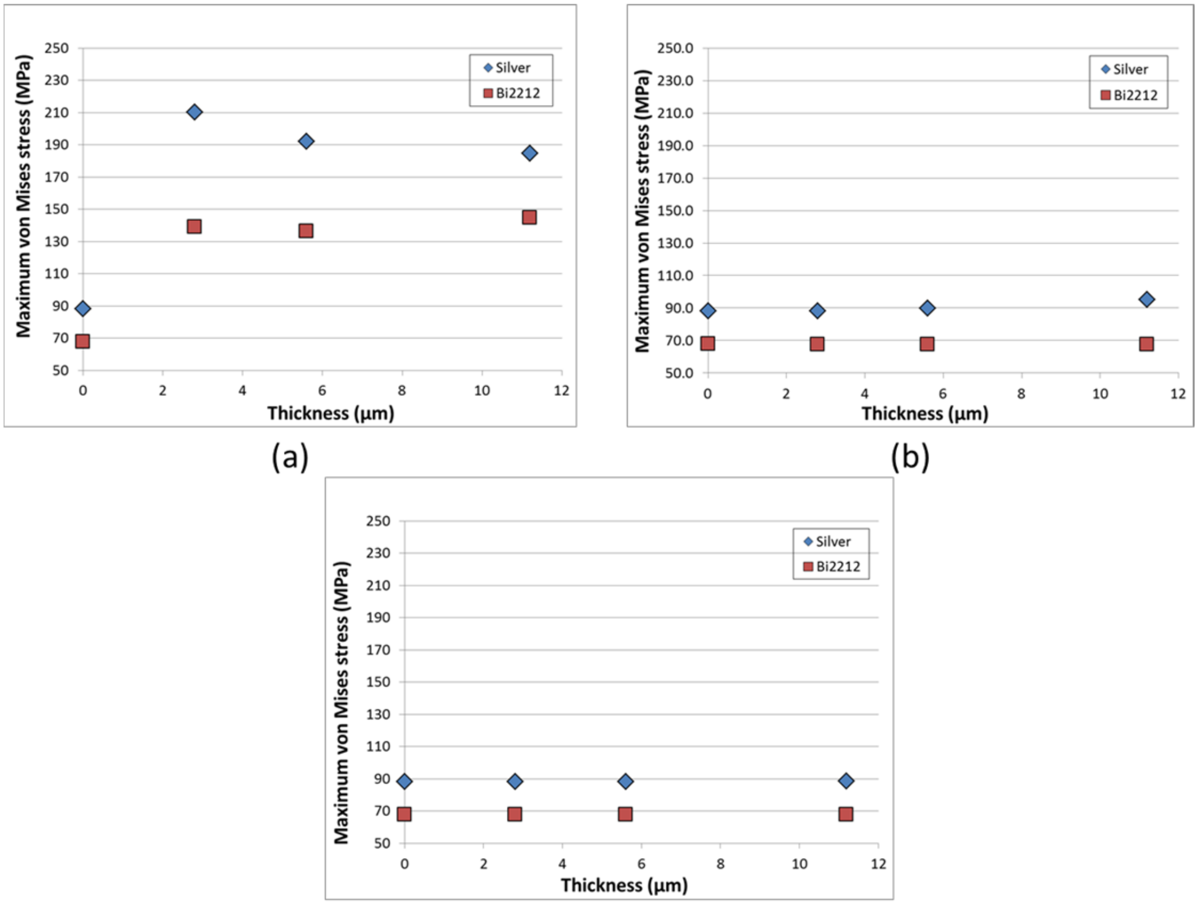

(a)

(b)

(c)

Figure 3.14. Dependence of maximum von Mises stress on 45 degree defect's width. (a) When defect is a void. (b) When defect is a soft phase. (c) When defect is a hard phase.

3.4.7. Samples with circular defects of different diameters

The defects of shape (e) in Figure 3.2 are used for simulations in this section. Similar to previous section, void, soft phase, and hard phase circular defects are illustrated in Figures 3.15(a, b, c), respectively. The defects' diameter (D) is varied from 0 to 22.4 µm; and the effect of diameter size on maximum von Mises stress is shown on Figures 3.16(a, b, c).

Similar to rectangle voids of increasing length, Figure 3.16(a) shows circular voids also show a trend of maximum stress increasing with void size; and when the void is large enough to completely cut through the Bi2212 filament stress in Bi2212 also drops while stress in silver keeps increasing. But compared to the rectangle void case, in this case there is one noticeable difference. When the void diameter is less than filament width (15.12 µm), the stress in Bi2212 phase rises significantly more than in silver phase when the void increases in size. In fact only in this case stress in Bi2212 becomes higher than in silver at some point. This could be due to the fact that unlike the rectangle voids that always have at least one end touching the silver phase, most circular voids are entirely encompassed in the Bi2212 phase.

Another difference is when the void diameter starts to become equal to the filament width (15.12 µm), the stress in Bi2212 does not drop like in other cases. This is because in this case, the low angle between the void's circular boundary and the filament's boundary creates sharp Bi2212 "tips" near the highest and lowest vertical positions of the void. These sharp tips make the stress in Bi2212 high despite the fact that the circular void has lower aspect ratio and smoother boundary line compared to other rectangle voids in previous sections. Only the when the void is large enough (22.4 µm diameter), then the Bi2212 tips become blunt and the stress in Bi2212 drops again. While the maximum stress in silver still continues to increase because the silver layers directly above and below the void get thinner as the void size increases.

Previously, experimental results have shown that smaller bubbles result in higher critical electric current. Now the simulations also show smaller bubbles could result in higher mechanical strength. Though this can be difficult to verify experimentally because in a real sample, there could be multiple bubbles and there is no direct control yet on the maximum size of the bubbles, which the highest stress concentration depends on. Meanwhile, the macroscopic critical current depends more on the average, not the maximum bubble size. And similar to other simulations, Figures 3.16(b, c) show soft and hard circular defects also do not affect Bi2212's maximum stress. The only difference is silver's maximum stress increases with diameter when the circular defect is of the soft phase as shown in Figure 3.16(b).

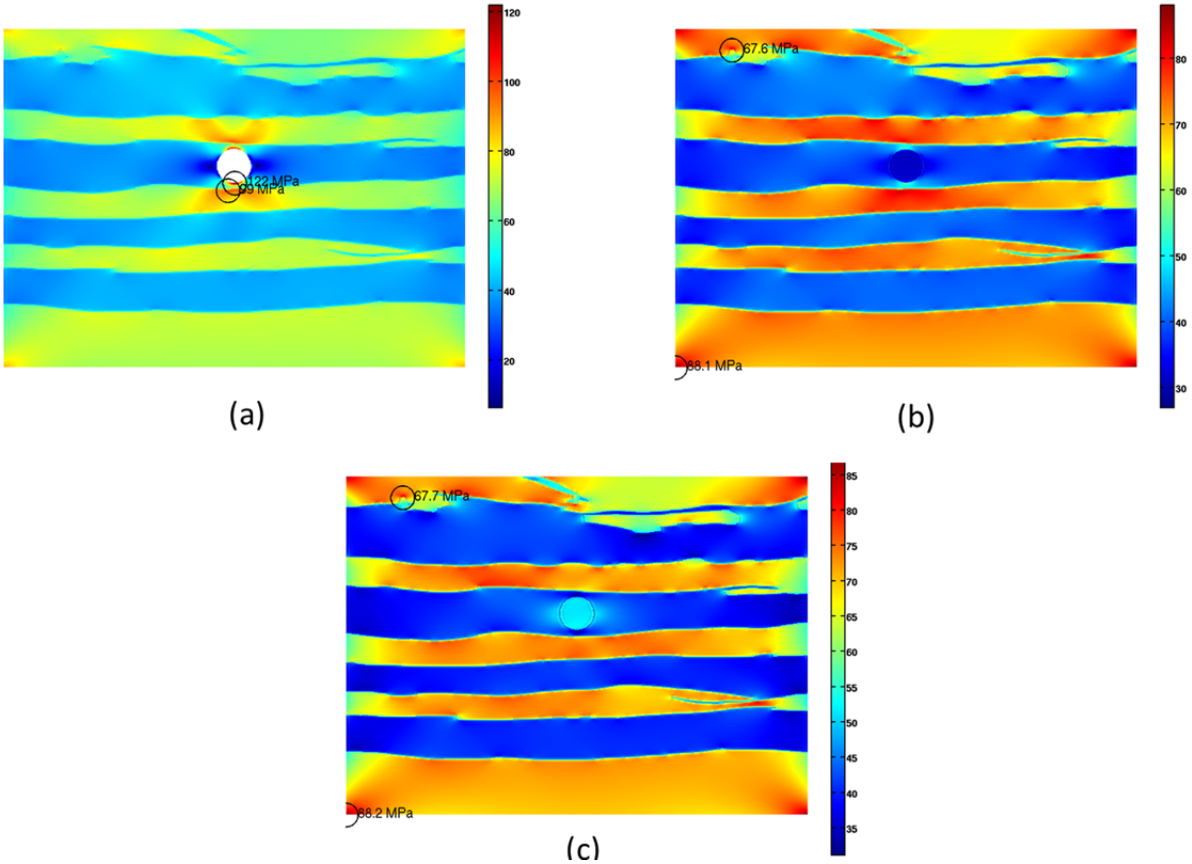

Figure 3.15. von Mises stress distribution when there is a round defect. (a) When defect is a void. (b) When defect is a soft phase. (c) When defect is a hard phase.

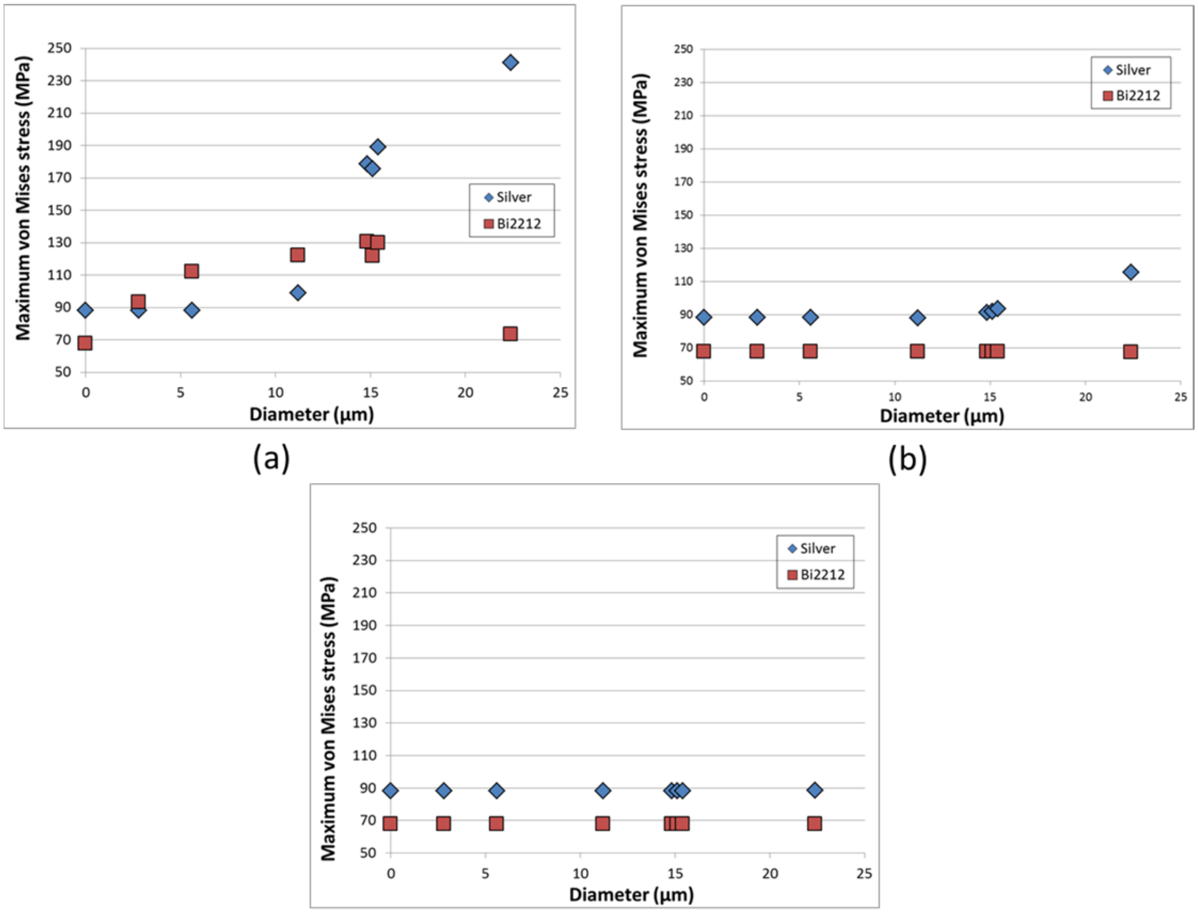

(a)

(b)

(c)

Figure 3.16. Dependence of maximum von Mises stress on round defect's diameter. (a) When defect is a void. (b) When defect is a soft phase. (c) When defect is a hard phase.

3.4.8. Samples with artificial rectangle voids inside a Bi2212 filament

The simulation results so far have shown void geometry has great influence on stress concentration in Bi2212 wires. But does the shape or the size of the void have more importance on the outcome? In previous simulation, there is a change of voids' both shape and size (or size alone in simulation with circular voids). So it is difficult to separate the influence of the two attributes. Thus in this study, three different rectangle voids of shape (c) in Figure 3.2 are used. Both the width w and the length h are varied, but the area A = w.h is kept the same for all three voids. Figure 3.17 shows the von Mises stress results of these voids. The h:w ratio is 4 in Figure 3.17(a), 1 in Figure 3.17(b), and 0.25 in Figure 3.17(c). The figures show there is a clear influence of defect aspect ratio on the stress concentration. Namely, Figure 3.17(a) with highest vertical to horizontal aspect ratio shows the highest stress concentration, 133 MPa in Bi2212 and 103 MPa in silver. While Figure 3.17(c) shows the lowest one, 78.8 MPa in Bi2212 and 88.1 MPa in silver. In fact, by comparing Figure 3.6(a) (the sample without any defect) and Figure 3.17(c), one finds that the stress in silver is essentially the same in both cases, with only some slight difference of stress in Bi2212. Thus it is apparent that defect's aspect ratio plays an important part on material's stress concentration. The voids' size still have influence on stress though, as shown previously in simulations with circular voids where there is no change in aspect ratio.

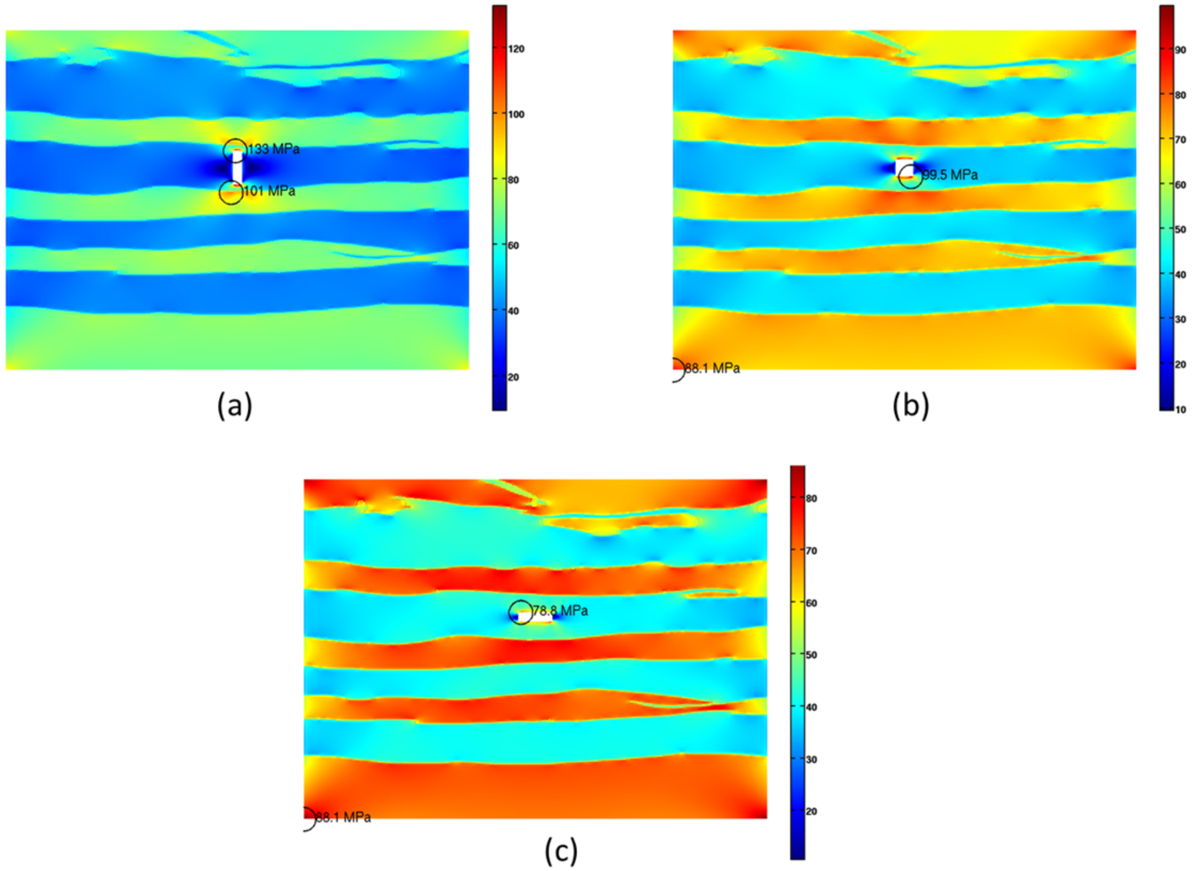

Figure 3.17. von Mises stress distribution when there is a rectangle void. (a) When defect's h:w aspect ratio is 4. (b) When the ratio is 1. (c) When the ratio is 0.25.

3.4.9. Sample with artificial voids around a Bi2212 filament

Figure 3.18 shows a different type of voids, in this figure the voids are not inside the Bi2212 filament but around it. The voids are artificially created to study the effect of detached Bi2212 filament on stress behavior. These voids are type (f) defect in Figure 3.2.

Figure 3.18 shows a different type of voids. In previous simulations, the voids are always inside the Bi2212 filaments. But it has been shown there are also voids between Bi2212 filaments and silver matrix [10]. These detached Bi2212 filaments are considered the "weak component" in electric conductivity of the wires because they are more prone to breakage when in compression. The result in Figure 3.18 is also from 0.1% strain test so it cannot be related to buckling behavior mentioned in [10]. But from the result, it can be concluded that these voids raise the stress concentration on the same range of magnitude as the internal voids do in Bi2212 phase.

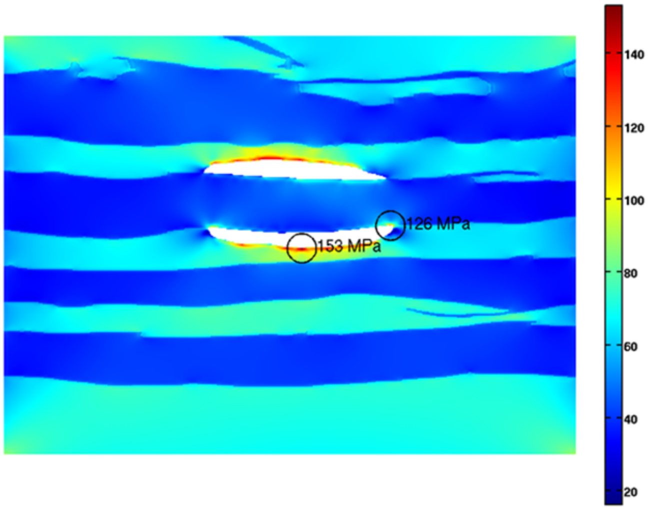

Figure 3.18. von Mises stress distribution when a fraction of a Bi2212 is detached from the silver matrix.

3.4.10. Simulation of stress concentration due to thermal cooling

In all previous simulation, it is assumed that there is no temperature change and initially, the Bi2212 wires are in stress-free state. But in experiments, the wires are often subjected to low temperature of cryogenic liquids such as helium and nitrogen, and experiments suggest that there is significant internal stress in the material, due to different thermal expansion coefficients of silver and Bi2212 phase. The peridynamic theory can easily incorporate thermal expansion into its model, simply by decomposing the total bond stretch s into two mechanical and thermal parts:

$$s = s_{mechanical} + s_{thermal} = s_{mechanical} + \alpha_{thermal}\Delta T \tag{3.2}$$

where $\alpha_{thermal}$ is the thermal expansion coefficient and ΔT is the temperature change. Then the same peridynamic formulas can be applied using $s_{mechanical}$ in place of the total stretch s. This is analogous to thermal strain in classical mechanics, and it has been applied in bond based models in other studies [24, 27, 29, 30, 46]. Figure 3.19 shows the von Mises stress distribution in the defect free sample when it is subjected to a temperature change of -300 K. This is the amount of change from room to liquid helium temperature. Thermal expansion coefficient of silver is set at 17x10^{-6} K^{-1}, Bi2212 at 12.7x10^{-6} K^{-1}. As expected, Figure 3.19(a) shows the Bi2212 phase in compression and silver in tension (negative pressure). The maximum von Mises stress in silver is 115 MPa, and in Bi2112 is 104 MPa. These are beyond the experimental yield stress in silver and fracture stress in Bi2212. Thus from the result, it can be predicted that silver goes into plastic deformation when cooling down to liquid helium temperature. A more advanced 2D peridynamic model including plasticity in it would be more adequate for modeling the mechanical behavior in the Bi2212 wires when they are under large temperature changes often seen in real experiments.

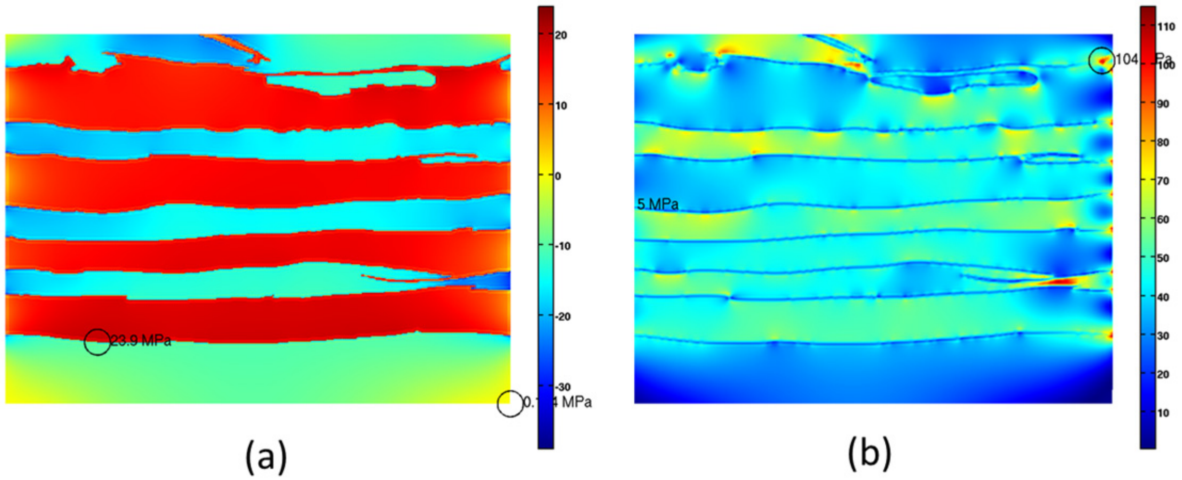

Figure 3.19. Stress distribution when temperature change is -300 K. (a) Pressure. (b) von Mises stress.

4. CONCLUSION AND SUGGESTED FUTURE WORK

2D state-based peridynamic model for plane stress simulation is used for investigating mechanical response in Bi2212 round wires. Compared to 3D model, the 2D model has the advantage of a smaller system and reduced computation time. Both m-convergence and δ-convergence of the model are investigated. For verification, both displacements and stresses are compared with results from a counterpart FEM model. The 2D peridynamics simulations show that both the displacements and stresses match well to the FEM results, except for the stresses on the sample boundaries where the free-boundary effect common to peridynamics modeling occurs. Energy minimization method with conjugate gradient algorithm is used for finding static stress distribution in the system, and different defect geometries and physical properties are investigated. The simulation is implemented with parallel Matlab code and ran on GPU to improve computation speed.

Simulation results show in Bi2212 phase, stress concentrates the most around void defects both inside and outside the Bi2212 filament. The voids' aspect ratio and their dimension in the direction perpendicular to the Bi2212 filaments have important influence on the stress concentration in the case of internal voids. Protruding growths and bridges of Bi2212 phase also concentrate stress to a lesser extent. Hard and soft secondary phases have the least influence in stress concentration in Bi2212. In silver, stress tends to concentrate on the Bi2212/silver interface. Thus where the cracks start to happen in a Bi2212 wire strongly depends on whether there are voids presenting in it or not. Reducing the maximum void size in Bi2212 is predicted to positively increase the mechanical strength of the Bi2212 wires.

Simulation shows on samples with a void defect inside a Bi2212 filament, maximum stress Bi2212 phase is increases with defect size in the direction perpendicular to the filament; until the defect completely cuts through it then the maximum stress in Bi2212 phase decreases, except for the round defects. This indicates that once a Bi2212 filament is broken, the load is transferred mostly to the silver matrix rather than other adjacent filaments. It is unknown how much influence the Bi2212 filament-to-filament distance has on the behavior of load transferring when a filament breaks. Additional simulations with various distances could be implemented to study this behavior and determine the minimum distance where the maximum stress in Bi2212 phase will not increase when a filament breaks. This distance is important to know to have the highest filament density (and electrical current) without negatively affecting the mechanical strength of the wire.

The peridynamics models have potential for investigating different microstructures and defects in Bi2212 wires or other similarly complex phase arrangements. Because of nature of digital images, the resolution or fineness of the simulation is currently limited by the quality of the input images when discretizing the images into peridynamic nodes. The elements/areas have to be fine enough to still retain the important microstructure features but coarse enough to smooth out the artifacts caused by the pixelation of the images. For example, in Figure 4.1(a), that requires the red and yellow regions must contain at least a few hundred pixels each. And the mesh size should be about a few times the pixel size at least. So this method can work well when the length scale of the jagged edges, or pixel size, is small compared to the other features in the digital image. If they had only a few pixels each then the method won’t work out well. So the quality of the input images is very important to achieve reasonable results.

For better preservation of the boundary symmetry, an uneven mesh that (roughly) follows the phase boundary could also be used, as illustrated in Figure 4.1(b). From the images, we can see that the jagged edges have been replaced by piece-wise smooth boundary lines with smaller angle change between adjacent edges (this angle is usually called “edge angle” in finite element literatures).It can be seen that the uneven mesh in Figure 4.1(b) preserves the defect geometry better than the even mesh in Figure 4.1(a). Then the uneven mesh can be further discretized to have finer results with higher resolutions. But the phase boundary line of this mesh should not be refined in the process because otherwise the phase boundaries would contain the artificial, jagged edges again. This scheme can overcome the minimum element size limitation in even mesh scheme; the only limitation is the phase boundary still cannot be refined.

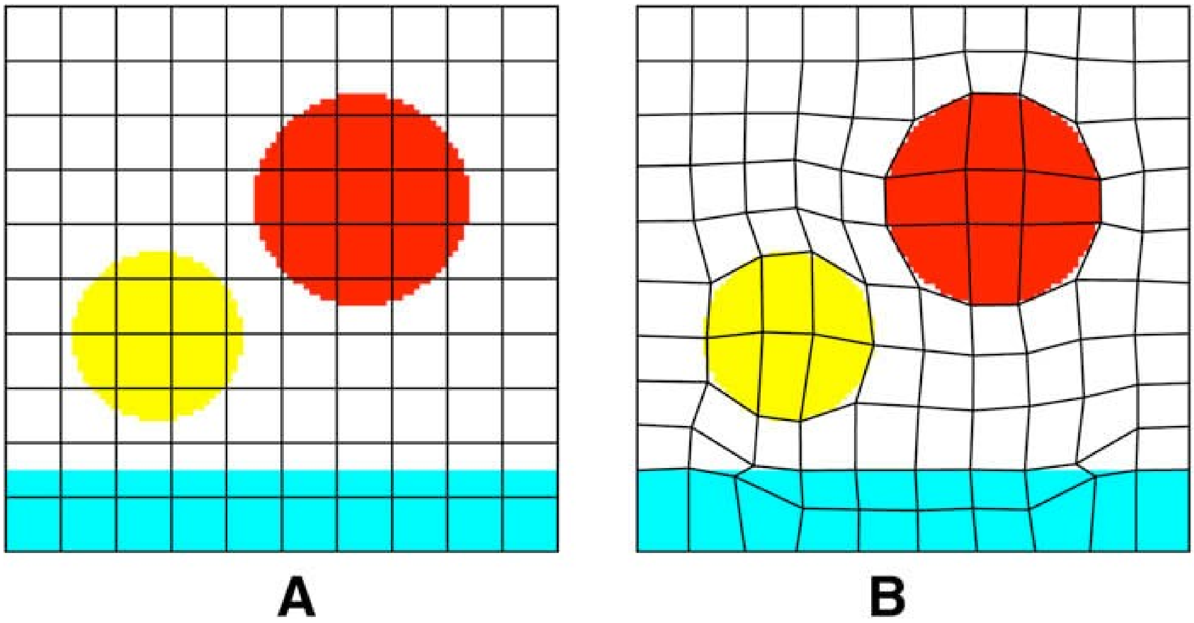

Figure 4.1. (a) A crude, uniform mesh. (b) A mesh that roughly follows the image's interface and smoothens out the pixel artifacts [61].

Another possible way to overcome this limitation of jagged edges is to first convert the pixel images to vector-based images first before implementing discretization. In a vector image, all the points, curves, or surfaces are described by mathematical expressions. Thus the jagged edges in the original, pixel image can be replaced by smooth mathematical curves. After that, the vector image can be discretized into a mesh of elements. With the vector image, the discretization grid size can be set to any size since there will be no pixels or jagged edges in the vector image. And different to the previous scheme, in this scheme the phase boundary lines can also refined indefinitely. It is because no matter how much one "zooms in", the boundary lines of a vector image can always be smooth, not jagged.

The 2D peridynamic models proposed in this study are elastic models and do not include plastic deformation, so applications are limited to the behavior of the wires in elastic region. Yielding in silver is of particular importance in mechanical behavior of the wires, as studies have shown silver yields significantly before failure from both the thermal cooling and mechanical loading the wires undergo while inside a magnet. The models are capable of modeling mechanical failure in Bi2212 phase because Bi2212 deformation is linearly elastic up until the failure strain, then it breaks suddenly. Silver however has a wide range of strain where it deforms plastically before failing. This plastic deformation has not been included in the models. Thus, more complete understanding of the composite wires via peridynamic simulation could be achieved if plasticity is added to the models.

REFERENCES

[1] J. Schwartz, F. Hunte, W. K. Chan, X. F. Gou, X. T. Liu, M. Phillips, Q. V. Le, G. Naderi, M. Turenne, and L. Ye, "Status of high temperature superconductor based magnets and the conductors they depend upon," Proceedings of the EuCARD - HE-LHC'10 AccNet Mini-Workshop on a "High Energy LHC", 2011.

[2] A. L. Mbaruku, Q. V. Le, H. Song, and J. Schwartz, "Weibull analysis of the electromechanical behavior of AgMg sheathed Bi 2 Sr 2 CaCu 2 O 8 + x round wires and YBa 2 Cu 3 O 7 − δ coated conductors," Superconductor Science and Technology, vol. 23, p. 115014, 2010.

[3] G. Naderi, X. Liu, W. Nachtrab, and J. Schwartz, "Understanding processing–microstructure–properties relationships in Bi 2 Sr 2 CaCu 2 O x /Ag round wires and enhanced transport through saw-tooth processing," Superconductor Science and Technology, vol. 26, p. 105010, 2013.

[4] X. T. Liu, Q. V. Le, and J. Schwartz, "Influencing factors on the electrical transport properties of split-melt processed Bi 2 Sr 2 CaCu 2 O x round wires," Superconductor Science and Technology, vol. 25, p. 075008, 2012.

[5] F. Kametani, T. Shen, J. Jiang, C. Scheuerlein, A. Malagoli, M. D. Michiel, Y. Huang, H. Miao, J. A. Parrell, E. E. Hellstrom, and D. C. Larbalestier, "Bubble formation within filaments of melt-processed Bi2212 wires and its strongly negative effect on the critical current density," Superconductor Science and Technology, vol. 24, p. 075009, 2011.

[6] S. Tengming, L. Xiaotao, U. P. Trociewitz, and J. Schwartz, "Electromechanical Behavior of Bi2Sr2CaCu2Ox Conductor Using a Split Melt Process for React-Wind-Sinter Magnet Fabrication," Applied Superconductivity, IEEE Transactions on, vol. 18, pp. 520-524, 2008.

[7] J. Jiang, W. L. Starch, M. Hannion, F. Kametani, U. P. Trociewitz, E. E. Hellstrom, and D. C. Larbalestier, "Doubled critical current density in Bi-2212 round wires by reduction of the residual bubble density," Superconductor Science and Technology, vol. 24, p. 082001, 2011.

[8] T. Shen, J. Jiang, F. Kametani, U. P. Trociewitz, D. C. Larbalestier, J. Schwartz, and E. E. Hellstrom, "Filament to filament bridging and its influence on developing high critical current density in multifilamentary Bi 2 Sr 2 CaCu 2 O x round wires," Superconductor Science and Technology, vol. 23, p. 025009, 2010.

[9] B. Ten Haken, A. Godeke, H. J. Schuver, and H. H. J. ten Kate, "Descriptive model for the critical current as a function of axial strain in Bi-2212/Ag wires," Magnetics, IEEE Transactions on, vol. 32, pp. 2720-2723, 1996.

[10] N. Cheggour, X. F. Lu, T. G. Holesinger, T. C. Stauffer, J. Jiang, and L. F. Goodrich, "Reversible effect of strain on transport critical current in Bi 2 Sr 2 CaCu 2 O8 + x superconducting wires: a modified descriptive strain model," Superconductor Science and Technology, vol. 25, p. 015001, 2012.

[11] L. F. Liu, D. H. Lin, and X. Q. Wang, "Computer Simulation of Flux Pinning in the High-Temperature Superconductors Bi-2212," Journal of Superconductivity and Novel Magnetism, vol. 24, pp. 1725-1727, 2011/07/01 2011.

[12] O. V. Velichko, B. Zeimetz, and T. A. Coombs, "Numerical Simulation of AC Current Limiting by Bulk Bi-2212 Ceramic and 2G YBCO Tapes," Applied Superconductivity, IEEE Transactions on, vol. 17, pp. 1780-1783, 2007.

[13] C. Zhi-Xiong, D. O. Welch, and G. S. Dubey, "Numerical simulations of elastic properties of flux-line lattices in high-T/sub c/ superconductors," Applied Superconductivity, IEEE Transactions on, vol. 9, pp. 2674-2677, 1999.

[14] J. Langston, M. Steurer, S. Woodruff, T. Baldwin, and J. Tang, "A generic real-time computer Simulation model for Superconducting fault current limiters and its application in system protection studies," Applied Superconductivity, IEEE Transactions on, vol. 15, pp. 2090-2093, 2005.

[15] X. Gou and J. Schwartz, "Fractal analysis of the role of the rough interface between Bi 2 Sr 2 CaCu 2 O x filaments and the Ag matrix in the mechanical behavior of composite round wires," Superconductor Science and Technology, vol. 26, p. 055016, 2013.

[16] S. A. Silling, "Reformulation of elasticity theory for discontinuities and long-range forces," Journal of the Mechanics and Physics of Solids, vol. 48, pp. 175-209, 2000.

[17] P. Seleson, M. L. Parks, M. Gunzburger, and R. B. Lehoucq, "Peridynamics as an Upscaling of Molecular Dynamics," Multiscale Modeling & Simulation, vol. 8, pp. 204-227, 2009.

[18] M. L. Parks, R. B. Lehoucq, S. J. Plimpton, and S. A. Silling, "Implementing peridynamics within a molecular dynamics code," Computer Physics Communications, vol. 179, pp. 777-783, 2008.

[19] Parks, Seleson, Plimpton, Lehoucq, and Silling, "Peridynamics with LAMMPS: A User Guide v0.2 Beta," Sandia Report 2010.

[20] S. A. Silling and R. B. Lehoucq, "Convergence of Peridynamics to Classical Elasticity Theory," Journal of Elasticity, vol. 93, pp. 13-37, 2008/10/01 2008.

[21] S. A. Silling and E. Askari, "A meshfree method based on the peridynamic model of solid mechanics," Computers & Structures, vol. 83, pp. 1526-1535, 2005.

[22] R. W. Macek and S. A. Silling, "Peridynamics via finite element analysis," Finite Elements in Analysis and Design, vol. 43, pp. 1169-1178, Nov 2007.

[23] P. Seleson and M. Parks, "On the Role of the Influence Function in the Peridynamic Theory," vol. 9, pp. 689-706, 2011-11-11 2011.

[24] B. Kilic and E. Madenci, "Peridynamic Theory for Thermomechanical Analysis," IEEE Transactions on Advanced Packaging, vol. 33, pp. 97-105, Feb 2010.

[25] F. Bobaru and Y. D. Ha, "Adaptive refinement and multiscale modeling in 2D peridynamics," vol. 9, pp. 635-660, 2011-11-11 2011.

[26] Y. Ha and F. Bobaru, "Studies of dynamic crack propagation and crack branching with peridynamics," International Journal of Fracture, vol. 162, pp. 229-244, 2010/03/01 2010.

[27] B. Kilic and E. Madenci, "An adaptive dynamic relaxation method for quasi-static simulations using the peridynamic theory," Theoretical and Applied Fracture Mechanics, vol. 53, pp. 194-204, 2010.

[28] B. Kilic, A. Agwai, and E. Madenci, "Peridynamic theory for progressive damage prediction in center-cracked composite laminates," Composite Structures, vol. 90, pp. 141-151, Sep 2009.

[29] B. Kilic and T. U. o. A. M. Engineering, Peridynamic Theory for Progressive Failure Prediction in Homogeneous and Heterogeneous Materials: The University of Arizona, 2008.

[30] B. Kilic and E. Madenci, "Structural stability and failure analysis using peridynamic theory," International Journal of Non-Linear Mechanics, vol. 44, pp. 845-854, Oct 2009.

[31] E. Emmrich and O. Weckner, "On the well-posedness of the linear peridynamic model and its convergence towards the Navier equation of linear elasticity," pp. 851-864, 2007/12 2007.

[32] S. A. Silling, W. H. Gerstle, and N. Sau, Peridynamic modeling of plain and reinforced concrete structures, 2005.

[33] F. Bobaru, M. Yang, L. F. Alves, S. A. Silling, E. Askari, and J. Xu, "Convergence, adaptive refinement, and scaling in 1D peridynamics," International Journal for Numerical Methods in Engineering, vol. 77, pp. 852-877, 2009.

[34] S. A. Silling, M. Epton, O. Weckner, J. Xu, and E. Askari, "Peridynamic states and constitutive modeling," Journal of Elasticity, vol. 88, pp. 151-184, Aug 2007.

[35] S. A. Silling, "Linearized Theory of Peridynamic States," Journal of Elasticity, vol. 99, pp. 85-111, 2010/03/01 2010.

[36] J. T. Foster, S. A. Silling, and W. W. Chen, "Viscoplasticity using peridynamics," International Journal for Numerical Methods in Engineering, vol. 81, pp. 1242-1258, Mar 5 2010.

[37] J. A. Mitchell, "A Nonlocal, Ordinary, State-Based Plasticity Model for Peridynamics," Sandia National Laboratories, vol. SAND2011-3166, 2011.

[38] F. Bobaru and W. Hu, "The Meaning, Selection, and Use of the Peridynamic Horizon and its Relation to Crack Branching in Brittle Materials," International Journal of Fracture, vol. 176, pp. 215-222, 2012/08/01 2012.

[39] D. Rubin, E. Krempl, and W. M. Lai, Introduction to Continuum Mechanics: Elsevier Science, 1994.

[40] S. A. Silling and R. B. Lehoucq, "Peridynamic Theory of Solid Mechanics," Advances in Applied Mechanics, Vol 44, vol. 44, pp. 73-168, 2010.

[41] R. B. Lehoucq and S. A. Silling, "Force flux and the peridynamic stress tensor," Journal of the Mechanics and Physics of Solids, vol. 56, pp. 1566-1577, 2008.

[42] Y. D. Ha and F. Bobaru, "Characteristics of dynamic brittle fracture captured with peridynamics," Engineering Fracture Mechanics, vol. 78, pp. 1156-1168, 2011.

[43] A. Agwai, I. Guven, and E. Madenci, "Peridynamic theory for impact damage prediction and propagation in electronic packages due to drop," in Electronic Components and Technology Conference, 2008. ECTC 2008. 58th, 2008, pp. 1048-1053.

[44] A. Agwai, I. Guven, and E. Madenci, "Peridynamic theory for failure prediction in multilayer thin-film structures of electronic packages," in Electronic Components and Technology Conference, 2008. ECTC 2008. 58th, 2008, pp. 1614-1619.

[45] F. P. Bowden, J. H. Brunton, J. E. Field, and A. D. Heyes, "Controlled Fracture of Brittle Solids and Interruption of Electrical Current," Nature, vol. 216, pp. 38-42, 1967.

[46] B. Kilic and E. Madenci, "Prediction of crack paths in a quenched glass plate by using peridynamic theory," International Journal of Fracture, vol. 156, pp. 165-177, 2009/04/01 2009.

[47] F. Bobaru and M. Duangpanya, "The peridynamic formulation for transient heat conduction," International Journal of Heat and Mass Transfer, vol. 53, pp. 4047-4059, Sep 2010.

[48] S. A. Silling and F. Bobaru, "Peridynamic modeling of membranes and fibers," International Journal of Non-Linear Mechanics, vol. 40, pp. 395-409, 2005.

[49] X. Jifeng, A. Abe, W. Olaf, R. Hamid, and S. Stewart, "Damage and Failure Analysis of Composite Laminates under Biaxial Loads," in 48th AIAA/ASME/ASCE/AHS/ASC Structures, Structural Dynamics, and Materials Conference, ed: American Institute of Aeronautics and Astronautics, 2007.

[50] J. Xu, A. Askari, O. Weckner, and S. Silling, "Peridynamic Analysis of Impact Damage in Composite Laminates," Journal of Aerospace Engineering, vol. 21, pp. 187-194, 2008.

[51] P. Lall, S. Shantaram, and D. Panchagade, "Peridynamic-models using finite elements for shock and vibration reliability of leadfree electronics," in Thermal and Thermomechanical Phenomena in Electronic Systems (ITherm), 2010 12th IEEE Intersociety Conference on, 2010, pp. 1-12.

[52] X. Chen and M. Gunzburger, "Continuous and discontinuous finite element methods for a peridynamics model of mechanics," Computer Methods in Applied Mechanics and Engineering, vol. 200, pp. 1237-1250, 2011.

[53] N. S. Ottosen and M. Ristinmaa, The Mechanics of Constitutive Modeling: Elsevier Science, 2005.

[54] J. R. Shewchuk, "An Introduction to the Conjugate Gradient Method Without the Agonizing Pain," School of Computer Science, Carnegie Mellon University, Pittsburgh, PA 15213, 1994.

[55] E. Oterkus, "Peridynamic Theory for Modeling Three-Dimensional Damage Growth in Metallic and Composite Structures," ed: The University of Arizona.

[56] Q. V. Le, W. K. Chan, and J. Schwartz, "(in review) A two-dimensional ordinary, state-based peridynamic model for linearly elastic solids," International Journal for Numerical Methods in Engineering, 2013.

[57] J. K. Shin, S. Ochiai, M. Sugano, H. Okuda, Y. Mukai, M. Sato, S. S. Oh, D. W. Ha, and S. C. Kim, "Analysis of the residual strain change of Bi2212, Ag alloy and Ag during the heating and cooling process in Bi2212/Ag/Ag alloy composite wire," Superconductor Science and Technology, vol. 21, p. 075018, 2008.

[58] J. K. Shin, S. Ochiai, H. Okuda, Y. Mukai, H. Matsubayashi, S. S. Oh, D. W. Ha, S. C. Kim, and M. Sato, "Estimation of Young's modulus, residual strain and intrinsic fracture strain of Bi2212 filaments in Bi2212/Ag/Ag alloy composite wire," Physica C: Superconductivity, vol. 468, pp. 1792-1795, 2008.

[59] D. C. van der Laan, H. J. N. van Eck, M. W. Davidson, B. ten Haken, H. H. J. ten Kate, and J. Schwartz, "Magneto-optical imaging study of the crack formation in superconducting tapes caused by applied strain," Physica C: Superconductivity, vol. 372–376, Part 2, pp. 1020-1023, 2002.

[60] D. C. van der Laan, H. J. N. van Eck, B. Haken, H. H. J. Kate, and J. Schwartz, "Strain effects in high temperature superconductors investigated with magneto-optical imaging," Applied Superconductivity, IEEE Transactions on, vol. 13, pp. 3534-3539, 2003.

[61] A. C. E. Reid, S. A. Langer, R. C. Lua, V. R. Coffman, S.-I. Haan, and R. E. García, "Image-based finite element mesh construction for material microstructures," Computational Materials Science, vol. 43, pp. 989-999, 2008.